MULTI-MODELLING of ABRASIVE WATERJET MACHINING

By

PATRICK HALE, B.ENG & MGMT

A Thesis submitted to the School of Graduate Studies

in partial fulfillment of the requirements for the

Degree of Master of Applied Science

MULTI-MODELLING of ABRASIVE WATERJET MACHINING

MASTER OF APPLIED SCIENCE MCMASTER UNIVERSITY

MECHANICAL ENGINEERING HAMILTON, ONTARIO

TITLE: MULTI-MODELLING OF ABRASIVE WATERJET MACHINING

AUTHOR: PATRICK HALE

SUPERVISOR: DR. EU-GENE NG

NUMBER OF PAGES: CXXI, 121

Abstract

Abrasive waterjet (AWJ) machining is a complex, non-conventional machining process involving numerous input parameters including hydraulic, abrasive, mixing and cutting that must be accurately manipulated to guarantee precise cutting and quality. Currently, available models are empirical or require continuous calibration, or extensive experimental work. To reduce the calibration and experimental time required for accurate prediction of AWJ cutting, computational fluid dynamics (CFD) is being utilized to model the nozzle flow interaction; high pressure water is pushed through the orifice into the mixing chamber, pulling the abrasive into the flow and cohering in the focus tube. Initial research worked towards understanding the effect that input parameters - such as pressure, particle size and shape, focus tube length and volume fraction of air in fluid mixture - have on the velocity profile through the nozzle and upon exit to the atmosphere. Once understood, the CFD model can be utilized to vary mass-inlet, mixing head, orifice and focus tube dimensions to optimize velocity profile of abrasive material including magnitude and jet coherency. Primarily focused on pump pressure, which is limited by technology - an optimized AWJ nozzle will increase material removal rate and/or enhance cut quality without making changes to any other AWJM components.

Utilizing the velocity output information from the CFD model, a depth of penetration erosion prediction model was generated. Based on methodology from Finnie, and modified by Hashish and ElTobgy, a multi-particle erosion model of an impacted work piece is developed. With an updated formulation for the specific cutting resistance of a work piece, dependent on particle velocity and nozzle traverse speed, the erosion prediction over the

sixty-five different setups modelled and tested experimentally, reduced error on average 41.8%. Moreover, the development of this model created multi-layered surface plots, illustrating for quick reference, the erosion of a work piece for a given set of parameters albeit mass flow rate, pump pressure and traverse rate.

Further, a database of quick reference guides, including variable input settings, nozzle types, garnet types and work piece materials can easily be developed. Finally, a new methodology for the leading edge of the waterjet is described and can be incorporated into the erosion simulation by making use of the ``top-hat`` profile generated in the CFD model. This would reduce reliance on model constants to account for secondary cutting, or when particles do not contribute to cutting but are simply entrained in the fluid flow.

Both models demonstrated good correlation with experiments or literature. The use of these models will increase understanding of the complex abrasive waterjet process and reduce the need for costly experiments moving forward.

Acknowledgments

I would like to thank my supervisor, Professor Dr. Eu-Gene Ng, for all his guidance and consideration throughout my study; I am indebted to him for the opportunity to continue my education. I would also like to thank Terry Wagg for his assistance operating the waterjet and other equipment throughout my research. I would like to thank my family for their continued support throughout my study. Lastly, I would like to thank NSERC CANRIMT and Discovery grant for providing financial support for this research.

Nomenclature

m_a	Mass abrasive	(kg)
σ_f	Material flow stress	(N/mm^2)
$\ddot{y}, \ddot{x}, \ddot{\varphi}$	Particle acceleration components	(m/s^2, rad/s^2)
$\dot{x}, \dot{y}, \dot{\varphi}$	Particle velocity components	(m/s, rad/s)
K	Vertical to horizontal cutting force ratio	
γ	Depth of contact to depth of cut ratio	
b	Particle width	(mm)
$\propto$	Abrasive impact angle	(rad)
σ_y	Elastic load limit	(N/mm^2)
W_d	Deformation wear	(kg)
W_c	Cutting wear	(kg)
ε_b	Deformation wear factor	

v_{el}	Threshold velocity	(m/s)
φ_c	Material dependent wear factor	
v_p, v_t	Poisson's ratio for particle and target material	
ρ_p	Particle density	(kg/m^3)
E_p, E_t	Young's moduli for particle and target material	(MPa)
d_j	Jet diameter	(mm)
$\dot{m}_a$	Abrasive mass flow rate	(kg/s)
h_c	Depth of cut due to cutting wear	(mm)
h_d	Depth of cut due to deformation wear	(mm)
u	Feed rate	(mm/s)
V_c	Critical velocity	(m/s)
R_f	Roundness factor	(≤1.0)
C_f	Wall friction	

C_k, ε, C_1	Constants	
$N_1, N_2, N_3, N_4, N_5, N_6$	Non-dimensional constants for Hashish's model	
F_v, F_{vn}	Cutting forces in velocity and normal direction	(N)
K_s	Specific cutting energy	(N/mm^2)
θ	Particle direction	(rad)
φ	Particle rotation about center of gravity	(rad)
k, l	Particle tip location	(mm)
t	Depth of cut (d.o.c.)	(mm)
$delK, delL$	Change in particle tip position	(mm)
P	Pump pressure	(MPa)
s	Stand-off distance (s.o.d.)	(mm)
h	Depth of penetration (d.o.p.)	(mm)
dts	Time step during particle erosion formulation	(s)

Contents

List of Figures

List of Tables

1 Introduction

1.1 What is Waterjet Machining?

Waterjet machining is a versatile, recently developed cutting process. Numerous shapes, sizes and materials can be machined in an efficiently nested configuration, saving material and time. By changing various input parameters, versus retooling, multiple jobs can be taken on in record time. Initially, Dr. Norman Franz achieved quick bursts of high pressure, powerful enough to cut wood, by dropping heavy weights onto columns of water in the 1950s. Process developments lead to commercialized intensifier pumps being created for the cutting of disposable diapers in 1975 using only water. The addition of garnet, which is an abrasive material, was added to the waterjet process by Dr. Mohamed Hashish in 1979 and is responsible for the erosion when cutting any hard materials (Corporation, Our History-A History of Leadership, 2012).

In Figure 1, a comparison of abrasive waterjet machining (AWJM) to other non-conventional machining processes including laser, plasma and EDM is provided. Most advantageous, AWJM has the ability to machine any material, with little variance in setup for different materials, with precision of up to 0.001”, for little cost in comparison.

	Waterjet	Plasma	Laser	EDM
Process	Erosion process: high speed liquid sandpaper	Burning / melting process using high temperature ionized gas arc	Melting process using concentrated laser light beam	Erosion process using electrical discharge
Materials	Any material.	Primarily steel, stainless steel and aluminum.	Primarily steel, stainless and aluminum. Can also cut a variety of other materials.	Conductive materials only.
Thickness	Up to 24 inches, virtually any material. Z constraint is only limit to thickness.	Up to 2-3 inches, depending on material.	Generally 1 inch or less, depending on materials.	Generally 12 inch or less.
Part Accuracy	Up to .001"	Up to .010"	Up to .001"	Up to .0001"
Capital Investment	$60k to over $300k	$60k to over $300k	$200K to over $1M	$100k to over $400k
Machine Setup	Same setup for all materials	Different setup for different jobs	Different gases and parameters for different jobs	Different wire types for different jobs

Figure 1: Non-conventional machining process comparison (Corporation, Comparative Cutting, 2012)

1.2 Advantages of Abrasive Waterjet Machining

Abrasive waterjet (AWJ) technology is an advanced, non-conventional machining tool used in a variety of industrial applications because of its ability to machine typically difficult materials effectively; materials including ceramics, marbles and composites that have a tendency to fracture, damage, or change composition during more traditional machining techniques. AWJ also reduces the mechanical loading effects on the work piece. As such, parts can be nested extremely close, utilizing material. Moreover, parts can even share the same cut line as AWJ does not create the heat-affected zone common with conventional machining. In addition, there is no thick crust left behind as seen when using plasma flame or laser cutters. The equipment required for AWJM is much lighter than equivalent laser cuttings, reducing the problems associated with deceleration of robots and back lash issues. AWJM generally requires the following components: a high pressure pump/intensifier, an abrasive delivery system (hopper), a catcher (large water basin), a positioning system, and a mixing unit. All components are essential for machining to take place, however the mixing unit facilitates the transfer of momentum from the water to the abrasives, responsible for the cutting, and is therefore fundamental to the AWJM process.

The typical AWJ system uses an entrainment process whereby the water is pumped at an extremely high pressure (100-400MPa) utilizing intensifier technology. The intensifier principle is the theory that pressure over a large area is increased drastically by the multiple of area decrease. Flow International Inc. (Flow) pressurizes oil to 3000psi against a biscuit shown in Figure 2.

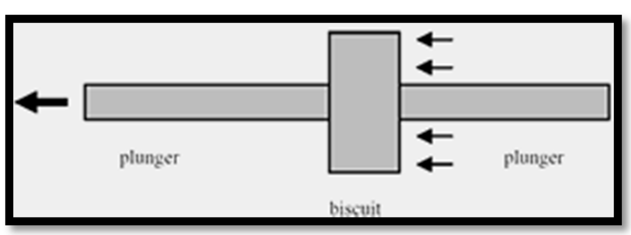

Figure 2: Pump interior description (Corporation, Intensifier Pump Detail, 2012)

The plunger, with area 20 times less than the biscuit, pressurizes water up to 94000psi (Corporation, Intensifier Pump Detail, 2012). The high pressure water then travels into the nozzle through an extremely fine orifice where the immensely pressured, slow moving fluid, is converted to kinetic energy, high speed fluid, moving inside the mixing chamber.

The turbulent high velocity water then pulls the abrasive material into the mixing chamber via the Venturi phenomenon, from a separate inlet aside the mixing chamber, where the water accelerates the abrasive (A. Tazbit, 1996). The Venturi effect is an influence on the jet flow as the cross-sectional area of the pipe changes. If the area is small, increases, then converges - as is the case in the mixing head - the velocity initially high, decreases in the mixing head and then increases down the nozzle tube. Conversely, the pressure initially high, increases in the mixing head, then decreases down the nozzle tube. These relationships are due to Bernoulli`s principle and the continuity equation. As such, the large pressure difference between the stagnate garnet and the high velocity water-air jet stream creates a vacuum effect that pulls the garnet into the mixture, entraining it into the flow in the mixing head and cohering the flow down the nozzle focus tube (Robert W. Fox, 2006). The two materials, in addition to air, mix and then are aligned inside the focus tube until exiting from the nozzle to atmosphere.

1.3 Research Motivation & Objective

AWJM can be used for numerous machining applications including slotting, turning, drilling and milling, making it a versatile machining process (H. Liu, 2004). As a result, there are numerous areas for research to improve or understand AWJM including modelling of wear, erosion or surface quality characterization. Next, operations including processes AWJM can perform such as drilling, turning, threading and more recently milling. Systems, which focuses on the high pressure pump, nozzle wear monitoring, nozzle location sensing. Research of other new applications such as hybrid machining with other conventional or non-conventional machining processes also exists. However, with the high pressure and velocities, small dimensions and numerous input parameters, AWJM becomes a very intricate process and therefore difficult to fully understand and predict. With the cutting process attributed primarily to the abrasive particles momentum at impact, predicting and understanding these velocities is a necessity to predicting erosion. To improve AWJM efficiency the material removal rate (MRR) must be optimized. An optimized nozzle will utilize the same inputs but have greater MRR or cut quality. This can only be achieved by fully understanding and optimizing the momentum transfer from the fluid energy to the abrasive particles.

The initial research objective is to accurately model the PASER 3 nozzle from Flow using ANSYS Fluent 12.1; to determine the effect of input pressure, particle size, shape factor, nozzle length and volume fraction of air in the fluid mixture (v.o.f.), have on the abrasive particle velocity. From the ANSYS model, these relationships and velocity profile output data of the fluid and abrasive will be used as input information to an erosion model. Succeeding with ElTobgy's modified erosion model and an updated abrasive particle velocity profile, versus an assumed constant, material erosion will be predicted, thereby reducing experimental requirements, time and mainly costs. To advance the erosion model research into an updated Ks – specific cutting resistance energy required to remove one unit of material – formulation is developed; this should improve accuracy in predication of depth of penetration (d.o.p) with a reduction in reliance on efficiency terms or other constants. Overall, with the combination of the two models, a reference guide illustrating d.o.p. prediction is created by means of a multi-layered surface plot dependent on mass flow rate of abrasive, feed rate and pump pressure. With minimal experiments, and variations in model inputs, a useful database can be generated and the depth of penetration of the abrasive into the work piece will be further understood and calculable.

1.4 Thesis Layout

The thesis is divided into seven main sections in addition to this introduction chapter, bibliography and appendixes. Chapter 2 describes abrasive waterjet machining processes including machining parameters and their effect on the cut quality, in addition to a survey of AWJ modelling techniques. Chapter 3 describes the computational fluid dynamics model developed to demonstrate the AWJ mixing head and nozzle. A thorough outline of the modelling approach including derivation of solvers, description of boundary conditions and model assumptions are included. Chapter 4 describes the erosion model formulation including a description of the methodology represented in the model, and derivation of each step in calculation throughout the predicted erosion. Chapter 5 outlines the results from the CFD model including confirmation of the effect of input parameters on the output velocity profile of the abrasive garnet. Chapter 6 initially describes the experimental tests that were conducted and outlines the effect of varied input parameters on depth of penetration and other cutting characteristics. Following that, the erosion model results are described and compared against experiments and reference literature to validate the model. Lastly, a conclusion section to recapitulate the main findings of the thesis is explained in chapter 7 and a future work section follows to describe where continued work exists.

2 Background Literature

Abrasive waterjet machining (AWJM) models must incorporate hydraulic, abrasive, mixing plus cutting settings and cut quality requirements; each category has requirements that must be identified (ElTobgy, 2007). When these parameters are not effectively selected the cutting results become poor. Most evident is the exaggeration of the AWJ limitations including stream lag demonstrated on the surface of the cut face shown in Figure 3.iv, cone or taper effects on the kerf width especially in corners, Figure 3.ii and fogging. Fogging prevents AWJM to have a mirror finish shown in Figure 3.i.

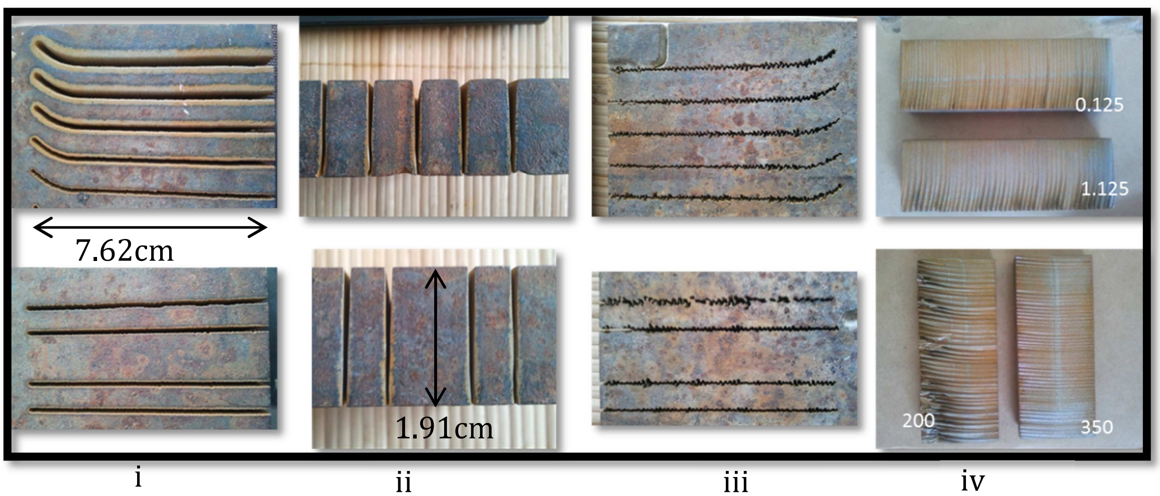

Figure 3: Cutting Limitations (i,ii,iii,iv)

Extensive research has been completed, attempting to understand the science of AWJ; improving the technology increases the application functionality of abrasive waterjet machining. For the erosion model to be effective the velocity profile of the particle must be accurately estimated. Liu et al. used a simplified geometry to model the turbulent mixture and concluded an initial region of rapid decay after the jet inlet; with smaller diameter particles jet decay occurs more rapidly.

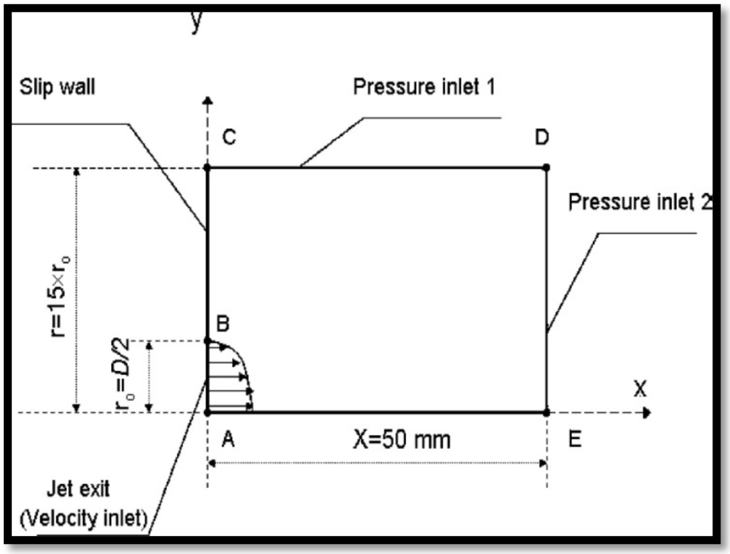

Figure 4: Simplified geometry (H. Liu, 2004)

Most significantly, Liu et al. described a "top-hat" profile for the jet flow that correlates well to the kerf formation geometry (H. Liu, 2004). The v-shaped kerf formation develops because as the abrasive material erodes through the work piece it loses energy, velocity and cannot erode to the same extent as before. Further, the "top-hat" profile describes the greatest velocity being concentrated in the center of the jet profile and tapering out radially. This promotes the v-shaped kerf because the abrasive particles closest to the nozzle wall travel with less velocity and also form the outer bound of the cut width; therefore, with less impacting velocity to generate erosion. Mostofa et al. described that a decrease in particle shape factor, increases erosion rate inside the focus tube. Further, the jet efficiency will decrease if the mass flow rate is too high due to a clogging effect in the nozzle decreasing the velocity of the abrasive. (Md. G. Mostofa, 2010). Ahmed et al. modeled the focus tube length to determine the effect on the velocity profile of the three phases near the central axis and found the optimized length of the focus tube to be 75mm (D.H. Ahmed, 2001). Tazbit et al. described the significance of air in the entrainment system. By monitoring the flow of air and particles into the system it was concluded that the volume distribution is 95% air, 4% water and 1% discrete mass phase. For volume of air >70% the mass flow rate of the abrasive particle has little influence on the acceleration process. Most significantly is the distance it takes to reach the equilibrium between phases; with 0% air 12cm, at 95% air volume the distance becomes 12m (A. Tazbit, 1996).

Zhu et. al developed a detailed description of the material removal rate through fracture erosion, which is dominated by the impacting force of the abrasive, rather than the secondary method of shearing (referred to as cutting in other models) by the lateral flow of the waterjet; this method dominated the fracture regime when materials are brittle. The MRR was estimated by determining the weight per sphere cap, with radius length of the shear crack and depth of the plastic zone. When machining titanium alloys, at high traverse rates and minimal depth of penetration, the cutting mechanism can be modelled such that it is dominated by the impact force rather than the cutting mechanism described by Zhu et al (Hongtao Zhu, 2009).

With high pressure and velocities, small dimensions and numerous input parameters AWJM becomes an intricate process and therefore difficult to fully understand and predict. With the cutting process attributed to the abrasive particles momentum at impact, predicting these velocities is a necessity for predicting cutting. Therefore, the research objective is to accurately model the PASER 3 nozzle from FLOW International using ANSYS Fluent 12.1; to determine the effect of input pressure - particle size, shape factor, nozzle length and volume fraction of air in the fluid mixture (v.o.f.) - on the abrasive particle velocity; then utilize that information in the numerical erosion model.

2.1 AWJM Parameters

With the numerous components associated with the AWJM process, several parameters emanate that must be understood and appropriately set to ensure effective cutting. Each category has requirements that must be identified. Hydraulic parameters include waterjet pressure and nozzle design; mainly diameter and nozzle length. Abrasive parameters include material, size, shape and flow rate.

Table 1: AWJ parameters

Parameters	**Range/Value**	**Effect on DOC**	**Effect on Kerf (width, quality, corners)**
Hydraulic Parameters			
• **WJ pressure**	100-600MPa	I	Cut taper decreases, roughness decreases
• **WJ nozzle diameter**	0.1-0.8mm	I	
Abrasive Parameters			
• **Material**	Garnet, glass bead, aluminum oxide, silica sand		
• **Particle size**	Mesh #30-120	Depends	Roughness has variable trend with a minimum
• **MFR**	2-10g/s	VM	No change on cut taper and roughness decreases as MFR increases
• **Particle shape**			
Mixing Parameters			
• **Mixing method**			
o **Forced**			
o **Suction**			
o **Suspension**			
• **Abrasive condition**			
• **Mixing chamber dimensions**			
Cutting Parameters			
• **Transverse Rate**		D	Cut taper and roughness increase as transverse rate increases
• **Standoff distance**		D	Cut taper increases
• **# Passes**		I	
• **Attack angle**	30-90 degrees		
o **Ductile**		VM	
o **Brittle**		I	

I≡Increase, D≡Decrease, VM≡Variable Trend w/ maximum, VD≡Variable Trend w/ minimum

Mixing characteristics include the method (forced or suction), condition (entrainment or slurry) and chamber dimensions. Cutting parameters include traverse rate, standoff distance, number of passes, attack angle and target material. Cutting results include cut depth, kerf width, and kerf quality. Table 1: AWJ parameters, prepared by ElTobgy summarized the range of values and trends associated with each of the parameters.

When these parameters are not effectively selected the cutting results become poor; most evident is the exaggeration of the AWJ limitations. Limitations include stream lag, cone or taper effects on the kerf width, especially in corners and fogging. Stream lag refers to the difference in location between the entry and exit location of the jet as it traverses across the work piece. The cone or taper effect is a result of the improper amount of cutting force; too much force causes a cone or blow-out effect, too little causes a taper effect. The fogging prevents AWJM to have a mirror finish. As the jet leaves the nozzle, the distance to the work piece is referred to as the stand-off distance. As this distance increases the jet diameter increases, which has particles entrained within it. Most of the particles are concentrated within the core of the jet, however, some that are near the outer bounds of the jet and shot-peen the surface causing a rough, unwanted surface finish.

These are the main limitations of AWJM demonstrating why the process parameters must be appropriately chosen to minimize these issues. Since the creation of AWJ, research attempting to understand the science and improve the application functionality has taken place.

2.2 AWJ Modelling

The hydrodynamic characteristics - including the velocity and pressure distributions - of AWJM must be fully understood to improve the nozzle design thereby improving MRR. As such, AWJM research efforts have been made experimentally, theoretically and more recently through various modeling techniques including finite element modelling and computational fluid dynamics.

2.3 Erosion Modelling

AWJM is a wear process described best by Finnie as the "attack of a surface by a solid particle entrained in a fluid system" (Finnie, 1960). During the erosion process, only the cutting force from the abrasive particles impacting the work piece is exerted, and the contact forces are responsible for decelerating the particles. Cutting from erosion occurs by means of micro-plastic deformation and brittle fracture described by Bitter and Finnie's work (ElTobgy, 2007). Plastic deformation is the process of displacing, or the cutting action of, an eroding particle experienced with ductile materials. Brittle material removal occurs by the intersection of cracks that propagate throughout the material from the point of impression due to the impact of the abrasive particle (Finnie, 1960). Hashish later combined these models and formulated a depth of penetration approximation, which ElTobgy modified to account for numerous particle impact on any surface, rather than a jet stream with a given mass flow rate.

2.3.1 Finnie Model for Ductile Erosion

Finnie developed a single particle erosion cutting model. Numerous assumptions were made including: the work piece material was ductile, the particle impacted a smooth flat surface, velocity, attack angle and material resistance are constant, elastic deformation is ignored and finally the length of contact between the work piece and the abrasive particle is significantly larger than the depth of cut.

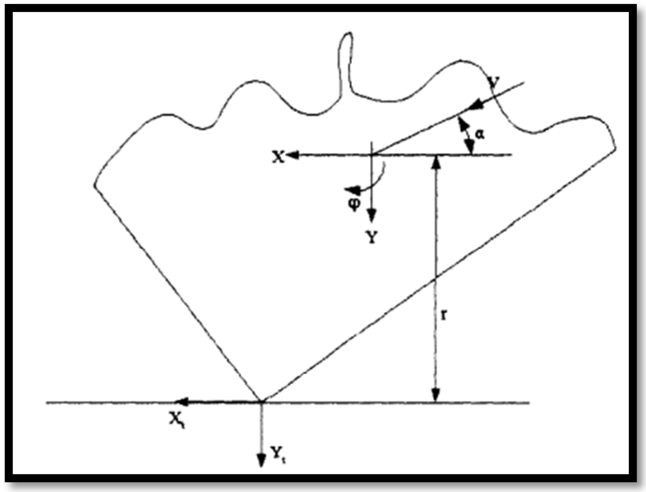

Figure 5: Initial particle position described by Finnie

Finnie derived the particle equations based off these assumptions as:

$$m_a\ddot{y} + \ \sigma_f\, K\gamma by = 0$$ Equation 2-1

$$m_a\ddot{x} + \ \sigma_f\, K\gamma by = 0$$ Equation 2-2

$$I\ddot{\varphi} + \ \sigma_f\, K\gamma bry = 0$$ Equation 2-3

Constant designations are velocity (v), impacting surface angle (∝), particle mass (m_a), particle width (b), ratio of vertical to horizontal force components (K=$\frac{F_v}{F_H}$), γ is the ratio of depth of contact (l) to the depth of cut (Y_t) and lastly the flow stress (σ_f) of the eroded work piece.

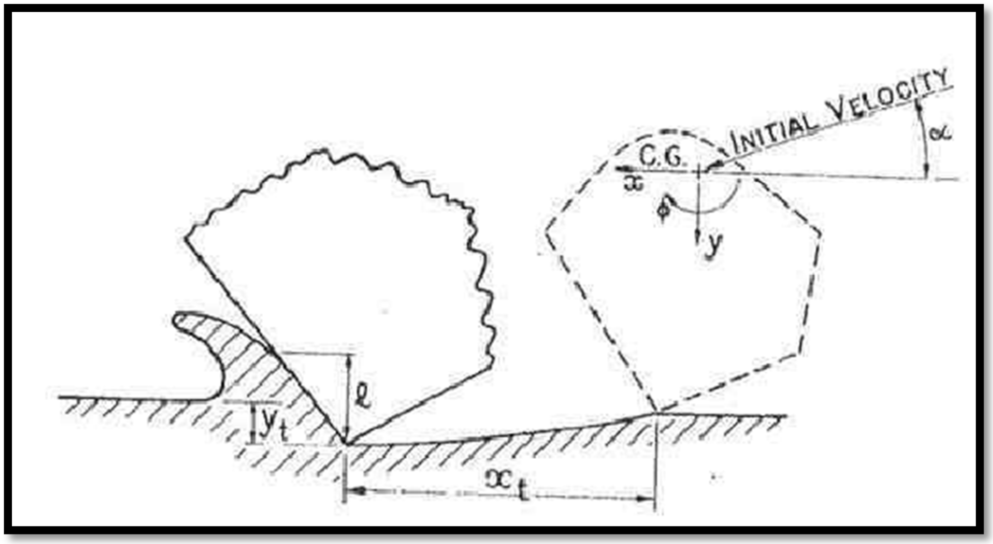

Figure 6: Contact illustration during erosion

Finnie described certain conditions for the cutting model, which were utilized in Hashish and ElTobgy's models. First $\propto \leq \alpha_o$ for the particle to enter the work piece; α_o is the initial impact angle, $\propto$ being the angle during erosion at the particular time step. As $\propto \geq \alpha_o$ the cutting stops because the particle velocity components become parallel to the surface; the two checks identifying when cutting stops are y=0 or $\dot{x}$=0. The final volume removal equations derived, with an experimentally determined K=2, are:

$$VOL = \frac{Mv^2}{2\sigma_f \gamma}[sin2\alpha - 3sin^2\alpha] \text{ when } \alpha < 18.5$$ Equation 2-4

$$VOL = \frac{Mv^2}{6\sigma_f \gamma}[cos^2\alpha] \text{ when } \alpha \geq 18.5$$ Equation 2-5

Because some particles will not cut, others will fracture and some will rebound off other particles and not impact the work piece, Finnie suggested reducing the volume removal rate by 50% and in comparison to experimental work, the model demonstrated effective for low impact angles. The 50% effective rate will be discussed in the Depth of

Erosion Prediction Model chapter; understanding and reducing the dependency on this factor was the basis for the new Ks formulation.

2.3.2 Bitter Model for Erosion

Bitter developed an erosion model based on the repeated deformation of the work piece material during collision. Different than Finnie, Bitter described the deformation to have two wear regimes. First, a deformation wear regime due to plastic deformation that occurs as a result of the plastic limit of the work material is being exceeded and the surface layer being removed. The second being governed by cutting as the particle impacts the surface and scratching, common to grinding (Bitter, 1962).

Bitter found the deformation and cutting zone to equal:

$$W_d = \frac{M(vsin\propto - v_{el})^2}{2\varepsilon_b} \quad , vsin(\propto) > v_{el} \qquad \text{Equation 2-6}$$

$$W_d = 0 \, , vsin(\propto) < v_{el} \qquad \text{Equation 2-7}$$

$$W_c = \frac{2M\acute{C}(vsin\propto - v_{el})^2}{\sqrt{vsin\propto}} \times [vcos - \frac{\acute{C}(vsin\propto - v_{el})^2\varphi^2}{\sqrt{vsin\propto}}], \propto \leq \propto_0 \qquad \text{Equation 2-8}$$

$$W_c = \frac{M\{v^2cos^2 \propto \; - K_1[vsin \propto - v_{el}]^{3/2}}{2\varphi_c} \quad , \propto \geq \propto_0 \qquad \text{Equation 2-9}$$

Variables that are different from Finnie's model include the deformation wear factor (ε_b) and the threshold velocity (v_{el}), which is calculated based on the Hertzian contact theory equation (ElTobgy, 2007). In the case between a sphere of diameter, $d_{1,}$ and a plane, $d_2 = \infty$, the contact area is a circular area of radius, r, represented below with maximum pressure and stress at the centre of the contact area (J. Shigley, Contact Stresses):

$$a = \sqrt[3]{\frac{3F}{8}\frac{\frac{1-v_1{}^2}{E_1}+\frac{1-v_2{}^2}{E_2}}{{}^1/_{d_1}\,{}^1/_{d_2}}}$$ Equation 2-10

$$p_{max} = \frac{3F}{2\pi a^2}$$ Equation 2-11

$$v_{el} = \frac{1.54{\sigma_y}^{5/2}}{\sqrt{\rho_p}}[\frac{1-{v_p}^2}{E_p}+\frac{1-{v_t}^2}{E_t}]$$ Equation 2-12

The elastic load limit (σ_y), particle density (ρ_p), Poission's ratios (v_p, v_t), modulus of elasticity of the particle and work piece (E_p, E_t), material dependant wear factor (φ_c) and constants $\acute{C}$ and K_1 are used to develop these wear relationships proposed by Bitter. The rebound velocity v_2 and constants $\acute{C}$ and K_1 can be determined by equations given in Bitter's paper, but φ_c and $\varepsilon_b$must be determined experimentally. These relationships lead to a total wear prediction as the sum of the two zones accounting for brittle and ductile materials.

2.3.3 Hashish Erosion Model

Hashish combined the efforts of both Finnie and Bitter and tried to improve their model shortcomings, such as the exclusion of particle shape and density, to develop a more well-rounded erosion model. This included accountancy of a single material erosion characterization property, characteristic velocity term of the particle, threshold velocity term and the effect of hydrodynamic loading, inertial loading and material resistance during erosion (M.Hashish, 1987). Hashish developed an analysis of erosion by a single particle superposed by hydrodynamic loading for the development of the site model

(Hashish, A Modelling Study of Metal Cutting with Abrasive Waterjets, 1984). Hashish described an upper cutting erosion zone where particles impacting at small angles were responsible for the cutting (h_c); only a portion (c) of the jet diameter was attributed to effective cutting. This is a continuation of the mentality described by Finnie that not all particles will effectively erode the work piece and therefore an efficiency term is required. In the lower region, erosion was due to deformation as the plastic limit was exceeded. Similar to Bitter, the two zones were summed together to achieve the total depth of cut.

2.3.3.1 Hashish - Cutting Wear Zone

Assumptions from Finnie's model to yield Hashish's depth due to cutting wear include the particle velocity over the range of h_c is assumed constant since it pertains to a shallow depth. The angle of impact, α, will be assumed to vary linearly from element to element yielding the relationship:

$$\frac{d \propto}{\propto_1} = \frac{-dx}{cd_j} \quad \text{Equation 2-13}$$

Lastly, the jet is assumed to be two-dimensional and have width equal to d_j. The volume removal relationship based on these assumptions for an abrasive flow rate, $\dot{m}$, is:

$$\dot{\delta v} = \frac{d\dot{m}V^2}{4\sigma_f}(sin2\alpha - 3sin^2\alpha) \quad \text{Equation 2-14}$$

$$\dot{\delta v} = dhud_j \, , d\dot{m} = (\frac{\dot{m}}{d_j})dx \quad \text{Equation 2-15}$$

Using equations from 2.13 and assumptions listed 2.12, $\frac{dh}{d\propto}$ becomes:

$$\frac{dh}{d\propto} = -\frac{c\dot{m}V^2}{4\sigma_f d_j \alpha_1 u}(sin2\alpha - 3sin^2\alpha)$$ Equation 2-16

Integrating between $h = 0, \propto = \propto_1$ to $h = h_c, \propto = 0$ and assuming $(sin2\alpha - 3sin^2\alpha) = 2\propto$

$$h_c = \frac{c\dot{m}V^2\alpha_1}{4\sigma_f d_j u}$$ Equation 2-17

The linear relationship between $\propto$ and d_j is shown in Figure 7.

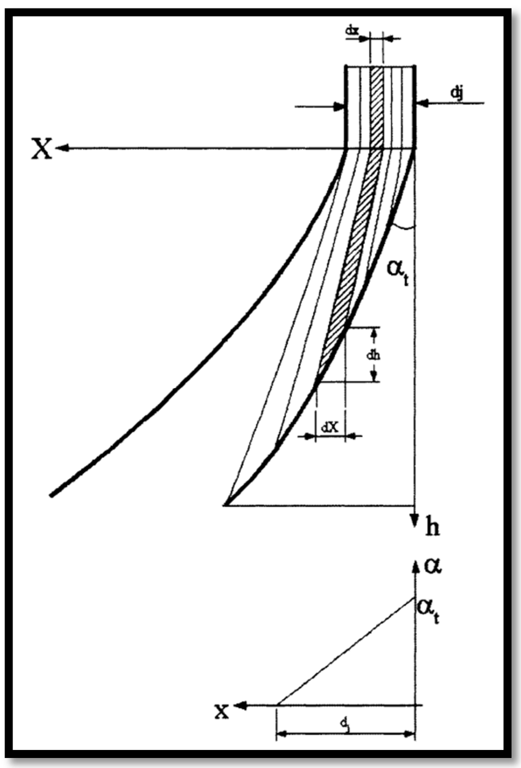

Figure 7: Cutting wear erosion schematic

2.3.3.2 Hashish - Deformation Wear Zone

Bitter described the material volume removal from deformation as:

$$\delta v = \frac{1}{2}\frac{m(V sin \propto \; - V_c)^2}{\epsilon} \qquad \text{Equation 2-18}$$

With critical velocity (V_c) assumed small compared to V, $sin \propto \approx 1$ and energy required removing the unit volume (ϵ), the volume removal rate equation becomes:

$$\dot{\delta v} = \frac{1}{2}\frac{mV^2}{\epsilon} \qquad \text{Equation 2-19}$$

Because $\delta v = \dot{h} A_c$ and $A_c = (\pi/4){d_j}^2$, recalling only $(1-c)\dot{m}$ is responsible for deformation wear and lastly assuming the velocity does not change the depth of cut for deformation is:

$$h_d = \frac{2(1-c)m\dot{V}^2}{\pi d_j \epsilon u} \qquad \text{Equation 2-20}$$

The total depth of cut is the summation of the two zones. Limitations to the model include the exclusion of particle size and shape and assumed velocities. These are considered in Hashish's modified model for erosion.

2.3.3.3 Modified Hashish Erosion Model

Improvements to Hashish's first model would be the inclusion of the characteristic velocity (C_k) that associates particle and material characteristics, such as roundness factor (R_f) and target material flow stress (σ_f), to the characteristic velocity and is calculated below. In addition, the effect of kerf wall drag and threshold velocity is considered (Hashish, A Model for Abrasive-Waterjet (AWJ) Machining, 1989).

$$C_K = \sqrt{\frac{3\sigma_f {R_f}^{3/5}}{\rho_p}} \qquad \text{Equation 2-21}$$

The improved model, based on Hashish's earlier work described, begins with the assumption of a uniform distribution of the abrasive particle velocity over the cross-sectional area of the jet; a real distribution of the particle velocity is developed from CFD to counter this assumption in the CFD Model section later.

$$\dot{\delta v} = \frac{7}{\pi}\frac{\dot{m}}{\rho_p}\left(\frac{V}{C_K}\right) sin2\alpha\sqrt{sin\alpha} \qquad \text{Equation 2-22}$$

The assumptions from Equation 2-15 and $sin\alpha \approx \propto$ Equation 2-22 becomes:

$$dhud_j = \frac{14}{\pi}\frac{\dot{m}}{\rho_p}\left(\frac{d_x}{d_j}\right)\left(\frac{V_0}{C_K}\right)^{2.5} {\alpha_t}^{1.5} \qquad \text{Equation 2-23}$$

Following that,

$$\alpha_t = \frac{1}{(\frac{14\dot{m}}{\pi\rho_p u {d_j}^2})^{2/5}\frac{V_0}{C_k}} \quad (2.19)\ tan \propto_0 sin \propto_0$$

$$= \frac{\frac{3\pi R_f 0.6}{14\gamma}}{\sqrt{\frac{V_o}{C_k}}} \qquad \text{Equation 2-24}$$

$$\gamma = 1 + \frac{mr^2}{I}, I = 0.5mr^2$$ Equation 2-25

Taking into account the kerf wall drag as a frictional force ($F_f = C_f A_w \frac{\rho V_0{}^2}{2}$) over the area $A_w = \frac{\pi d_j}{2} h$; calling $K_w = \frac{\pi C_f}{4\dot{m}_t} d_j \rho V_0 = \frac{C_f}{d_j}$ then $V = V_0(1 - K_w h)$ and finally after integration the depth due to cutting becomes:

$$h_c = \frac{(1 + 1.5K_w H)^{2/3} - 1}{K_w(1 + 1.5K_w H)^{2/3}}, H$$
$$= \frac{Cd_j}{2.5}(\frac{14\dot{m}}{\pi u \rho_p d_j{}^2})^{2/5} \frac{V_0}{C_k}$$ Equation 2-26

2.3.3.4 Modified Hashish - Deformation Wear Zone

The deformation wear zone does not change from Bitter's original description except for the velocity described with the kerf wall considerations. The depth of cut due to deformation becomes:

$$h_d = 1/(\frac{\pi d_j \sigma u}{2C_1 \dot{m}(V_0 - V_e)^2} + \frac{C_f}{d_j} \frac{V_0}{(V_0 - V_e)})$$ Equation 2-27

2.4 Simulation Modelling

2.4.1 Hashish's Non-dimensional Prediction

From the derivation defined above, Hashish continued his work and rewrote the total depth of cut in a non-dimensional format (Hashish, A Model for Abrasive-Waterjet

(AWJ) Machining, 1989). This formed the basis for ElTobgy's simulation model. The equations are:

$$N_c = \frac{h_c}{d_j} \quad \text{Cutting wear d.o.c. number}$$

$$N_d = \frac{h_d}{d_j} \quad \text{Deformation wear d.o.c. number}$$

$$N_1 = \frac{\rho_p u {d_j}^2}{\dot{m}} \quad \text{Traverse number}$$

$$N_2 = \frac{\rho_p {V_0}^2}{\sigma} \quad \text{Relative strength number}$$

$$N_3 = \frac{\rho_p {V_e}^2}{\sigma} \quad \text{Minimum relative strength number}$$

$$N_4 = C_f \quad \text{Coefficient of wall drag}$$

$$N_5 = 3{R_f}^{3/5} \quad \text{Particle shape number}$$

$$N_6 = \frac{V_e}{V_0} = \frac{N_3}{N_2} \quad \text{Threshold velocity number}$$

$$N_c = \frac{\sqrt{N_2/N_5}}{\frac{(\pi/14)^{2/5}}{C}{N_1}^{2/5} + N_3/N_5} \qquad \text{Equation 2-28}$$

$$N_d = \frac{(1-N_6)^2}{\frac{\left(\frac{\pi}{2}\right)}{C_1}\left(\frac{N_1}{N_2}\right) + N_4(1-N_6)} \qquad \text{Equation 2-29}$$

C & C_1 are constants determined experimentally as zero and one. Hashish describes a prediction procedure initiated by estimating the particle velocity from a simplified

Bernoulli flow equation, including a loading ratio between the water flow rate and the abrasive, and suggests an efficiency term for the flow as well. In this case, the constant C is a fraction to account for the partial involvement of the total jet diameter where cutting occurs, versus C_1 where deformation occurs. Following that the non-dimensional numbers are calculated. The impact angle is calculated and compared to the critical angle, in which cutting would stop.

$$\propto_t = \frac{a_1 {N_1}^{2/5} + {}^{N_3}/_{N_5}}{{}^{N_2}/_{N_5}} \qquad \text{Equation 2-30}$$

$$\propto_0 = \left(\frac{\pi}{14\gamma}\frac{{N_5}^{3/2}}{N_2}\right)^{1/3} \qquad \text{Equation 2-31}$$

Given that $a_1 = ({}^{\pi}/_{14})^{2/5}$, $C = 1 - {}^{\propto_t}/_{\propto_0}$ certain conditions must be met including: $\propto_t < \propto_0$ and $V_0 sin \propto_t > V_e$ otherwise cutting deformation will not take place and $h_c = 0$.

2.4.2 ElTobgy's New Approach

ElTobgy, based on Hashish's non-dimensional derivation, analyzed a smaller scale form of the jet width separated down to a per particle erosion simulation. A numerical simulation was then created to resolve the force components, shown in Figure 8, of a particle impacting any surface.

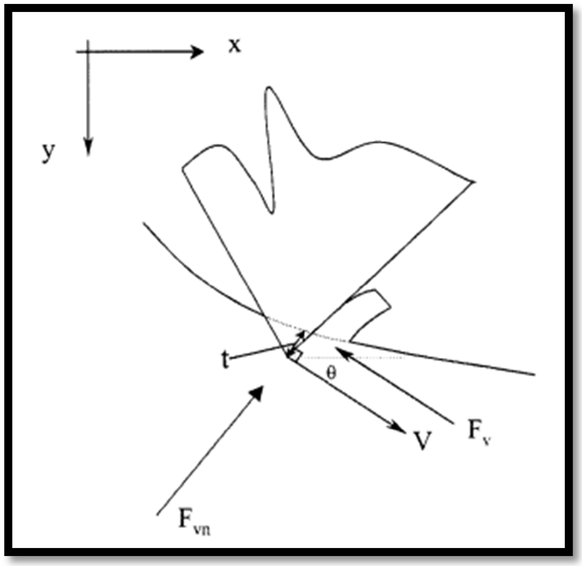

Figure 8: Force components of particle hitting curved surface

ElTobgy used a work piece specific cutting resistance constant (K_s), estimated at 30-40 times greater than typical orthogonal cutting, determined from the FEA model, but exaggerated because of model restrictions. Using K_s the force components are (M. ElTobgy):

$$F_v = K_s bt, F_{vn} = CF_v$$ Equation 2-32

$$m\ddot{x} = K_s bt[\cos(\theta) + csin(\theta)]$$ Equation 2-33

$$m\ddot{y} = K_s bt[\sin(\theta) + ccos(\theta)]$$ Equation 2-34

$$I\ddot{\varphi} = K_s btr[\cos(\theta) + csin(\theta)]$$ Equation 2-35

With $\theta = \arctan({}^{v_x}/_{v_y})$, $k = x + r\varphi$, $l = y + r\varphi$ a numerical simulation based on the central difference algorithm, shown in Equation 2-36, the single particle erosion is solved (Li).

$$D_0\mathrm{u(x)} = \frac{u(x+h) - u(x-h)}{2h} = \acute{u}(\mathrm{x}) + \frac{h^2}{6}u'''(\xi)$$ Equation 2-36

$$M\ddot{U} = [F]$$ Equation 2-37

$$A_t = -[M][F]_t$$ Equation 2-38

$$v_t = v_{t-1} + dtA_t$$ Equation 2-39

$$u_t = u_{t-1} + dtV_t$$ Equation 2-40

To calculate the penetration depth ElTobgy made some assumptions to Hashish's model described in Equation 2-26 and Equation 2-27, and reworked the d.o.p. to four non-dimensional numbers shown below (ElTobgy, 2007). This was used to calculate h in Equation 2-41.

$$\frac{h}{d_j} = 0.282c\sqrt{\frac{N_4}{N_2N_3}} + \frac{(1-N_1)^2}{\frac{N_2N_3}{(1-c)} + C_f(1-N_1)}$$ Equation 2-41

$$N_1 = \frac{V_{cr}}{V} = 0$$ Equation 2-42

$$N_2 = \frac{\pi}{2}\frac{\varepsilon {d_j}^2}{\dot{m}_a V_p}$$ Equation 2-43

$$N_3 = \frac{U_t}{V_p}$$ Equation 2-44

$$N_4 = \frac{\varepsilon}{\sigma}$$ Equation 2-45

Assumptions suggested by ElTobgy consist of V_{cr} and C_f equal zero; constants ε and c to be determined experimentally and are described later. The process, similar to all previous erosion models described, are dependent on a velocity profile of the jet and mainly the abrasive particle - be it the jet profile determined experimentally, theoretically (plus efficiencies), or modelled using computational fluid dynamics (CFD). To date these erosion models have all assumed constant velocity across the jet diameter, however this has been more recently described as a "top-hat" profile, with the highest velocity concentrating in the core of the jet. Using Hashish and ElTobgy's frame work, the erosion model will be modified to include this profile, and a more comprehensive specific-cutting resistance accounting for strain hardening and secondary cutting.

Strain hardening, also known as cold working, is the process of plastic straining a work piece below the recrystallization temperature in the plastic region of the stress-strain curve. By loading a material to its plastic region then releasing the load, the work piece becomes plastically deformed (ε_p). If the load is then reapplied the work piece will be elastically deformed to the same point but by an elastic strain, ε_e. The material has a higher yield point, becomes less ductile and is now strain hardened. When an abrasive particle strikes the work piece it may not be of sufficient velocity to crack or plastically erode the part by cutting; it will however plastically deform it causing a compression and thereby strain hardening the area. This will have two direct effects on the work piece: first no erosion takes place, but secondly the localised area may now require more energy to erode in the future requiring multiple impacts to propagate a crack because as the area is repeatedly cold worked (J. Shigley, Strength and Cold Work).

Secondary cutting is the attitude that some particles may be positioned in the jet stream away from impaction of the work piece, and some may rebound off the work piece and be re-entrained into the jet stream. In either case, the particle is accelerated and repositioned to an ideal location in the jet stream for impact of the work piece, where it can then cause erosion. The initial schematic of the jet stream with mass flow, $\dot{m}_f$, does not account for any secondary, effective cutting by dm further down the erosion contact length. By incorporating the effect of change in velocity and feed rate of the nozzle the updated Ks formulation will have allowance for the effect of strain hardening and secondary cutting.

3 CFD Model

3.1 Computational Fluid Dynamics Modeling

To ensure the erosion model is effective, the velocity profile of the particles upon exit of the nozzle to atmosphere must be accurately estimated. Whether it is determined by approximation via a mass-momentum balance based on the loading ratio between the water and the abrasive mass flow rates, experiments utilizing laser Doppler velocimeters (LDV) or other camera types, or more recently through computational fluid dynamic modeling techniques, the hydrodynamic characteristics must be accurately determined.

AWJM involves a three phase mixture made up of air, water and a discrete mass phase. These phases mix together at high velocity (200-900m/s) in a nozzle of very fine dimensions. Understanding the physics behind such an advanced flow is very difficult. Moreover experiments are timely, costly and difficult to attain full understanding. As such, numerous researchers have tried to model the AWJ mixing operation using CFD.

Liu et al. (2004) used a simplified geometry to model the turbulent mixture. They concluded an initial region of rapid velocity decay after the jet inlet; with smaller diameter particles jet decay occurs more rapidly. Particle size had little effect on the velocity decay downstream. Most significantly, Liu et al. described a "top-hat" profile for the jet flow that correlates well to the kerf formation geometry.

Mostofa et al. (2010) developed erosion relationships inside the focus tube. It was concluded that the focus tube is responsible for accelerating the particle and that decrease in particle shape factor increases erosion rate inside the tube. Moreover, the jet efficiency will decrease if the mass flow rate is too high, as the abrasive velocity decreases. Ahmed et al. (2001) modeled the focus tube length and compared the effect the volume ratio of air, has on the velocity profile.

J. Wang modelled AWJM at ultra-high pressure with a 1/7 power law distribution of the velocity profile upon exit from the nozzle. The focus was to model the jet decay rate of the abrasive particle at any location within the nozzle dependent on the particle size. Wang's CFD modelled developed was compared to a CFD model previously developed and validated experimentally by Liu (Wang, 2009).

Tazbit et al. (1996) described the most noteworthy experimental analysis for AWJM describing the significance of air in the entrainment system. By monitoring the flow of air and particles into the system this research was able to conclude that the volume distribution is 95% air, 4% water, and 1% discrete mass phase; this dramatically affects the velocity output profile discussed in CFD Model results by dramatically changing the fluid mixture density. First, while modeling water and mass only, Tazbit et al. (1996) demonstrated the effects of drag, virtual mass, wall shear and gravitational forces, proving minimal in comparison to the effect of air. When volume of air in the fluid mixture is >70% the mass flow rate of the abrasive particle has little influence on the acceleration process. The mass flow rate of abrasive is so small it negligibly decelerates the water-air mixture as it is accelerated down the nozzle. Based on the nozzle length in the experiment the abrasive particle velocity at this exit location was only 60% in comparison to the water model abrasive exit velocity. Most significantly is the distance it takes to reach the equilibrium between phases due to momentum exchange; with 0% air 12cm, at 95% air volume the distance becomes 12m.

3.2 Geometry

ANSYS Fluent 12.1 is used to model this steady-state, turbulent, three-phase mixture; CFD as the physics preference and Fluent for the solver preference. The AWJ mixing unit consists of a main inlet for water-air to enter through an orifice, a mass inlet for abrasive-air entry, a mixing chamber and a focusing tube. This setup is illustrated in Figure 9.

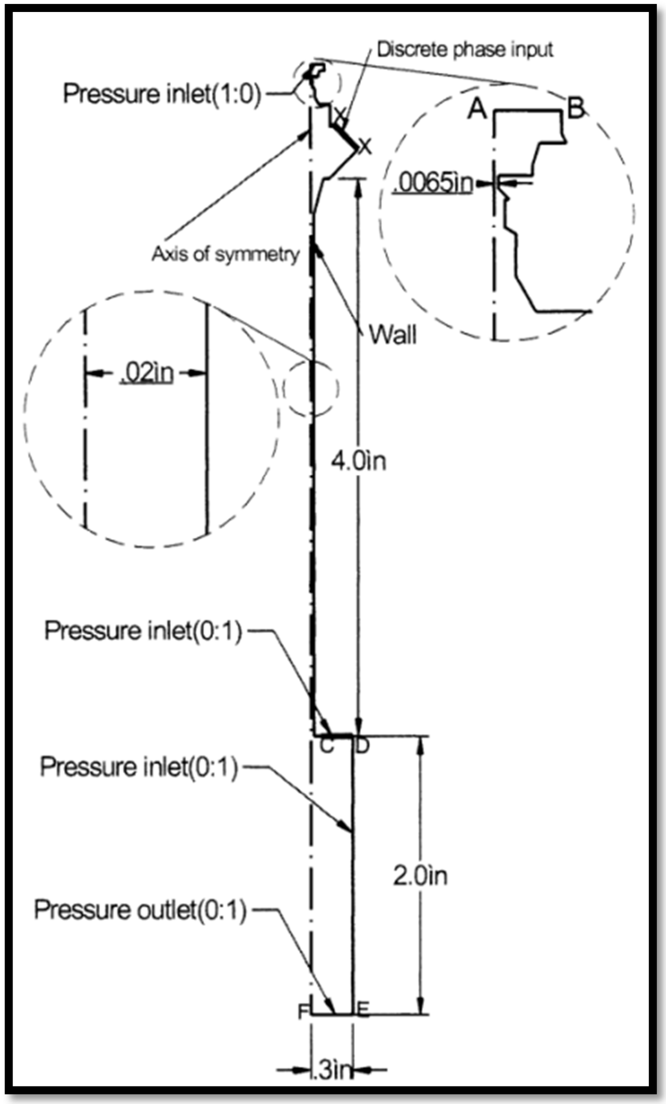

Figure 9: CFD model setup

The orifice and the focus tube length are the only inputs regarding the geometry that changed throughout the analysis of the AWJ nozzle head. Initially the orifice diameter is 0.013'' (0.033cm), the focus tube diameter is 0.04'' (0.1016cm), length is 4'' (10.16cm) and the atmosphere region is 2'' with a diameter of 0.6''. The region is set up symmetrically with an axis line A-F to reduce computational effort.

3.3 Mesh

The stability of the ANSYS Fluent solver, in regards to solution convergence, is highly dependent on the mesh setup. Settings utilized in the model included advanced sizing on curvature and proximity, fine relevance center with high smoothing and slow transitions. Cells across the fluid gap needed to be greater than 90. This is incredibly fine considering the orifice is 0.0065 inches (0.01651cm) to begin. Therefore, the average element length in the inlet region is 5E-5 in (0.000127cm). Lastly, a post inflation algorithm was used to total approximately 400000 nodes and elements. A list of meshing terms can be referenced in Appendix D - Mesh Method Settings Dialog Box With reference to Figure 9, the named locations in the mesh system are tabulated below in Table 2:

Location	Type	Phases	Surface
Main inlet	Pressure inlet	95% air, 5% water	A-B
Mass inlet	Mass flow inlet	100% air	X-X
Pressure inlet 1	Pressure inlet	100% air	D-E
Pressure inlet 2	Pressure inlet	100% air	C-D
Pressure outlet	Pressure outlet	95% air, 5% water	F-E
Walls	Wall, no-slip		All others
Symmetry	Symmetry axis		A-F

Table 2: CFD Boundary conditions

3.4 Model Setup & Boundary Conditions

The modeling approach for the AWJ nozzle uses an Eulerian model for the multi-phase flow in conjunction with a $k-\epsilon$ turbulence model; k refers to the turbulence kinetic energy and ϵ refers to the turbulence dissipation energy. The Eulerian model is the most complex of the multi-phase models solving 'n' momentum and continuity equations for each phase; coupling is achieved by pressure and interphase exchange coefficients obtained through use of kinetic theory (ANSYS, 2009). Due to the difficulty of attaining convergence, initially a single phase water model is accurately attained. Following that, the multiphase water-air flow is modeled. Lastly, once the flow is steadily approaching convergence, the discrete-mass phase of the abrasive garnet material is added into the flow via a mass-inlet spatially distributed over the inlet area and updated after 400 iterations. Following that, updating the frequency then occurred every 25 iterations until convergence.

3.5 Eulerian Multi-phase model

ANSYS uses two approaches to modeling multi-phase flow. The Euler-Lagrange approach and the Euler-Euler approach; the first is used in this model. Euler-Euler models the phases as interpenetrating continua described as a phasic volume; phasic meaning there must be at least one phase in the volume at any time and the fraction of phases contained within a volume must sum to one. With the Euler-Lagrange case, the fluid phase is treated as a continuum by solving Navier-Stokes equations and the dispersed phase is solved by tracking a large number of particles (ANSYS, 2009). The critical assumption is that the discrete phase material (DPM) occupies a small percentage of the volume (<10%). The Euler-Lagrange approach is more ideal for modelling conditions where particle phase volumes are low and Lagrangian framework is ideal; i.e. when individual particle history is required.

The Eulerian model is the most complex multiphase model solving the continuity equations for each phase; the volume fraction of each phase is denoted by $\propto_q$. Conservation of mass and momentum equations for the q^{th} phase are described by Fluent below:

$$\frac{\partial}{\partial_t}\left(\alpha_q\rho_q\right) + \nabla\cdot\left(\alpha_q\rho_q\vec{v}_q\right) = \sum_{p=1}^{n}(\dot{m}_{pq} - \dot{m}_{qp}) + S_q \qquad \text{Equation 3-1}$$

$$\frac{\partial}{\partial_t}\left(\alpha_q\rho_q\overrightarrow{v_q}\right) + \nabla\cdot\left(\alpha_q\rho_q\vec{v}_q\overrightarrow{v_q}\right)$$
$$= -\propto_q \nabla_p + \nabla\cdot\overline{\overline{\tau_q}} + \alpha_q\rho_q\vec{g}$$
$$+ \sum_{p=1}^{n}(\dot{\vec{R}}_{pq} + \dot{m}_{pq}\overrightarrow{v_{pq}} - \dot{m}_{qp}\overrightarrow{v_{pq}}) + (\overrightarrow{F_q} \qquad \text{Equation 3-2}$$
$$+ \overrightarrow{F_{lift,q}} + \overrightarrow{F_{vm,q}}$$

Where $\sum_{q=1}^{n}\propto_q = 1$. The volume fraction represents the space occupied by each phase. The control volume must be occupied by a phase, or multiple, but cannot be void. The conservation equations are solved by collaboratively averaging the local instantaneous balance of phases, using the implicit time discretization; the implicit time discretization uses the current time step to solve the scalar transport equation for secondary-phase volume fractions at each step (ANSYS, 2009).

The foremost limitation of volume of fluid (VOF) models is with large velocity differences between phases, the accuracy of the velocities computed near interfaces can be adversely affected (ElTobgy, 2007). The Eulerian model requires more computational effort, but accuracy is the highest. It also considers interphase drag laws and in AWJM there is little distribution in the particle size, as such the mixture model is not required. There are numerous other parameters that must be considered which are outlined in section 16.2.2 Model Comparison of the ANSYS Theory Guide, among other sections that describe multi-phase flow and the inclusion of a discrete mass phase.

3.6 Viscosity turbulence model

The realizable $k-\epsilon$ turbulent model has two important advantages over the standard and RNG model. First, a new formulation for the turbulent viscosity, μ_t, and second a new transport equation for the dissipation rate (ϵ) derived from the exact equation for the transport of the mean-square vorticity fluctuation; this improves the accuracy for rapidly strained flows. “Realizable” emphasizing the mathematical constraints on the Reynolds stresses being satisfied (ANSYS, 2009).

The transport equations for k & ϵ are:

$$\mu_t = \rho C_\mu \frac{k^2}{\epsilon} \quad and\ C_\mu = \frac{1}{A_0 + A_s \frac{kU}{\epsilon}} \qquad \text{Equation 3-3}$$

$$\frac{\partial}{\partial_t}(\rho k) + \frac{\partial}{\partial x_j}(\rho k u_j) = \frac{\partial}{\partial x_j}\left[\left(\mu + \frac{\mu_t}{\sigma_k}\right)\frac{\partial k}{\partial x_j}\right] + G_k + G_b + \rho\epsilon - Y_M + S_k \qquad \text{Equation 3-4}$$

$$\frac{\partial}{\partial_t}(\rho \epsilon) + \frac{\partial}{\partial x_j}(\rho \epsilon u_j) = \frac{\partial}{\partial x_j}\left[\left(\mu + \frac{\mu_t}{\sigma_\epsilon}\right)\frac{\partial \epsilon}{\partial x_j}\right] + \rho C_1 S\epsilon - \rho C_2 \frac{\epsilon^2}{k + \sqrt{v\epsilon}} + C_{1\epsilon}\frac{\epsilon}{k}C_{3\epsilon}G_b + S_\epsilon \qquad \text{Equation 3-5}$$

With $C_1 = \max\left[0.43.\frac{n}{n+5}\right], n = S\frac{k}{\epsilon},\ S = \sqrt{2S_{ij}S_{ij}},\ G_k$ represents the generation of turbulent kinetic energy, G_b is the generation due to buoyancy, Y_M is the contribution of the fluctuating dilation in compressible turbulence to the overall dilation rate. σ_ϵ & σ_k are the turbulent Prandtl numbers and $S_k,\ S_\epsilon$ are user-defined source terms equal to zero in this case. The eddy viscosity is computed as $\mu_t = \rho C_\mu \frac{k^2}{\epsilon}$ and model constants are $C_{1\epsilon} = 1.44, C_2 = 1.9, \sigma_k = 1.0, \sigma_\epsilon = 1.2$.

3.7 Dense Discrete Phase Model

Using an inert particle, the force balance is calculated by integrating the balance in the Lagrangian reference frame on the particle equal to:

$$\frac{du_p}{dt} = F_D(u - u_p) + \frac{g_x(\rho_p - \rho)}{\rho_p} + F_x$$ Equation 3-6

F_x is the additional acceleration term (force/unit particle mass) and $F_D(u - u_p)$ is the drag force per unit particle mass. F_D & Re are described below:

$$F_D = \frac{18\mu}{\rho_p {d_p}^2}\frac{C_D Re}{24}, Re \equiv \frac{\rho d_p |u_p - u|}{\mu}$$ Equation 3-7

For particles with shape factor of 0.3-0.9, a drag coefficient (C_D) is modeled as:

$$C_D = \frac{24}{Re_{sph}}\left(1 + b_1 {Re_{sph}}^{b_2}\right) + \frac{b_3 Re_{sph}}{b_4 + Re_{sph}}$$ Equation 3-8

$$b_1 = \exp(2.3288 - 6.4581\varphi + 2.4486\varphi^2$$

$$b_2 = 0.0964 + 0.5565\varphi$$

$$b_3 = \exp(4.905 - 13.8944\varphi + 18.4222\varphi^2 - 10.2599\varphi^3$$

$$b_1 = \exp(1.4681 + 12.2584\varphi - 20.7322\varphi^2 + 15.8855\varphi^3$$

The drag coefficient model was created from Haider and Levenspiel work (ANSYS, 2009). The shape factor is defined as $\varphi = {}^{s}/_{S}$, s is the surface area of a sphere having the same volume as the particle and S is the actual surface area.

Using unsteady particle tracking with appropriate particle time step of 1E-4s, two-way turbulence coupling and interaction with the continuous phase - initially update after 400 iterations of the continuous phase, then increasing frequency to 25 iterations as the solution converges - the discrete phase model is accurately modeled. Moreover, the injection of discrete phase is spatially distributed over the mass inlet surface with an arbitrary 10m/s inlet flow, particle size, shape and material properties designated. The Eulerian multiphase model uses a phase coupled "SIMPLEC" algorithm for pressure-velocity coupling in a segregated fashion; a flow chart is shown in Figure 10 illustrating the solver procedure (Kelecy, 2008).

3.8 Solver Solution Method

The AWJ nozzle mixture is modeled in Fluent using a pressure-based, steady-state, planar 2D model; the discrete phase cannot be modeled with a density-based solver. The multiphase model is a Eulerian three-phase mixture, two phases being Eulerian and one is the dense discrete phase. The viscous model is the realizable $k - \epsilon$ turbulent mixture model with enhanced wall treatment to appropriately model the boundary layer. The boundary condition types have been previously described; details are outlined in the Appendix E – ANSYS Fluent Parameters.

The Eulerian multiphase model uses a phase coupled "SIMPLEC" algorithm for pressure-velocity coupling in a segregated fashion; a flow chart is shown in Figure 10 (Kelecy, 2008).

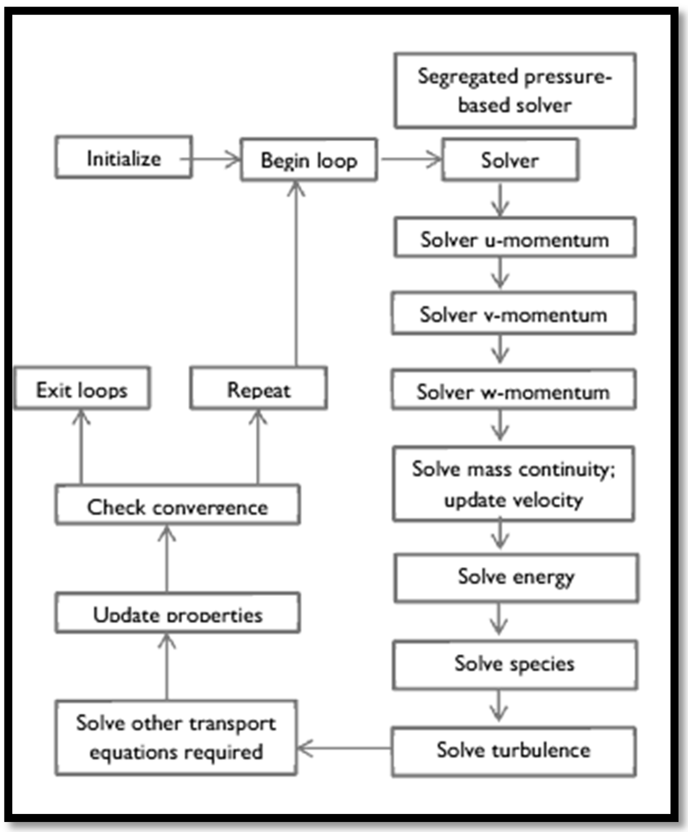

Figure 10: Fluent segregated solution

3.9 Turbulence Flow Conditions

Specifying the turbulence quantities prevents impediment of the solver. High levels of turbulence are generated within shear layers, versus the turbulence that is created at flow boundaries; however ensuring values prevents unphysical solution convergence.

Turbulence intensity (I) is the ratio of the root-mean-square of the velocity fluctuations, u', to the mean flow velocity, u_{avg} and is modeled as:

$$I \equiv \frac{u'}{u_{avg}} = 0.16(Re_{D_H})^{-1/8} \qquad \text{Equation 3-9}$$

Turbulence intensity can be as high as a few percent when Reynolds number is >50000; in this model it is approximately 3.38%. The turbulent length scale, l, is a physical quantity related to the size of the large eddies ($l = 0.07L$). The turbulent viscosity ratio, ${}^{\mu_t}/_{\mu}$, is proportional to the turbulent Reynolds number ($Re_t \equiv k^2/\epsilon v$) typically in the range of 100 to 1000. The modified turbulent viscosity relationship is $\tilde{v} = \sqrt{\frac{3}{2}} u_{avg} I l$. Finally, the turbulent kinetic energy, k and dissipation rate, ϵ, are: $k = \frac{3}{2}(u_{avg} I)^2$ and $\epsilon = {C_\mu}^{3/4} \frac{k^{3/2}}{l}$. Lastly, C_μ, is an empirical constant equal to 0.09 approximately for the turbulence model described above (ANSYS, 2009).

Final model considerations include: a supersonic/initial gauge (static pressure) boundary condition on the main inlet must be stipulated for supersonic flow if the solution is initialized on the pressure inlet, which is the case for this model. Initially this is set below the gauge pressure at the inlet, to assist convergence and then set equal to the inlet gauge pressure once stability in the solver has been realized. The inlet pressure value is used with the specified stagnation value to calculate the initial pressure differences based of the isentropic relationships for compressible flow.

3.9.1 Model Assumptions

Recapitulating model assumptions below:

i. Air volume is 95%
ii. Axis-symmetric flow (computational reduction)
iii. No temperature change
iv. No vacuum at any point
v. No-slip for water and air with wall
vi. No particle break up for DMP

4 Depth of Erosion Prediction Model

The erosion prediction numerical simulation is formulated based on ElTobgy's erosion model in 2.4.2, incorporated with a more accurate formulation of the specific cutting resistance (K_s) of the work piece material and is summarized below.

$$F_v = K_s bt, F_{vn} = CF_v \qquad \text{Equation 4-1}$$

$$m\ddot{x} = K_s bt[\cos(\theta) + csin(\theta)] \qquad \text{Equation 4-2}$$

$$m\ddot{y} = K_s bt[\sin(\theta) + ccos(\theta)] \qquad \text{Equation 4-3}$$

$$I\ddot{\varphi} = K_s btr[\cos(\theta) + csin(\theta)] \qquad \text{Equation 4-4}$$

$$M\ddot{U} = [F] \qquad \text{Equation 4-5}$$

$$A_t = -[M]^{-1}[F]_t \qquad \text{Equation 4-6}$$

$$v_t = v_{t-1} + dtsA_t \qquad \text{Equation 4-7}$$

$$u_t = u_{t-1} + dtsV_t \qquad \text{Equation 4-8}$$

ElTobgy's model was based on Hashish's non-dimensional derivation, which analyzed a smaller scale form of the abrasive waterjet width and associated mass for that jet area, separated down to a per particle erosion simulation. Returning to the K_s formulation later, the resultant cutting force is estimated, in Equation 4-1, in the particle velocity direction and normal to that. To determine the acceleration components ($\ddot{x}$, $\ddot{y}$, $\ddot{\varphi}$) the cutting force is divided by the mass of a particle, as this is a per-particle based erosion simulation shown in Equation 4-6. Prior to that, the x, y and rotational components of the model are described in Equation 4-2 to 4-6. Originally, Hashish's formulation divided the jet stream into dx sections, with corresponding mass, dm. Then the waterjet stream is divided further such that each dx' was the forward step of one particle; a similar formulation was used in this model. In Figure 11, dh demonstrates the depth of penetration (d.o.p.) that each dx' (particle step) will penetrate into the work piece. To follow the particle position as it penetrates into the work piece, the dh is tracked by dividing the penetration into time steps, dts, to properly illustrate this erosion. A convergence study comparing erosion prediction with varying dts magnitude (10<dts<5000) showed $dts = 500$ is sufficiently accurate with incremental changes in depth prediction becoming negligible with $dts > 500$; the percentage change demonstrating the convergence can be found in Appendix C – Erosion Model Results.

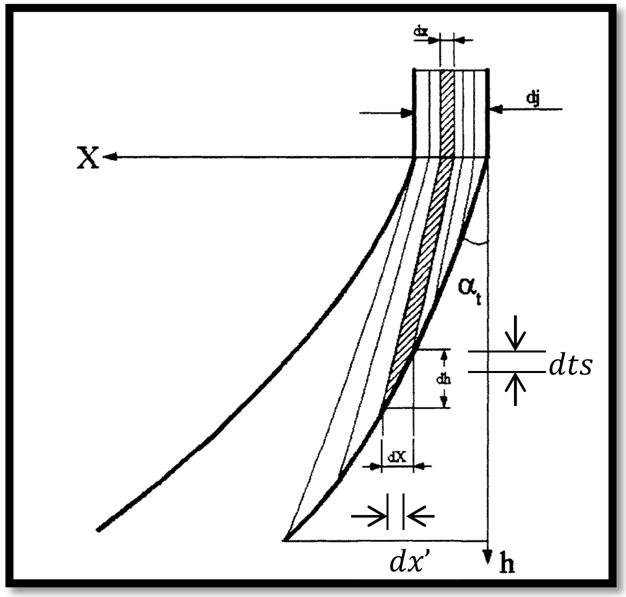

Figure 11 : New per-particle formulation

Utilizing the output information of the ANSYS Fluent model the initial velocity components of the abrasive are estimated. With the formulation shown in Equation 4-7 the updated velocity can be determined with the initial velocity, acceleration and time step dts. Further, with the work piece dimensions set, the initial particle position at impact is known such that the new position can be determined as the particle cuts through the work piece. Two criteria must be checked per immediate time step iteration, dts: first that the velocity in the vertical component is greater than zero for cutting to occur, and that the particle position remains in the work piece. Otherwise the particle has exited the side or bottom of the work piece and is no longer cutting. To simulate the particle-work piece interaction during the erosion process a square particle is used to represent the abrasive non-spherical particle; referring to Figure 12 the schematic of the square particle used in simulation is illustrated.

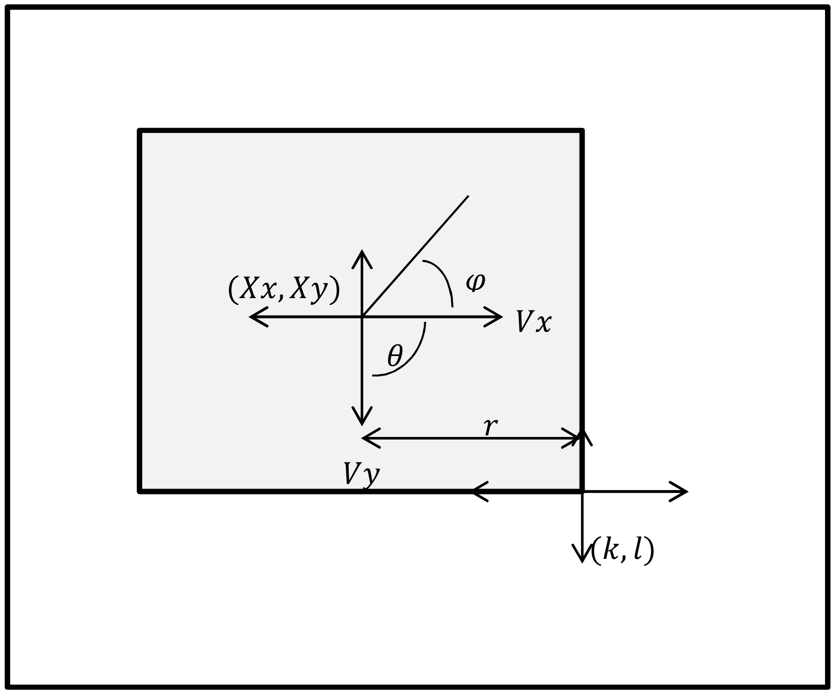

Figure 12: Simulated particle schematic

With $\theta = \arctan({}^{v_x}/_{v_y})$, $k = x + r\varphi$, $l = y + r\varphi$ and central difference algorithm (Equation 2-36) the single particle erosion can be solved. The d.o.c. equal to 't' in Equation 4-1 directly effects the resulting force at impact and thereby the deceleration of the abrasive particle throughout erosion. The initial velocity components V_x & V_y, are the mixing head/nozzle feed rate in the x-direction and the maximum of the abrasive particle velocity profile determined from the ANSYS CFD model. The initial position of the particle is determined with consideration of the size of work piece, which was set at twenty centimeters in height and ten centimeters in width. Therefore, the initial position of the center of the particle is 0.2m plus the radius of the particle in the y-direction. In the x-direction the left edge of the work piece was referenced zero, then less the radius of the particle to its center of gravity, plus the depth of cut, t, in the positive x-direction to engage the particle into the work piece. Theta (θ) is determined initially as the inverse tangent of the feed rate over the initial vertical velocity component of the abrasive particle. As the particle impacts the work piece the particle will rebound and begin to rotate phi (φ) radians. This rotation must be added to theta to update the angle of the particle upon impact as it continues to cut; the rotation of the particle is about its centre of gravity. To determine the particle tip position the rotation must be transformed to the leading edge to accurately determine and update the d.o.c. for the next iteration as it will change dependent on this rotation and original particle position.

The particle rotation during penetration can be seen below in Figure 13**.** As the particle penetrates into the work piece in stage i there is a depth of cut (d.o.c.) presented t_i. In stage ii outlined in blue, the particle begins to rotate as its momentum is resisted by the work piece thereby $t_{ii} < t_i$. The rotation of the particle continues to increase into stage iii outlined in red, in turn causing t_{iii} to be nearly negligible and the effective cutting terminates. The three stages illustrated simulate what is incrementally occurring over the dts stages; in some cases upwards of 500,000 steps were required for the total erosion depth to be simulated.

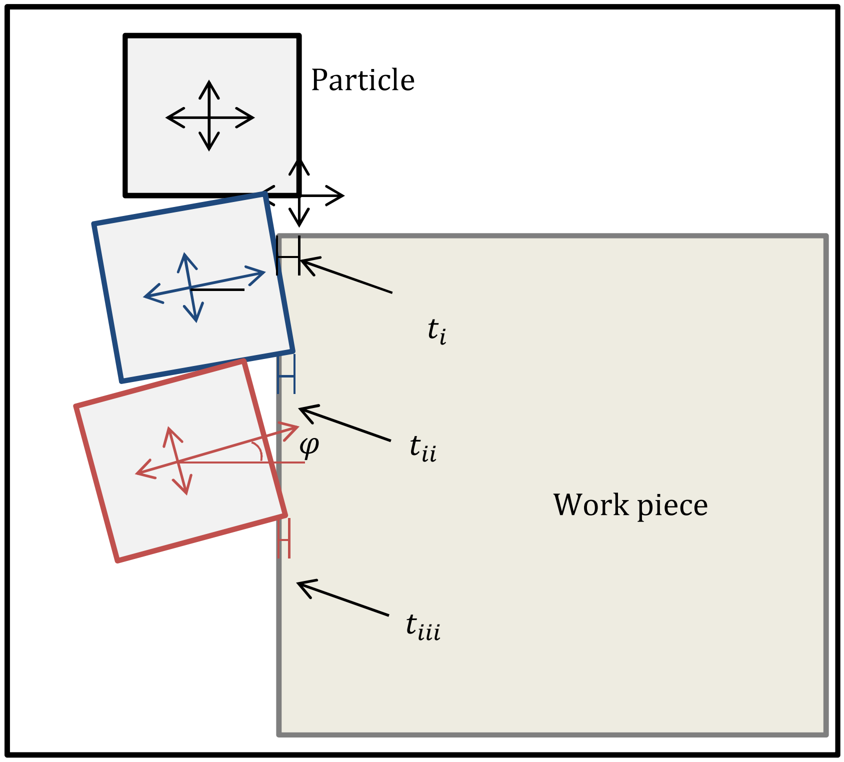

Figure 13: Erosion simulation

To determine the particle tip positions $delK$ and $delL$ are calculated as follows, per dts iteration.

$$cos\varphi = {}^{r}/_{hyp}\ , delK \approx hyp - r \quad \text{Equation 4-9}$$

$$delK = \left({}^{r}/_{hyp}\right) - \mathrm{r} \quad \text{Equation 4-10}$$

$$X_{xk} = Xx + r + delK \quad \text{Equation 4-11}$$

$$sin\varphi = {}^{opp}/_{hyp}\ , delL = opp \quad \text{Equation 4-12}$$

$$delL = \left({}^{r}/_{cos\varphi}\right) * \sin\varphi$$ Equation 4-13

$$X_{yL} = Xy - r - delL$$ Equation 4-14

The $delK$ is crucial to update the resultant cutting force in Equation 4-1 as $delk$ will decrease the depth of cut, t, directly effecting the cutting force. Using the radius of the particle and the rotation of the particle from original impact, φ, the hypotenuse can be determined. The decrease from the original depth of cut, t, is $delK$determined in Equation 4-10. Finally, the new x-position of the particle tip, named X_{xk}, can be determined in Equation 4-11. Using the same mentality and trigonometry relationships, the y-position of the tip can be determined as well, shown in Equation 4-12, 4-13 and 4-14. Now, the updated formulation for the resulting cutting force, with the loss in depth of cut due to particle rotation, is shown in Equation 4-15:

$$F_v = K_s b(t - delK)$$ Equation 4-15

Lastly, knowing the starting position of the particle, which would be the top of the work piece initially at the instant of impact, the d.o.p. can be determined as the absolute of the difference between Xyo and Xyi. The results of the erosion formulation will be discussed in chapter 6.

The final point of discussion is the formulation for the specific cutting energy relationship, Ks, below in Equation 4-19 and Equation 4-20. ElTobgy's initial work was compared against Hashish's model and experimental work done by Hashish (Hashish, Pressure effects in abrasive waterjet (AWJ) machining , 1989). The Ks formulation for

ASTM A36 Steel was a constant of magnitude 50 $J/_{mm^3}$ regardless that two feed rates and five pressures were simulated. In ElTobgy's erosion simulation the Ks constant determined from a FEM model assumed a magnitude of 40-50 times greater due to the restrictions of the FEM simulation; mainly the material contact interaction speed was limited to <10m/s whereas in water jetting the speed is >300m/s. When comparing ElTobgy's final simulation to experimental work on Ti-6Al-4V the specific cutting resistance showed an increasing trend with impacting velocity, different to the constant alluded to in the prior experiments, completed by a third party. Little elaboration on the significance of this increasing trend was described.

During the erosion, as the initial particle strikes a surface it will cause plastic deformation, potentially causing no material removal, by this means, strain hardening the surface which is common in shot peening applications. Upon repeated impact of the surface the strain-hardened/plastically deformed zone material will be removed. As the particle velocity increases with pump pressure the material will harden more significantly due to higher strain rates, hence the relationship of increasing Ks with increasing particle velocity. However, this does not appear to be a linear relationship as determined by ElTobgy's FE model. Further, the assumptions that no secondary cutting occurs is inaccurate, especially as feed rate decreases which allows for more particles impact to be localised to an area, re-entrain in the fluid and erode the work piece again; this common trend is observed experimentally - and shown in Table 1: AWJ parameters - as feed rate decreases d.o.p. increases. After the initial particle impact the abrasive can reaccelerate to sufficient speed entrained in jet flow and cause secondary cutting; this is more likely to occur as the feed rate, u, decreases. To account for these to relationships observed in experiments Equation 4-19 and Equation 4-20 were developed by fitting constants to tests of one mass flow rate, three feed rates and five pressures. The model was then compared to Hashish's model and experiments at this mass flow rate, plus three additional, four feed rates and nine pressures, totalling sixty-five different cases; the results will be discussed in section 6.3.

To determine the constants for the Ks formulation a GRG non-linear solver in Excel was used. A generalized reduced gradient (GRG) solver utilizes the smoothness of a function by computing gradient values at various trial solutions and moving in the negative gradient direction when optimizing for a minimal value; vice versa when optimizing for a maximum value (FrontlineSolvers, 2012). The function must be continuous – no breaks in graph – and smooth – not 'V' shaped where the derivative is discontinuous. Lastly, a non-convex function may have multiple locally optimal solutions, but determining the global solution may take time or be unfeasible if objective function is unbounded.

The determination of the Ks formulation was an iterative process. Initially, with 5 pressures, 3 feed rates, and 1 mass flow rate there were 15 cases to be predicted and compared to experimentally. The specific cutting energy formulation initially included a constant, plus a second constant multiplied by the input velocity of the abrasive particle.

$$Ks = C_1 + C_2\, V \qquad \text{Equation 4-16}$$

After the d.o.p. prediction was determined for the first fifteen original cases the values were compared to the experiments and a more appropriate Ks was re-estimated.

Recalling, $F = K_s bt$, if Ks is too large the erosion will be under predicted because the deceleration will become larger. Vice versa, if the Ks estimation is too small the deceleration of the abrasive particle will not be immediate enough and the erosion will be overestimated in comparison to d.o.p. observed in the experiments. Therefore, the Ks values were iteratively re-estimated to calibrate the formulation. The error between the previously calculated and the recently re-estimated Ks values was determined and the absolute error of the 15 cases was summed and set as the objective cell. Similarly, the d.o.p. was compared to the experiments and the relative error was utilized to estimate the degree to which the Ks formulation was incorrect. The variable cells included the constants in the formulation of the Ks and the objective cell was set to be minimized. Other cell constraints were set to localize the solution to assist in convergence; for example $0 < Ks < 1E11$. Following convergence the d.o.p. was recalculated and the process was repeated.

The Ks formulation then expanded to include non-linear terms for velocity and feed rate. The updated formulation included seven constants up to a third power.

$$Ks = C_1 + C_2\,V + C_3 V^2 + C_4\,V^3 + C_5\,u + C_6 u^2 + C_7\,u^3 \qquad \text{Equation 4-17}$$

The GRG non-linear solver was used to determine these values, however a final realization was the power was not necessarily an integer. As such, the formulation for the solvers final form, including eleven constants, was:

$$Ks = C_1 + C_2\,V + C_3 V^{C_8} + C_4\,V^{C_9} + C_5\,u + C_6 u^{C_{10}} + C_7\,u^{C_{11}} \qquad \text{Equation 4-18}$$

Based on Equation 4-18 the GRG non-linear solver led to the final two relationships for the specific cutting energy:

$$Ks = 10.239E10 + 4.030E8\,V + 3.905E5\,V\text{^}2 + 9.513E12\,u\text{^}1.368 \quad , for\ 3\ mm\ /\ s < u < 8\ mm\ /\ s \qquad \text{Equation 4-19}$$

$$Ks = 51.471E9 + 2.247E8\,V + 2.333E5\,V\text{^}2 + 5.600E11\,u \quad , for\ 8\ mm\ /\ s < u < 50\ mm\ /\ s \qquad \text{Equation 4-20}$$

This Ks relationship was then used to estimate the d.o.p. in a parametric study over four mass flow rates, nine pressures, and seven feed rates totalling sixty-five cases; the accuracy improvements in depth of penetration prediction versus experiments will be discussed in section 6.3.

5 CFD

5.1 CFD Test Metrics

The computational fluid model methodology has been previously described. The CFD analysis was developed to understand the effect of variance in nozzle input parameters including: particle size, shape, mass flow rate of abrasive, focus tube length, input pressure and lastly volume fraction of air in the fluid mixture. Parameters were chosen based on common industry setups and settings chosen in other literature for further comparison and validation. The particle size was modelled between 0.0059" to 0.028", a difference of almost five times in magnitude. The shape factor, described earlier as a comparison in unity to a sphere, changed from 0.4 to unity at 1.0. The mass flow rate modelled between 5 to 25g/s. Focus tube length modelled 2, 4 and 6 inches (5.08cm, 10.16cm, 15.24cm) and pressure investigated from 150 to 350 MPa over 5 intervals. Lastly, the volume fraction of air in the fluid mixture started with zero percent air up to a maximum of 95% to further the understanding of air in the jet-stream mixture.

A base case of parameters were held, while only one of the six parameters was altered at a time. The base case includes a particle size of mesh 40, equivalent to 0.0165" (0.4191cm), shape factor of 0.8, a mass flow rate of 10 g/s, focus tube length of 4" (10.16cm), pressure is 300 MPa, and volume fraction of air of 95%. The various test cases are presented in Table 3: CFD test metrics.

Model Characteristics	P.S	P.Sh.	MFR	FTL	P	V.O.Air
	40	0.8	0.01	4	300	95%
Particle Size (P.S.) (mesh)	25=0.0280''	0.8	0.01	4	300	95%
	40=0.0165''	0.8	0.01	4	300	95%
	60=0.0098''	0.8	0.01	4	300	95%
	100=0.0059''	0.8	0.01	4	300	95%
Particle Shape (P.Sh.)	40	0.4	0.01	4	300	95%
	40	0.6	0.01	4	300	95%
	40	**0.8**	0.01	4	300	95%
	40	1	0.01	4	300	95%
Mass flow rate (MFR) (Kg/s)	40	0.8	0.005	4	300	95%
	40	0.8	**0.01**	4	300	95%
	40	0.8	0.015	4	300	95%
	40	0.8	0.02	4	300	95%
	40	0.8	0.025	4	300	95%
Focus tube length (F.T.L.)	40	0.8	0.01	2	300	95%
	40	0.8	0.01	**4**	300	95%
	40	0.8	0.01	6	300	95%
Pressure (P) (MPa)	40	0.8	0.01	4	150	95%
	40	0.8	0.01	4	200	95%
	40	0.8	0.01	4	250	95%
	40	0.8	0.01	4	**300**	95%
	40	0.8	0.01	4	350	95%
V.O.Air (%)	40	0.8	0.01	4	300	0
	40	0.8	0.01	4	300	25
	40	0.8	0.01	4	300	50
	40	0.8	0.01	4	300	75
	40	0.8	0.01	4	300	**95**

Table 3: CFD test metrics

5.2 Model Results

The motivation of the model is to continue the understanding of the inner workings of the AWJ nozzle; to understand the mechanisms of the mixing process, including the affect certain input parameters have on the output of the waterjet profile. More specifically, the research is to obtain a velocity profile for the discrete phase material at a particular standoff distance, to then use with the updated erosion model. A 25-feed streamline is shown in Figure 14 together with a vector plot of the DMP shown Figure 15. The water converges into the orifice where it spikes upon exiting into the mixing head; this is how the large potential energy, from the pressure developed by the intensifier pump, is converted to high speed kinetic energy. Abrasive garnet enters through the mass inlet shown and the water and garnet mix. The garnet particles are accelerated due a difference in momentum between the phases, as energy from the water is transferred to the garnet. Finally, exit to atmosphere causes an abrupt deceleration in the water as it starts to loose coherence and diverge radially.

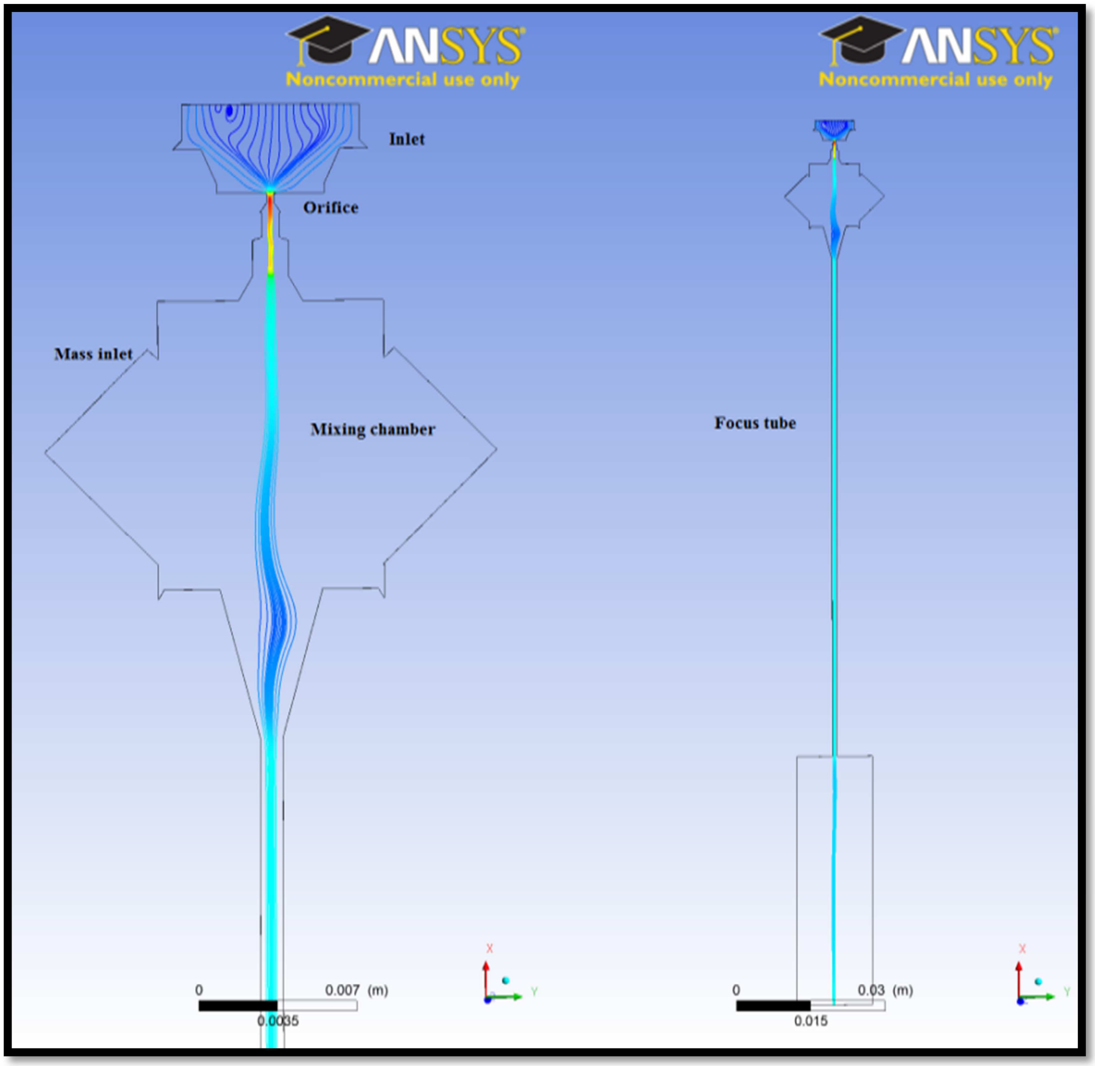

Figure 14: Water Streamline

As described earlier, the large pressure difference between the high speed water velocity into the mixing head and the low speed garnet causes the garnet to be pulled into the mixing chamber where it is entrained in the water flow via the Venturi phenomenon; a vector plot illustrating this mixture is shown in Figure 15.

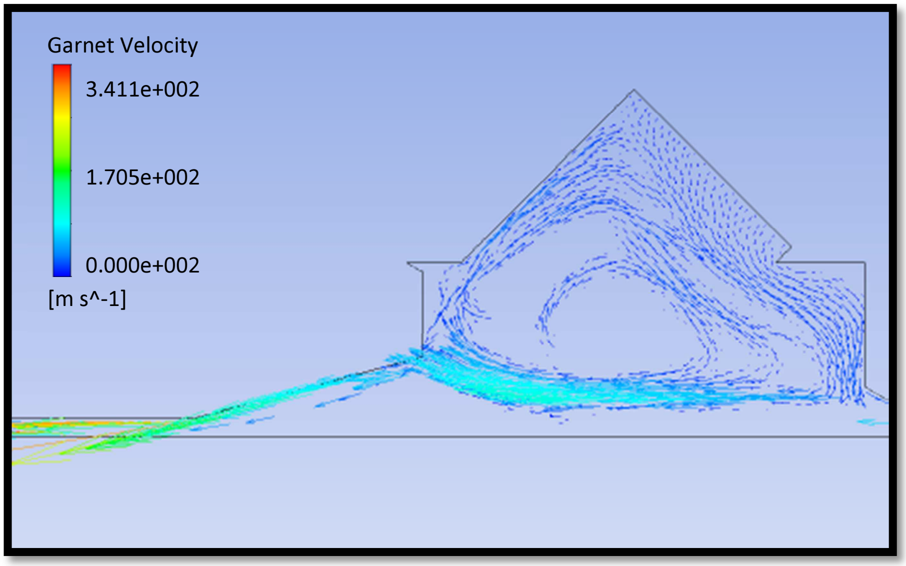

Figure 15: DPM Vector Plot

The input parameters that were modeled include input pressure, material flow rate focus tube length, particle size and shape and most crucial was the investigation of the volume fraction percentage of air. The volume fraction refers to the volume of fluid occupied by a particular phase, or combination of phases, but can never be void.

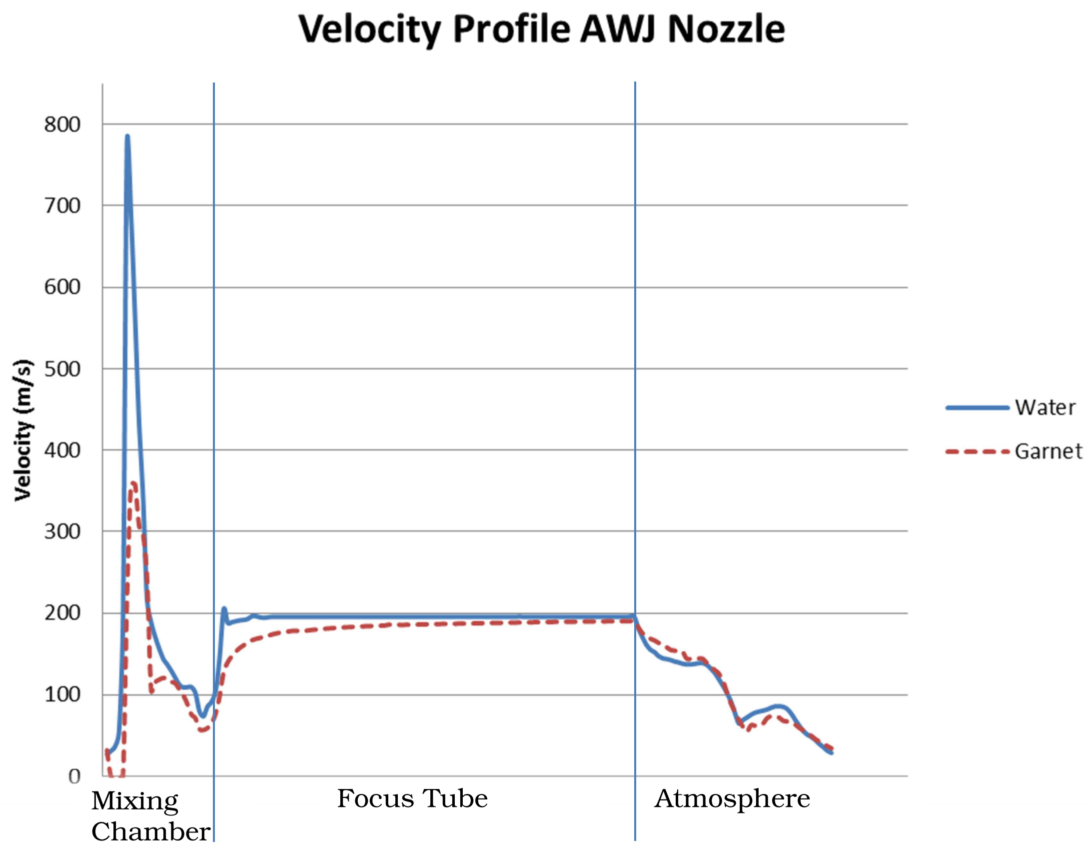

Figure 16: Velocity Profile AWJ Nozzle

The theoretical velocity of the flow can be estimated by simplifying Bernoulli's law and computing the pressure balance which makes:

$$V_{th} = \sqrt{\frac{2P}{\rho}} \qquad \text{Equation 5-1}$$

Using Equation 5-1, the theoretical velocity of the water should be 775m/s, assuming no losses; generally an efficiency term is added to account for such loses. This velocity is dependent on pressure and density. However, work previously described by Tazbit et al.

(1996) concluded the volume fraction of air to be about 95%. The density of the Eulerian mixture modeled is calculated by:

$$\rho_{12} = \propto \cdot \rho_1 + (1 - \propto) \cdot \rho_2$$

Equation 5-2

In turn, the volume fraction of air (v.o.f) significantly changes the overall density of the Eulerian mixture modeled and the inlet velocity is significantly affected. The effect of the volume fraction of air is shown in Figure 17. Neglecting the v.o.f. significantly underestimates the inlet velocity of the water. When v.o.f. is 95% air and 4% water the inlet velocity through the orifice is about 1600m/s compared to <800m/s when air is not accounted for in the mixture. More advantages with the consideration of the air within the fluid is the promotion of turbulence, facilitating mixture and entrainment in the mixing head. Lastly, although the density of the mixture is reduced - and the energy transfer to the garnet is driven by the momentum transfer from the water-air mixture - the mass flow rate of the fluid is significantly high such that the garnet is accelerated sufficiently based on this increase in velocity, regardless that the density of the fluid mixture is decreased. Therefore, effective material removal of the work piece continues.

Particle size, shape and mass flow rate inputs were varied individually –all else the same - to determine their effect on the garnite oulet velocity. The particle size and mass flow rate had negligible effect on the final garnet velocity; a 4.1% difference in velocity magnitude over the range of particle sizes modelled and a 0.6% difference in velocity magnitude change over the mass flow rates investigated. The outlet velocities are compared at a reference stand-off distance (s.o.d.) of 1mm in Table 4. Due to the large difference in mass flow rate between the water-air fluid and the garnet, the size and flow-rate did not inhibit the acceleration during the mixing process through the nozzle for the cases tested. Not to be confused, the particle size, shape and mass flow rate of abrasive will directly effect the material removal rate. The CFD model is describing that the fluid mixture is sufficiently dominant such that the momenteum exchange has minimal effect on the fluid mixture output and the velocity output remains high.

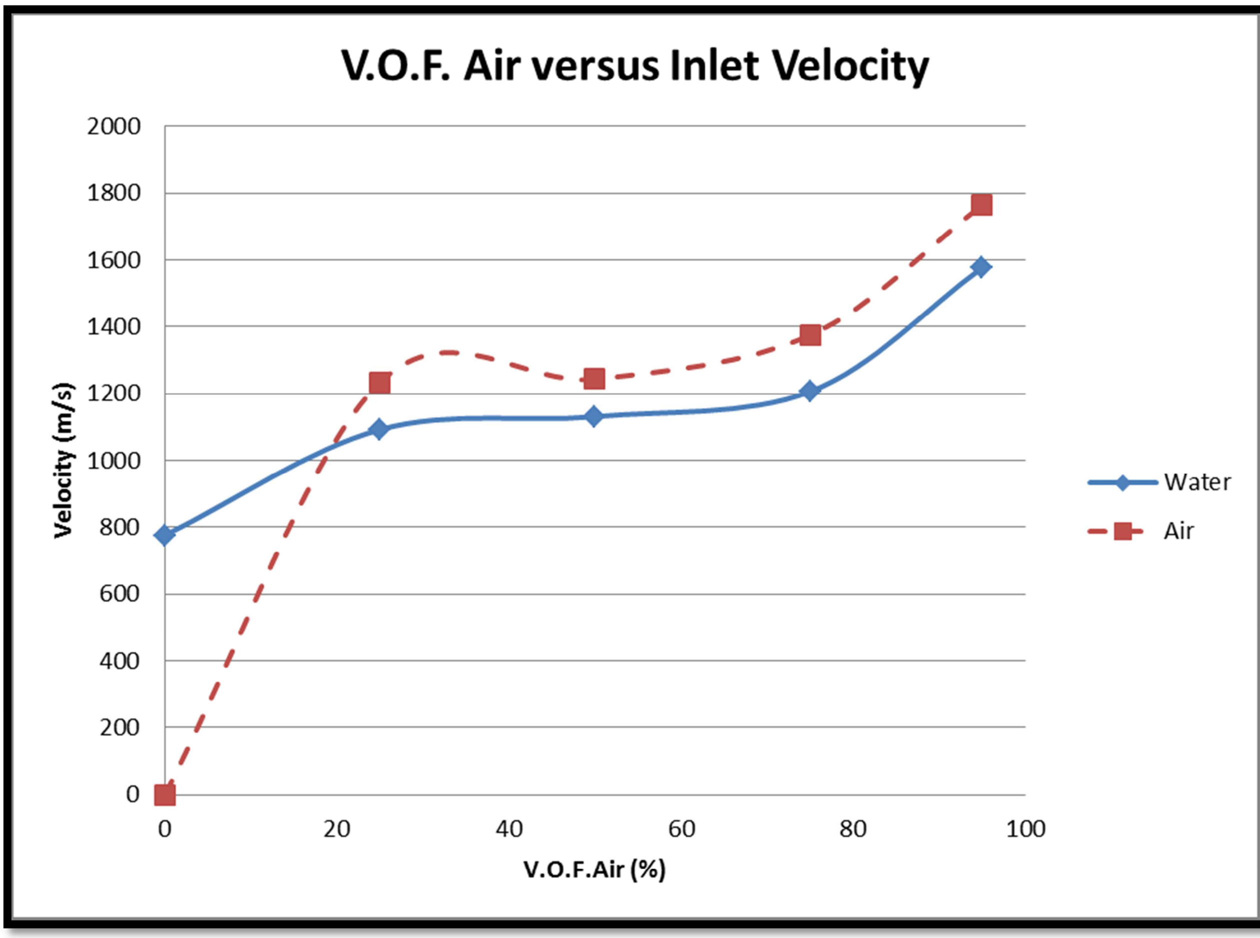

Figure 17: v.o.f. Air versus Inlet Velocity

Particle Size (mesh)	Garnet Max Velocity (m/s)	Mass flow rate (kg/s)	Garnet Max Velocity (m/s)
25=0.028”=0.071cm	**388.11**	0.005	**401.07**
40=0.0165”=0.042cm	**398.56**	0.01	**398.56**
60=0.0098”=0.025cm	**404.61**	0.015	**400.35**
100=0.0059”=0.015cm	**402.62**	0.02	**399.46**
		0.025	**399.58**

Table 4: Particle size and MFR on modeled garnet velocity

The shape factor had a significant effect on the output velocity. Figure 19 clearly demonstrates, as the shape factor approaches unity, the final velocity of the garnet decreases by as much as 10 percent. Unity refers to a particles geometry that is perfectly spherical. Shape factor is a value between 0 to 1, 1 being unity. The smaller the shape factor, ($\Phi \approx 0.3$), the more jagged the particle becomes. The jagged, flat surfaces increase the mixing capabilities of the garnet, rather than the streamline effect occurring with a perfectly spherical particle. This promotes the acceleration of the particle within the fluid; a shape factor of 0.8 is most similar to the garnet used in experiments. Illustrations of sphericity and roundness determining the shape factor are illustrated in Figure 18.

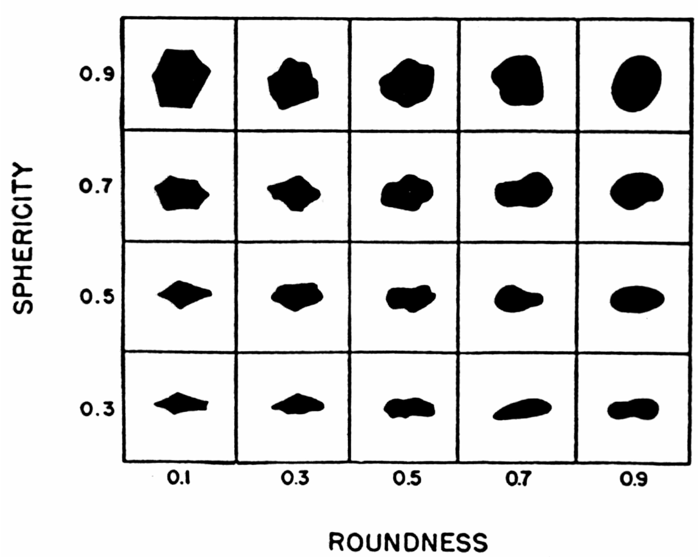

Figure 18: Shape factor diagram (Folk, 1955)

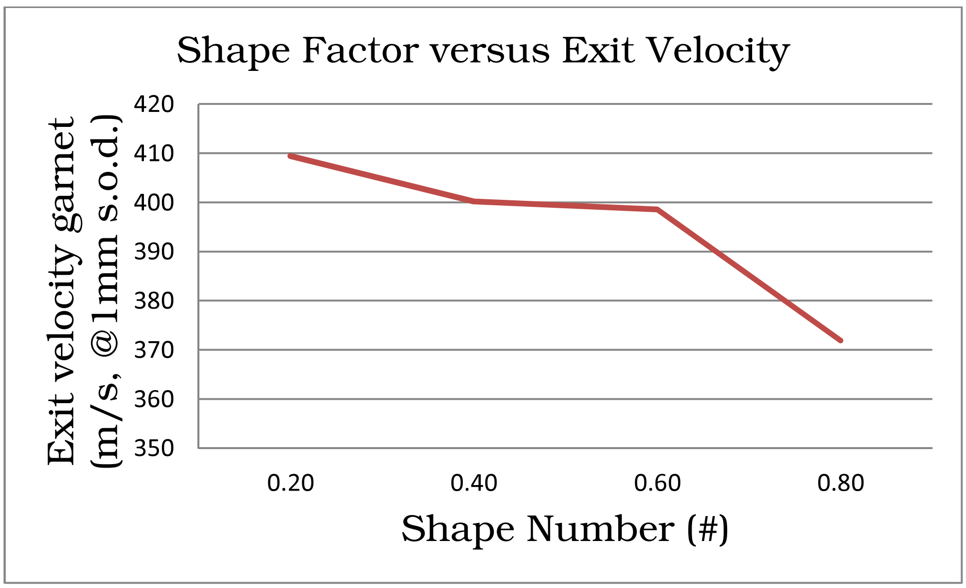

Figure 19: Particle shape effect

The focus tube was modeled at 2”, 4” and 6” (5.08cm, 10.16cm, 15.24cm) in length. Tazbit et al. (1996) describe how the inclusion of air drastically increases the focus tube length required for the discrete phase to reach equilibrium with the fluid; garnet initially near standstill is accelerated fully to match the speed of the fluid mixture. This distance increased from 12cm with zero air, to 12m with 95% air. Figure 20 below coincides with that work illustrating a 20% increase in exit velocity with the extension of 4 inches (10.16cm). Further modeling to investigate the theory of an ideal focus tube length for a set of input parameters - be it pressure, particle size, shape, flow-rate etc. – should be completed for potential development of an adjustable length nozzle.

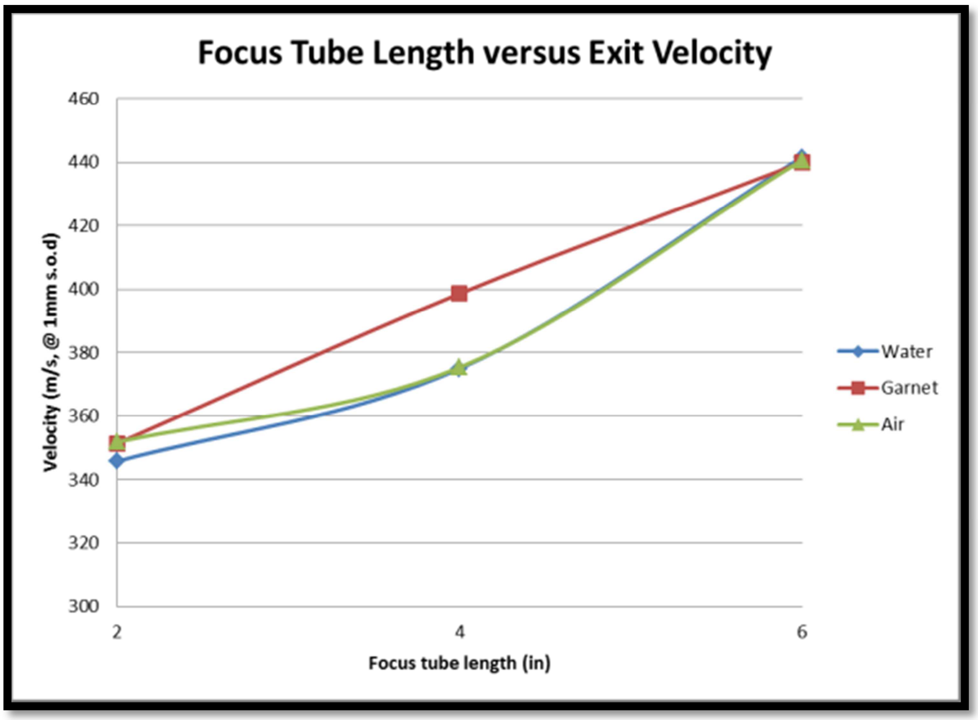

Figure 20: Focus tube length effect

Most significant, is the determination of the garnet velocity profile per stand-off distance that can be utilized in the updated erosion model shown in Figure 21. This is a 2D render, however because the nozzle is symetrical it can be rotated 2π about the center to create a 3D abrasive velocity profile. Liu et al. (2004) described a "top-hat" profile for the jet flow; a concentration of velocities in the center decreasing in magnitude radially away

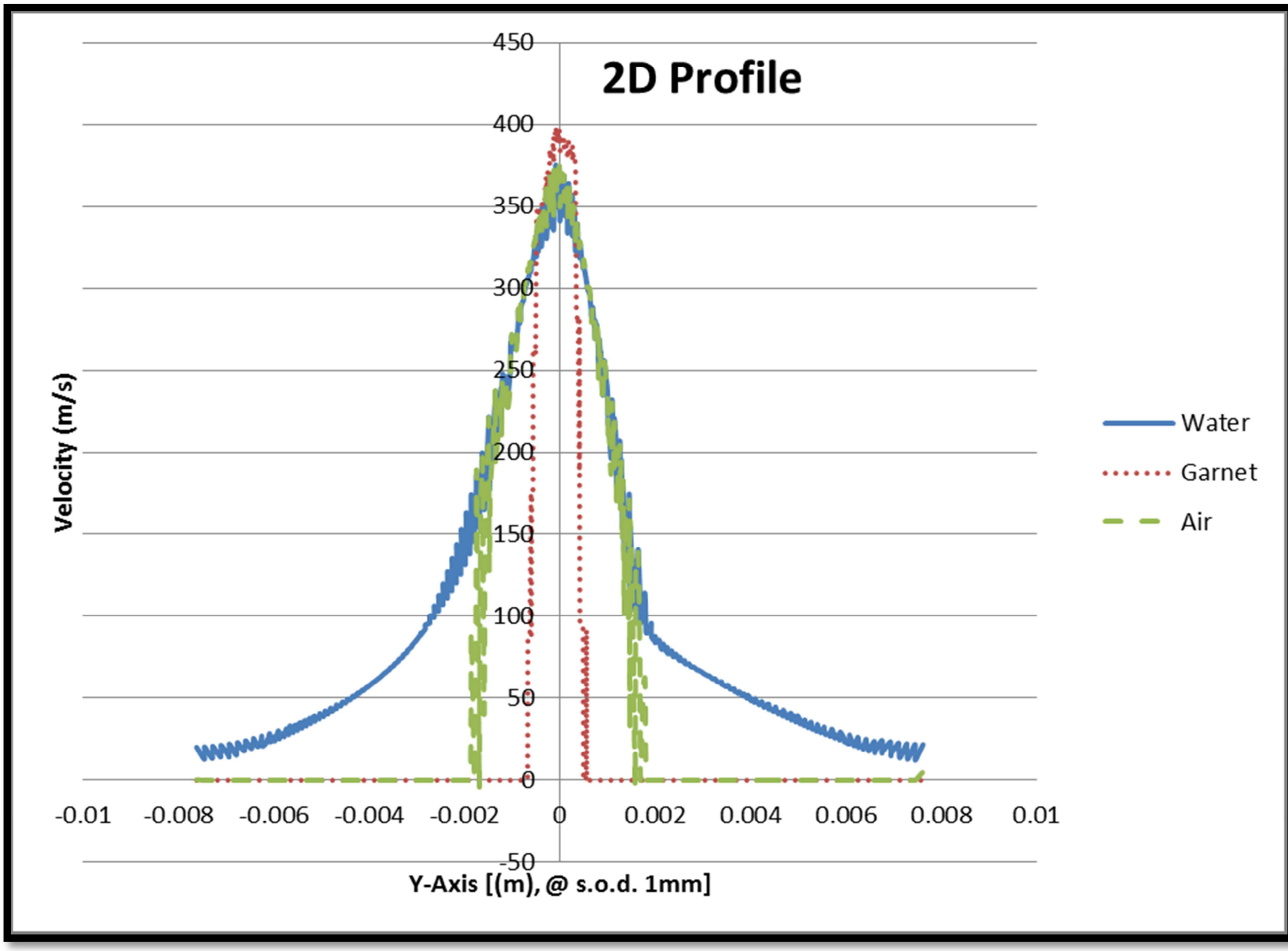

Figure 21: 2D Garnet velocity profile

from the center. The results from the CFD model confirm this, correlating to the kerf formation in the work piece observed when cutting. Because the velocity in the center is the greatest, the greatest penetration is also achieved in the center, tapering out to the sides where the velocity of the abrasive is lower.

This information is extremely useful as a correction to the modified erosion numerical model, developed by ElTobgy, which assumes a constant velocity over the jet diameter; not the case in actual jet. The additional information on the profile used in the erosion model could prove more accurate in predicting depth of cut by building on the per particle model setup. Rather than simulating one particle eroding one depth of cut and repeating, a wave of particles with varying velocities based on the 2D particle velocity profile can be calculated and individual erosions summed to generate the penetration depth prediction. This revised methodology will be discussed further in Future Work but is illustrated below.

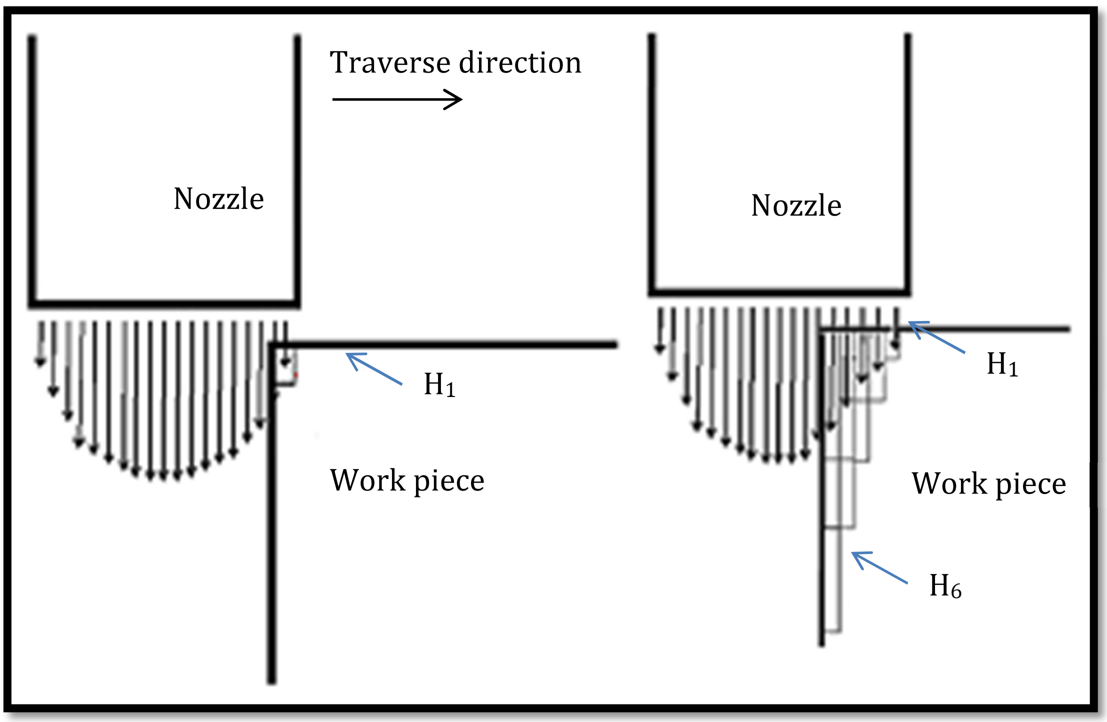

Figure 22: “top-hat” erosion methodology

Initially as the nozzle approaches the work piece the first abrasive stream from the jet is the only particle that impacts the work piece to a depth of H_1 shown in Figure 22. As the nozzle traverses across the work piece more abrasive particles can co-penetrate the work piece each with their own depth of cut. For example, H_6 is in the same x-position in the work piece as H_1 was originally, however it took six dx stages for this erosion to take place, to the depth of H_6. Each individual penetration depth will still be modelled at individual stages, dts, as described in the current updated erosion model to ensure particle deceleration, velocities and most importantly positions are accurately known. Once all particles co-penetrating cease eroding the work piece the nozzle will traverse dx and the next stage in the erosion will occur. Summing all of the individual penetration depths will determine the aggregate penetration depth for the simulation; however more accurate surface modelling will be created including determination of the stream lag. Moreover, there is less reliance on efficiency terms because with this methodology the effective erosion by a particle is based on its initial velocity of that stream. This is more accurately represented with the 2D profile generated by the CFD, rather than an assumed constant equal to the maximum of the abrasive velocity profile.

6 Results of Erosion Model

6.1 Experimental Test Metrics

Experiments were completed using the Paser 3, 5-axis waterjet made by Flow. The work piece material was Ti-6Al-4V. The cutting parameters that were varied are listed in Table 5: Experimental test metrics, creating 61 different cases used to validate the empirical erosion simulation:

Stage I	Feed (mm/s)	3.4, 5.1, 7.6
(Experiments completed at McMaster)	Pressure (MPa)	172, 207, 241, 276, 310
	Mass flow rate (g/s)	2.86, 4.65, 10.31
Stage II	Feed (mm/s)	6.25, 12.5, 25, 50
(Experiments from literature)	Pressure (MPa)	150, 200, 250, 300
	Mass flow rate (g/s)	4

Table 5: Experimental test metrics

For each cut setting, three passes across the work piece were made (coded in an "s" pattern) providing three depths of cut; the depths were measured and averaged. The work piece was a 2x2x10 inch (5.08x5.08x25.4cm) bar. To ensure that jet entry or exit did not affect the depth measurement a ¼ inch (0.635cm) cross-section in the centre of the bar was cut out of the 2 inch thick work piece. The work piece was measured on a surface table using a depth gauge accurate to 0.001 inch (0.00254cm).

6.2 Experimental Work

Initial tests were carried out using the Paser 3, 5-axis waterjet made by Flow Corp. illustrated in Figure 23. Initial cuts were into a piece of 1045 steel at varying standoff distances (s.o.d.) and pressures to demonstrate and familiarize the effects of certain parameters on cut quality; mainly fogging, kerf width, cone or taper and stream lag. The results after changing the s.o.d. from 1/8" to 9/8" (0.3175-2.8575cm) and pressure from 200MPa to 350MPa were shown earlier in Figure 3: Cutting Limitations (i,ii,iii,iv) and agree with the trends demonstrated in Table 1: AWJ parameters as different cutting parameters are changed.

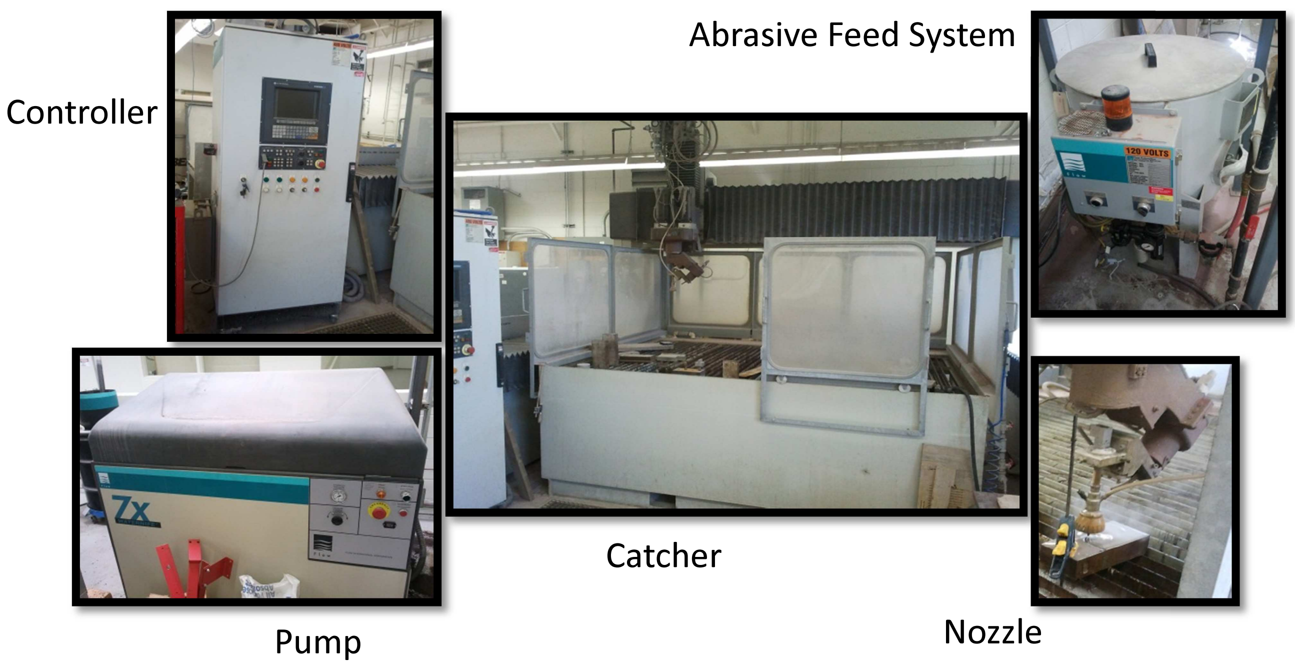

Figure 23: Experimental equipment

The CFD model compared the effects of numerous cutting parameters described in the modelling chapter previous. The velocity profiles determined in ANSYS Fluent - one case shown in Figure 21 - were used as input information for the d.o.p. erosion model. To validate this multi-physics model experiments were completed on a titanium alloy work piece, Ti-6Al-4V, at varying pressures, mass flow rates and feed rates. The test metrics were determined initially based on ElTobgy's previous work such that the updated erosion model could be compared to recent experiments, Hashish's model and ElTobgy's model in addition to experiments.

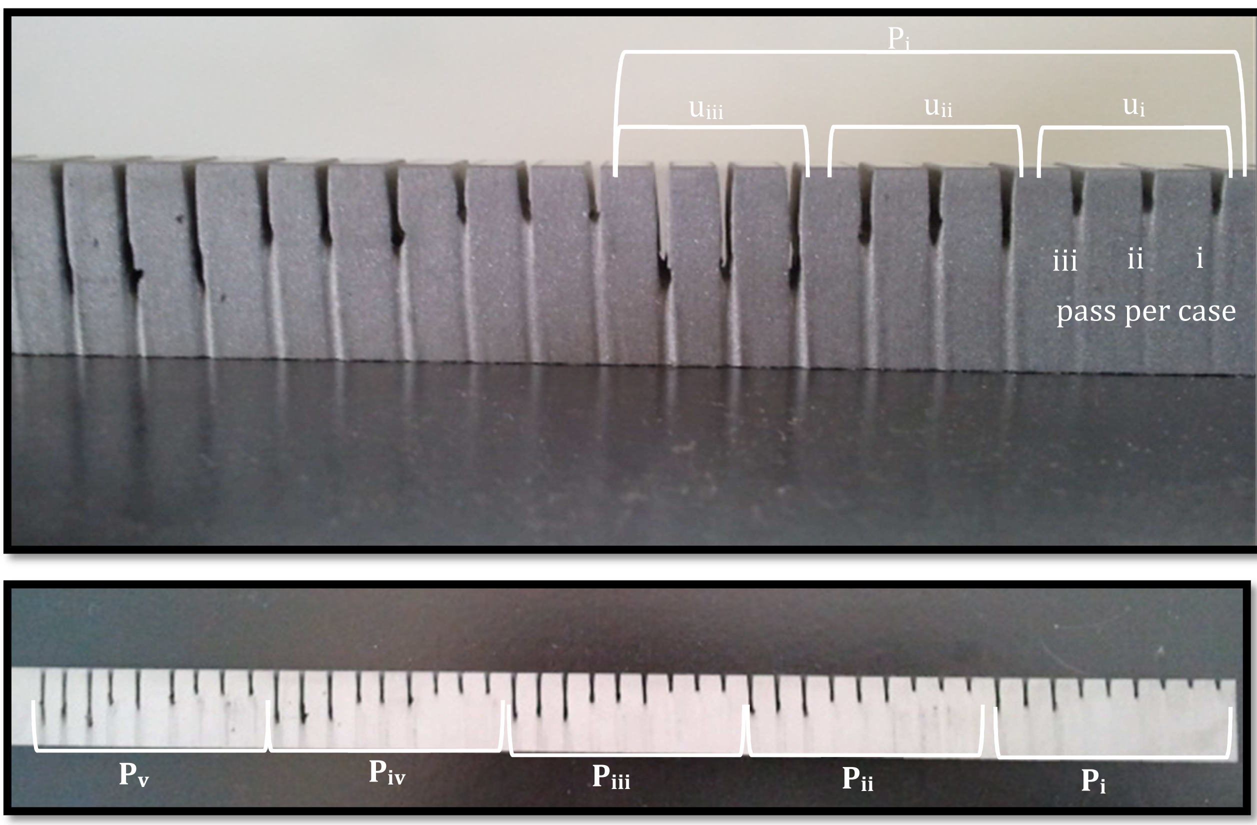

Figure 24: Experiments cross-section of Ti-6Al-4V

This included five pressures, three feed rates and three mass flow rates totaling 45 experimental cases for model comparison; tabulated results found in Appendix B – Experimental Results Table 8: Experimental results – 3MFR, 5 Pressures, 3 Feeds.

For each of the 45 setups the titanium work piece was cut three times, with linear horizontal passes, all parameters held the same. The depth of penetration for each case was then measured using a micro depth gauge and averaged. Sample cross section is illustrated in Figure 24. The three feed rates, u, five pressures, P, are outlined for one of the three mass flow rates, $\dot{m}$.

Figure 25: Experimental feed rate on d.o.p. shows the effect feed rate has on the d.o.p. in the work piece. As expected, when pump pressure increases more kinetic energy is developed, transferred to the abrasive and utilized in the penetration of the work piece.

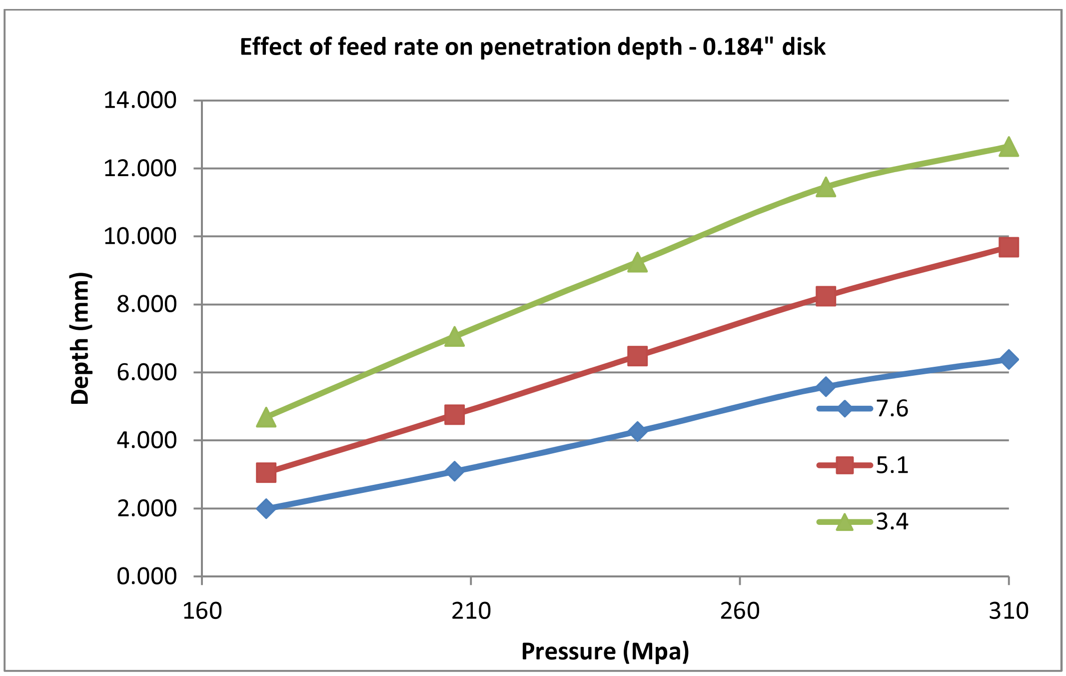

Figure 25: Experimental feed rate on d.o.p.

As the feed rate decreases - mass flow rate the same - more abrasive particles are able to repeatedly strike the localized surface contributing to a greater d.o.p. shown in

Figure 25.

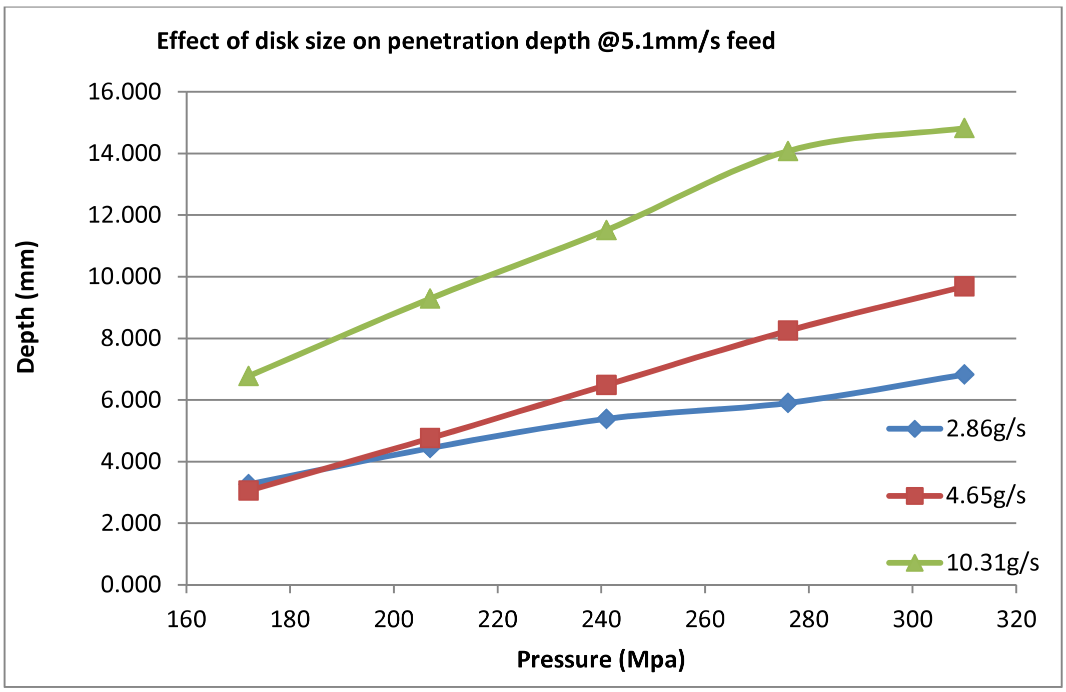

Figure 26: Experimental mass flow rate on d.o.p.

Figure 26 demonstrates, while feed rate is fixed an increase in disk size, which controls the mass-flow rate of the abrasive, increases the d.o.p. for the same reason described before; being that multiple particles can impact a localized area of the work piece and penetrate further. The experiments agree with literature tabulated in Table 1.

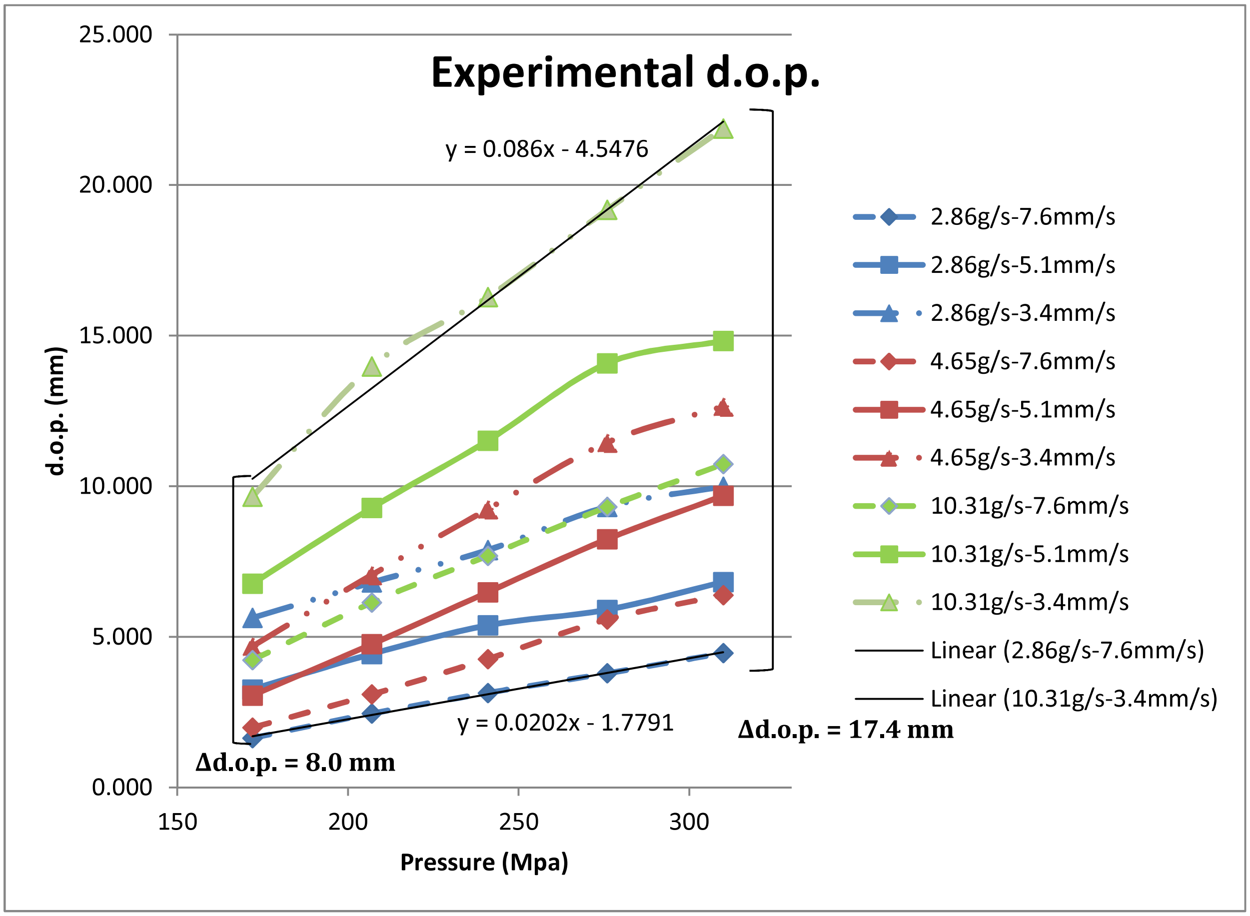

Figure 27: Experimental d.o.p. results

Figure 27 illustrates experimental results on the effects of mass flow rate and feed rate on d.o.p. The 3 mass flow rates are designated by color; blue-2.86g/s, red-4.65g/s, and green-10.31g/s. Further, the feed rates are designated in three categories: 7.6mm/s-diamond, 5.1mm/s-square and 3.4mm/s-triangle. The first aspect to note is the rate at which the d.o.p. increases, represented by slope, from y=0.02x to y=0.086x - between the 2.86g/s-7.6mm/s and 10.31g/s-3.4mm/s cases (the top and bottom lines illustrated). As the mass flow rate increases from 2.86g/s to 10.31g/s the percentage difference in d.o.p., between the initial pressures of 172MPa to the final pressure of 310MPa, increases 9.4mm.

Overall, as the larger mass flow rate is utilized by a higher pressure it is experiencing a more efficient material removal rate demonstrated by the increased slope or range in d.o.p. described.

6.3 Erosion model results

The erosion model with the Ks formulation described earlier was calibrated to the experimental data of three feed rates, five pressures and one mass flow rate. A parametric study was then carried out comparing the depth of penetration prediction over the same feed rates and pressures, but changing the mass flow rate from 4.65g/s to 2.86g/s and 10.31g/s to understand the models prediction capabilities as the mass flow rate of abrasive changes.

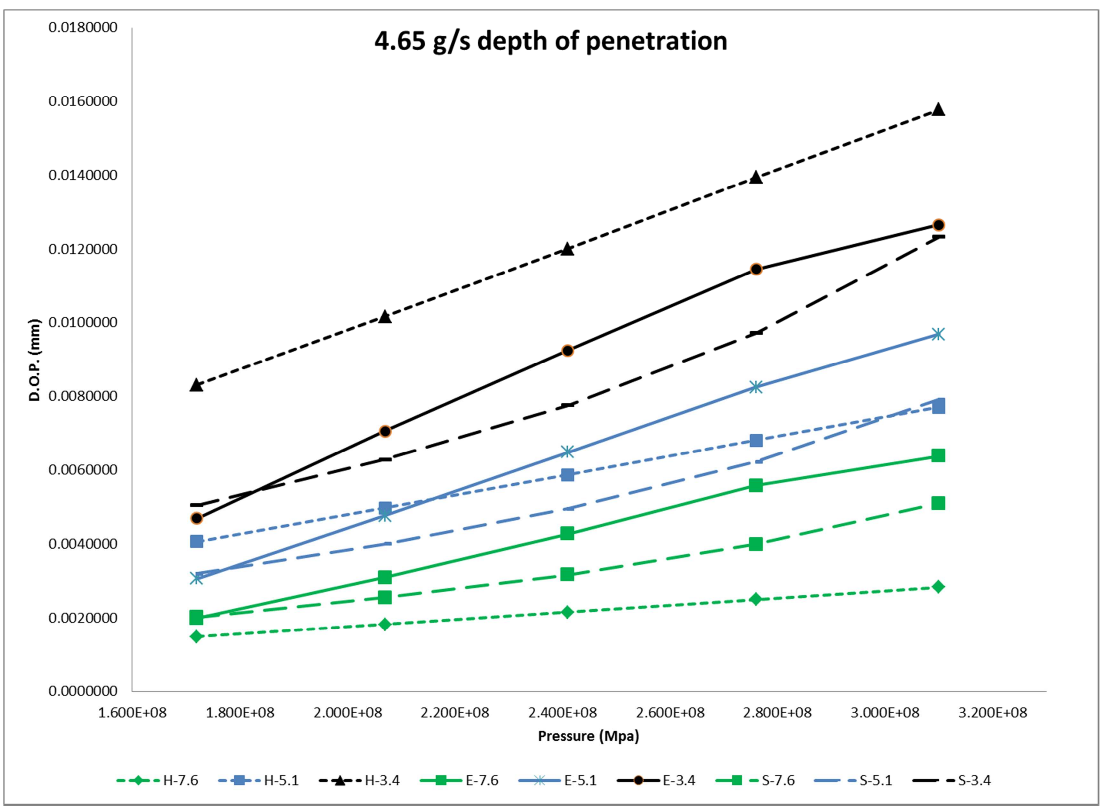

Figure 28: D.O.P. @ 4.65g/s New model (S) vs. Experiment (E) vs. Hashish (H)

This prediction was compared to experimental depth of penetration and tested against Hashish's model for a reference in error comparison. In Figure 28 the d.o.p. prediction is illustrated against the experimental results and Hashish`s model. Using these parameters Hashish`s model averaged 33.9% error versus a reduced average error of 14.1% with the new Ks formulation model; an error reduction of 58.5%. The better results directly relating to the new Ks formulation, rather that assuming a constant. When the new Ks model was tested at the different mass flow rates the error reduction was substantial. With a mass flow rate of 2.86g/s Hashish's error was 30.6% and the new Ks model was 13.5%; an overall error reduction of 55.9%; shown in Figure 29: D.O.P. @ 2.86g/s New model (S) vs. Experiment (E) vs. Hashish (H).

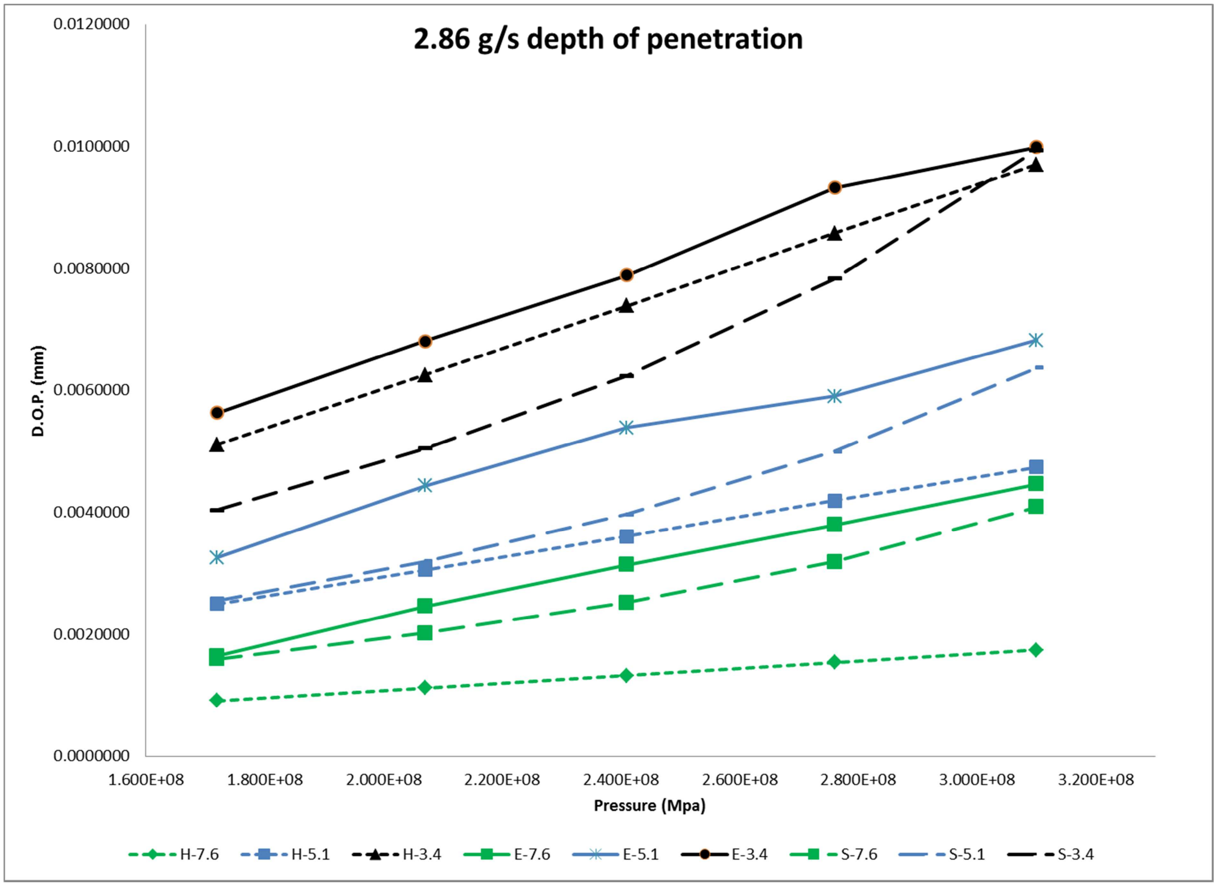

Figure 29: D.O.P. @ 2.86g/s New model (S) vs. Experiment (E) vs. Hashish (H)

Lastly, illustrated in Figure 30 at an extreme mass flow rate of 10.31g/s, to test the bounds of the model, Hashish's model had an average error of 40.0% and the new Ks formulation had an average error of 25.7%; a total error reduction of 35.7%.

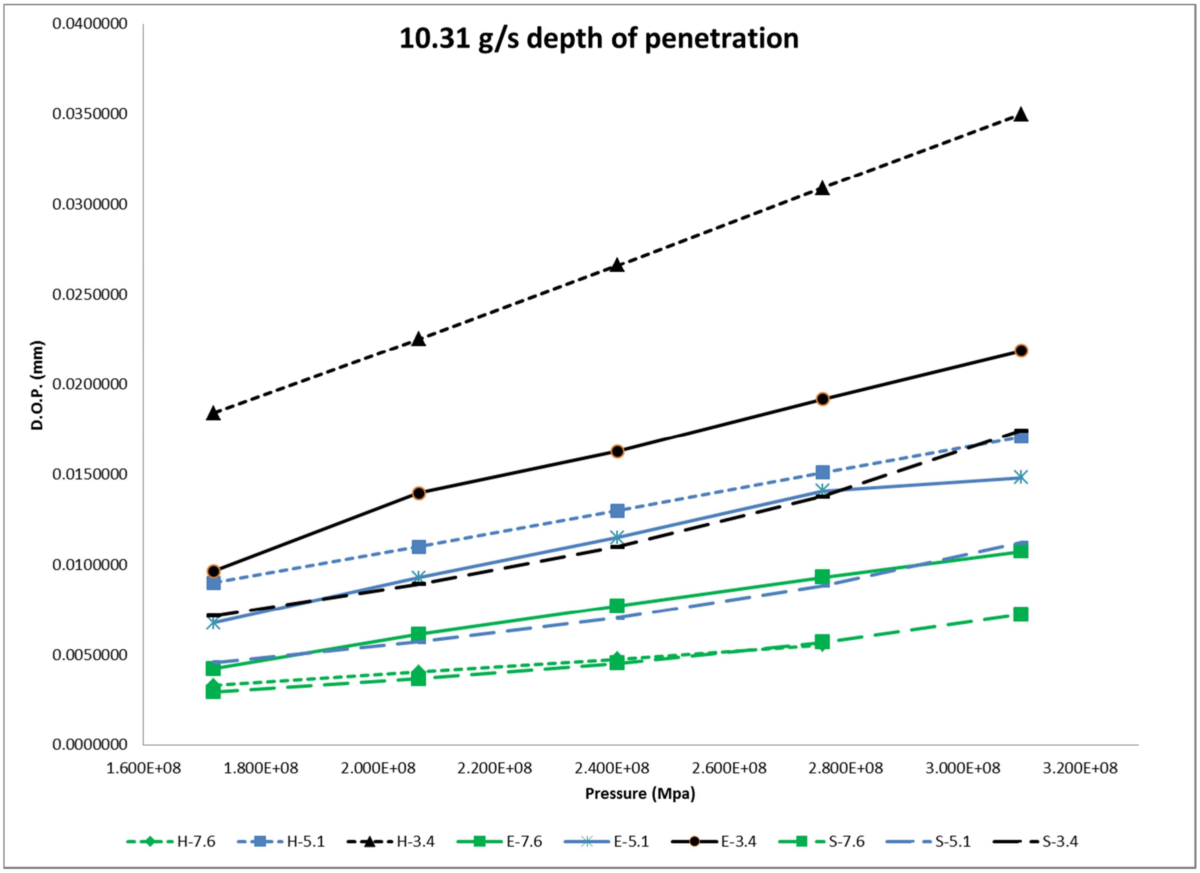

Figure 30: D.O.P. @ 10.31g/s New model (S) vs. Experiment (E) vs. Hashish (H)

Overall, a drastic improvement in the depth of penetration predication was realized over the three mass flow rates, five pressures and three feed rates tested - the forty-five cases average error of 34.8%, improved to 17.8%, 50.03% relative reduction.

To further extend the parametric study the Ks formulation was tested against some of ElTobgy's experiments found in literature carried out at four different pressures, four faster feed rates and one mass flow rate; this created an additional twenty cases to be analyzed. This approached the limits of the new model as the error reduction was only 5.2% from 29.4% with Hashish's model to 24.2% with the updated Ks formulation; a relative reduction in magnitude of 17.7%; presented in Figure 31.

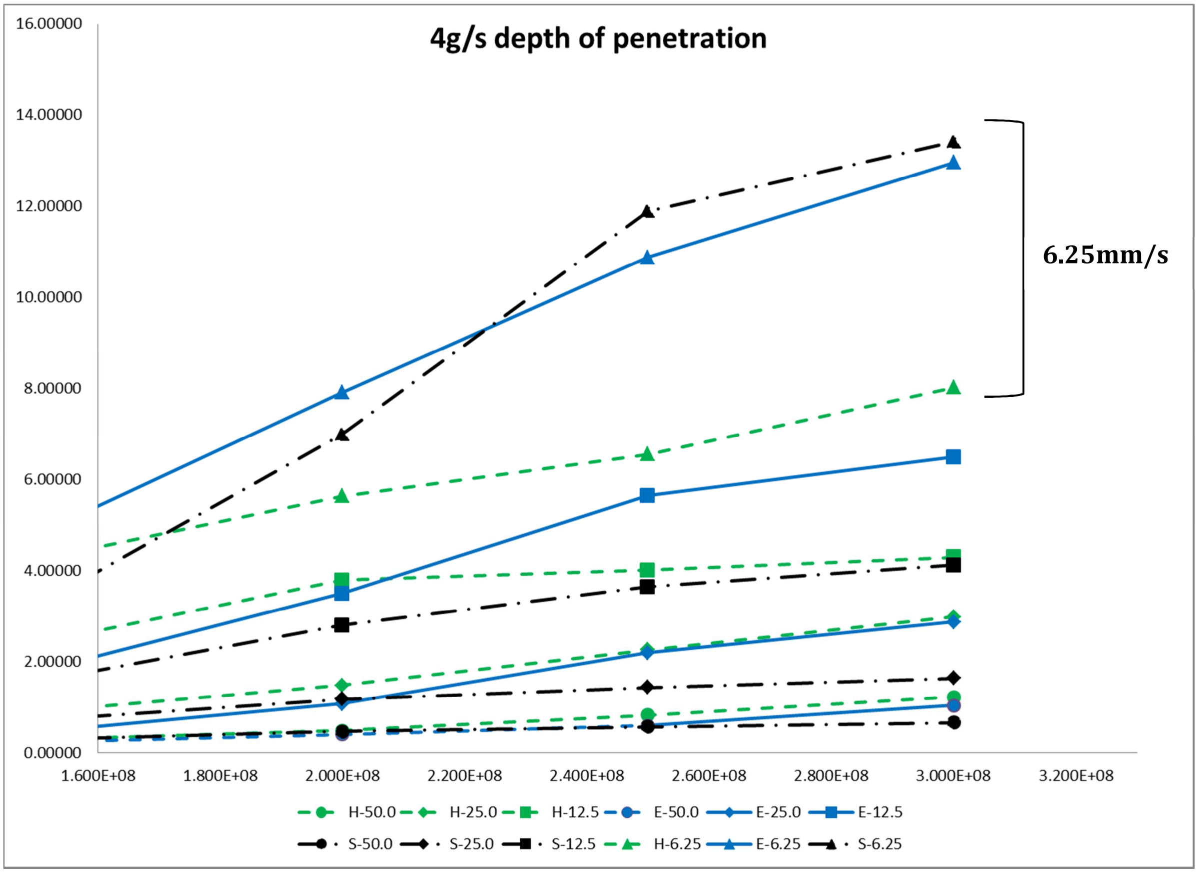

Figure 31: D.O.P. @ 4g/s New model (S) vs. Experiment (E) vs. Hashish (H)

Although the improvement in penetration prediction wasn't as significant as the previous cases the new model still had great correlation with the experiments; with drastically greater accuracy at lower feed rates as shown by the top dashed black line (new Ks formulation) compared to the blue experimental line and lastly the underestimated green dashed line representing Hashish's model – feed rate of 6.25mm/s represented by triangle points location.

More tests should be carried out to further develop the limits of the updated Ks formulation. Consideration should be given to matching the type of material to appropriate cutting feeds used in industry, or mainly for effective cutting. The second set of tests – the twenty cases – feed rates were extreme conditions where little effective cutting was taking place and would not be common in industry when cutting Ti-6Al-4V. For example, when machining titanium under the highest pump pressure and feed of 50mm/s the work piece eroded less than one millimeter. Overall, consideration to the specific industry applications trying to be understood should be recognized. Higher feed rate models should be developed but for materials such as aluminum or unhardened steel applications. The model results are tabulated below:

Table 6: Erosion model results

MFR	Hashish's Model Error	New *Ks* Model	Relative Error Reduction
4.65 g/s	33.9%	14.1%	58.5%
2.86 g/s	30.6%	13.5%	55.9%
10.31g/s	40.0%	25.7%	35.7%
45 Cases AVG	34.8%	17.8%	50.0%

A direct correlation has been observed between increasing pressure, mass flow rate of abrasive and decreasing feed rate of the mixing head nozzle resulting in an increase in depth of penetration. Most interesting, this has led to the development of a multi-layered surface plot that can be utilized as a quick reference guide for d.o.p. estimation. The surface plots created are shown in Figure 32 (45 cases) and Figure 33 (20 cases). In AWJM the numerous input parameters and their effect on cut output and quality were discussed in section 2.1 AWJM Parameters. As feed rate, mass flow rate of abrasive, or pressure change the resulting material removal of the work piece changes, represented by the depth of penetration. For a particular material, Ti-6Al-4V for these experiments, the surface plots can act as a quick reference for penetration depth prediction if the three vital input parameters are known. The surface renderings based on the results of the new Ks formulation are plotted below. As the pressure and mass flow rate of abrasive increases the d.o.p. increases. Inversely, as feed rate of the nozzle decreases across the work piece the d.o.p. increases; complete test parameters are summarized in Table 7.

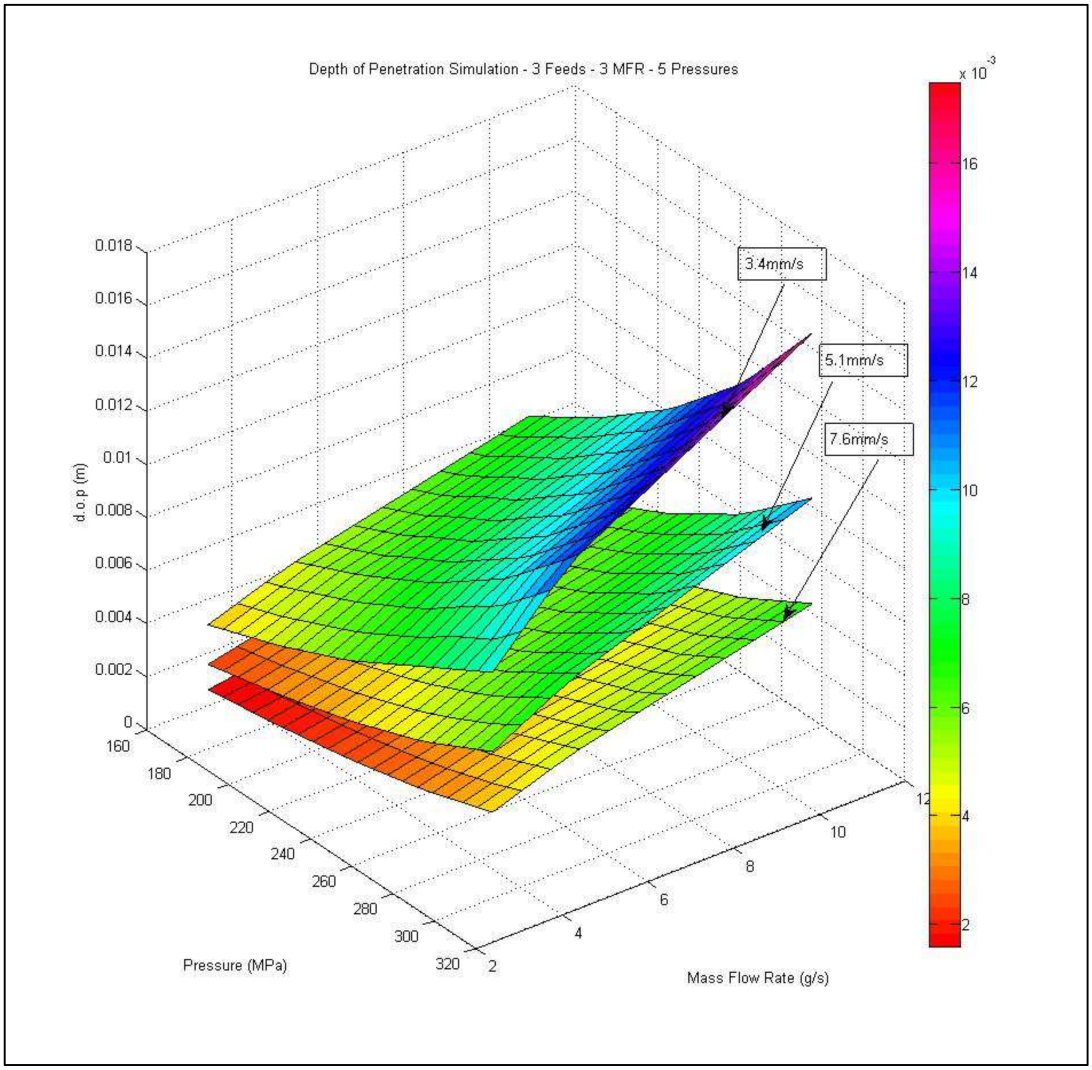

Figure 32: 3 feed, 3 MFR, 5 Pressures d.o.p.

Figure 32	Feed (mm/s)	3.4	5.1	7.6		
	Pressure (MPa)	172	207	241	276	310
	Mass flow rate (g/s)	2.86	4.65	10.31		
Figure 33	Feed (mm/s)	6.25	12.5	25	50	
	Pressure (MPa)	150	200	250	300	
	Mass flow rate (g/s)	4				

Table 7: Test parameters for surface plots

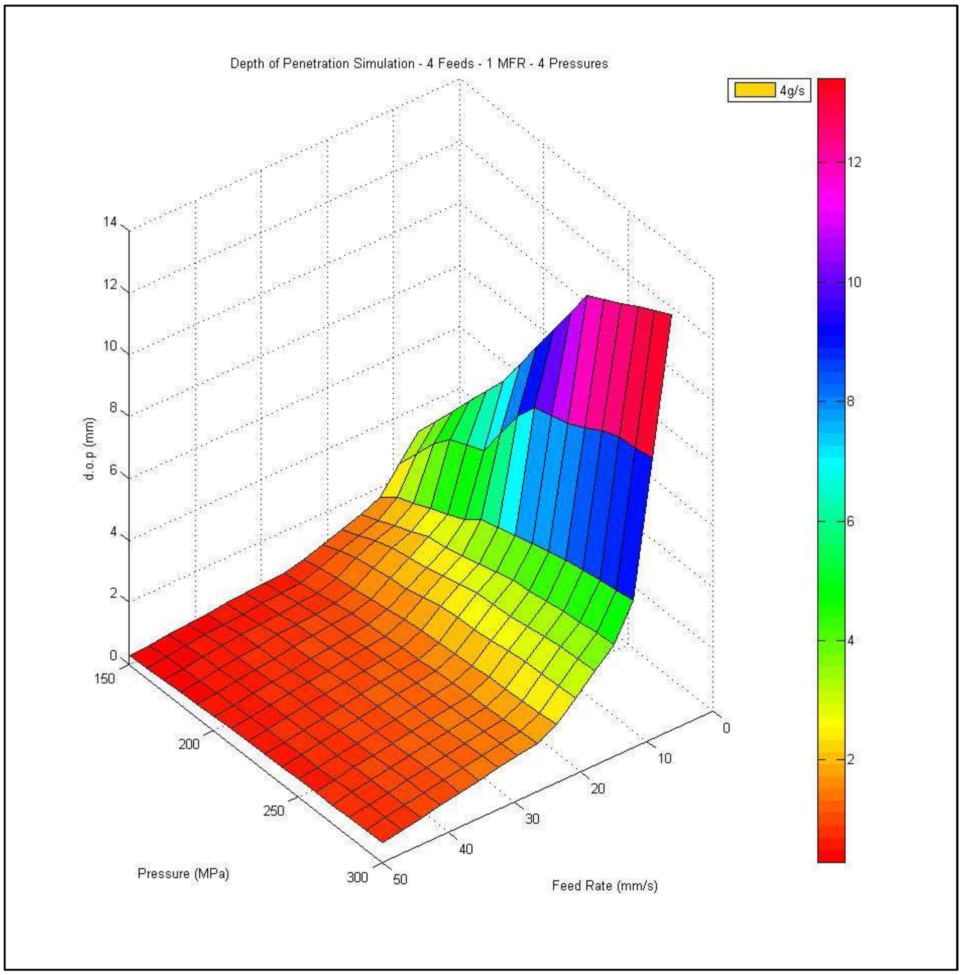

Figure 33: 4 feed, 1 MFR, 4 Pressures d.o.p.

To increase the functionality of the model and to extend to other input parameters such as different abrasive size, shape or mass flow rate the inputs for the erosion model parameters would have to be changed and the model rerun. If nozzle length, diameter, or mixing chamber dimensions were significantly changed rerunning the ANSYS model would be required to predict the velocity profile. Then the ANSYS CFD output velocity profile would be used as input to the erosion model again and rerun. With the input changes described the surface plots can be determined without any additional experiments needed. To predict erosion on other material types however the Ks formulation constants would have to be recalculated; therefore, some experiments would be required. The greater the number of feed rates, pressures and mass flow rates tested experimentally, the greater accuracy the Ks formulation prediction can generate moving forward.

7 Conclusions

AWJM uses upwards of twenty input parameters that effect the cut quality achieved making it an extremely advanced, intricate process to understand and even more difficult to predict. Overall, the CFD model provided useful insight towards understanding the inner workings of the AWJ mixing head nozzle. As particle shape became less spherical and more jagged, outlet velocity of the abrasive garnet increased by as much as 10%. Interesting, was the effect of focus tube length with the inclusion of air in the fluid mixture. Without air, the focus tube length had little effect on output velocity, as the abrasive was quickly accelerated to equilibrium due to the vast momentum difference between phases. However, with the inclusion of air the momentum transfer, between abrasive and the fluid mixture, decreased dramatically. This observation reaffirming that the focus tube length can be significantly long because the increase in air volume fraction decreases the rate that equilibrium between phases is reached. As such, with a nozzle length difference of 4 inches the output velocity of the abrasive increased as much as 20%, due to the greater time allowed for momentum change between the phases.

As expected, pressure and the volume fraction of air proved to have the greatest impact on the velocity profile upon exit from the nozzle. The input pressure provides the potential energy transformed into kinetic energy that originally is in the fluid mixture and transferred to the abrasive garnet. The volume fraction of air greatly affects the inlet velocity of the fluid mixture shown in Figure 17, which directly affects the energy transfer available to the abrasive particles. In addition, the greater the volume fraction of air the more turbulent the flow inside the mixing chamber becomes, thereby facilitating particle-fluid mixing which enables more momentum transfer; mainly acceleration of the abrasive. Therefore, the inclusion of air makes the CFD model more accurate and the mixing process more efficient.

The particle size and mass flow rate did not prove significant on the discrete phase velocity for the cases analyzed; less than 5% change. The particle size and mass flow rate directly affect the erosion model; however the output velocity from the CFD model observed little change. Until a nozzle reaches a saturation point – or clogging effect – the mass flow rate and/or particle size can increase with little change to the abrasive particle output velocity because the momentum of the air-water fluid is much greater than the abrasive particle. Made clear, the mass flow rate and size do not affect the output velocity but directly correlate to the energy available to do work, in this case erosion on the work piece.

Most useful from the CFD was the development of the 2D garnet profile at particular stand-off distances. The "top-hat" profile was observed and can be utilized to improve the new Ks numerical erosion model; this was illustrated in Figure 21. The significance of the "top-hat" profile will be discussed in Future Work.

A new Ks formulation was calculated to modify ElTobgy's erosion model, dependent on particle velocity and feed rate. This formulation had significant improvements on past empirical erosion models. Experimentally 65 variations of cutting parameters were used including nine pressures, seven feed rates and four mass flow rates, tested on Ti-6Al-4V. The new formulation in comparison to Hashish's erosion model had a reduction in error from 33.4% to 19.5% over the 65 cases; a total error reduction of 41.8%. For certain industrial cases, which bear more importance, error reduction was much more significant.

As the three inputs - mass flow rate, feed rate and pressure – are varied a multiple layered surface plot estimating the depth of penetration is created; reference Figure 32. This can be utilized as a quick reference erosion prediction tool by quickly estimating where the cutting parameters fit on a particular surface. To create a database, input parameter changes involving nozzle length, focus tube diameter, mixing head dimensions or particle shape factor would require the CFD model to be updated to ensure an accurate velocity profile is used as input to the erosion model. Changes including mass flow rate, particle size or feed rate would require the erosion model to be updated. Lastly, material changes in the work piece would require a set of experiments at a particular mass flow rate and a minimum of a few feeds rates and pressures. This will guarantee the Ks updated formulation for the new work piece material is accurate, providing enough experimental data for constants to be fitted. For industrial applications - with few materials, feed rates, and nozzle types - development of quick reference surface plots would require little work and be truly advantageous.

8 Future Work

The CFD model has been accurately set up and solver conditions optimized. Therefore, varying mixing head, orifice, abrasive inlet and focus tube dimensions to optimize abrasive-fluid mixing and coherence in the focus tube can be established. Optimization would require increase in output velocity of abrasive particles and a tightening of the "top-hat" profile thereby improving the kerf width of the cut. Increase in the velocity profile, without increase of pressure since pump technology is limited, will increase the material removal rate improving AWJM efficiency thereby gaining functionality.

Future work for the updated Ks erosion model would involve the utilization of the "top-hat" profile. Initially, Hashish's erosion model assumed a jet stream and mass flow rate divided into dx and dm sections. ElTobgy then divided the dx further to be a per particle basis for the erosion model where constants account for particles that do not contribute to erosion. From Figure 21 the 2D garnet velocity profile illustrates a maximum flat section in the centre of the curve. This maximum was used for the new Ks erosion model's abrasive initial velocity. Instead a multi-particle cutting front could be developed utilizing the profile illustrated; mainly the garnet velocity information. This would then decrease the reliance on constants to account for particles that do not cut but are simply entrained in the fluid. The leading edge particle will have a slower particle velocity followed by particles that increase in velocity and similar depth of penetration will be accurately represented with little or no reliance on efficiency terms.

9 Bibliography

A. Tazbit, F. P. (1996). Theoretical analysis of the abrasive particle acceleration process in abrasive water jet cutting. *Computational Materials Science 5*, 243-254.

ANSYS. (2009, April). *ANSYS FLUENT 12.0 Theory Guide.* Retrieved 2011-2012, from https://www.sharcnet.ca/Software/Fluent12/pdf/th/flth.pdf

Bitter, J. (1962). *A Study of Erosion Phenomena Part I.* Amsterdam, The Netherlands: Shell Internationale Research Maatschappij.

Corporation, F. I. (2012). *Comparative Cutting*. Retrieved 07 2012, from Flow: http://www.flowwaterjet.com/en/waterjet-technology/comparative-cutting.aspx

Corporation, F. I. (2012). *Intensifier Pump Detail*. Retrieved 2012, from Flow: http://www.flowwaterjet.com/en/waterjet-technology/intensifier-pump-detail.aspx

Corporation, F. I. (2012). *Our History-A History of Leadership*. Retrieved 07 2012, from Flow: http://www.flowwaterjet.com/en/waterjet-technology/history.aspx

D.H. Ahmed, R. D. (2001). *Optimising the Focus Tube Length for Abrasive Waterjet Using Numerical Simulations.* Hawthorn, Vic. 3122, Australia: Swinburne University of Technology.

ElTobgy, M. (2007). *Modelling of Abrasive Waterjet Machining using a Multi-Physics Approach.* Hamilton: McMaster University.

Finnie, I. (1960). *Erosion of Surfaces by Solid Particles.* Emeryville, Calif. : Shell Development Company.

Folk, R. (1955). Student operator error in determination of roundness, sphericity, and grain size. *Journal of Sedimentary Petrology, vol. 25, No. 4*, 297-301.

FrontlineSolvers. (2012). Optimization Problem Types - Smooth Nonlinear Optimization. Incline Village, NV, USA.

H. Liu, J. W. (2004). A study of abrasive waterjet characteristics by CFD cimulation. *Journal of Materials Processing Technology, 153-154*, 488-493.

Hashish, M. (1984). A Modelling Study of Metal Cutting with Abrasive Waterjets. *Journal of Engineering Materials and Technology, Vol. 106*, 88-100.

Hashish, M. (1989). A Model for Abrasive-Waterjet (AWJ) Machining. *Journal of Engineering Materials and Technology, Vol 111*, 154-162.

Hashish, M. (1989). Pressure effects in abrasive waterjet (AWJ) machining . *Journal of Engineering Materials and Technology 111*, 221-228.

Hongtao Zhu, C. H. (2009). Modeling Material Removal in Fracture Erosion for Brittle Materials by Abrasive Waterjet. *Advanced Materials Research Vols. 76-78*, 357-362.

(n.d.). Contact Stresses. In C. M. J. Shigley, *Mechanical Engineering Design 8th Editon* (pp. 117-121). Tata McGraw-Hill.

(n.d.). Strength and Cold Work. In C. M. J. Shigley, *Mechanical Engineering Design 8th Edition* (pp. 33-35). Tata McGraw-Hill.

Kelecy, F. J. (2008). Coupling Momentum and Continuity Increases CFD Robustness. *ANSYS Advantage, Volume II, Issue 2*. ANSYS Inc.

Li, Z. (n.d.). *Finite Difference Methods.* Retrieved 07 12, from Center for Research in Scientific Computation & Department of Mathematics: http://www4.ncsu.edu/~zhilin/TEACHING/MA402/notes1.pdf

M. ElTobgy, E.-G. N. (n.d.). *Modelling of Abrasive Waterjet Machining: A New Approach.* Hamilton: Machining System Labratory, McMaster Manufacturing Research Institute, McMaster University.

M.Hashish. (1987). An Improved Model of Erosion by Solid Particle Impact. *Proc. 7th Int. Conf. on Erosion by Liquid and Solid Impact*, (pp. 66:1-9).

Md. G. Mostofa, K. Y. (2010). Computational fluid analysis of abrasive waterjet cutting head. *Journal of Mechanical Science and Technology 24*, 249-252.

Robert W. Fox, A. T. (2006). *Introduction to Fluid Mechanics Sixth Edition.* Jonh Wiley & Sons, Inc.

Wang, J. (2009). Particle velocity models for ultra-high pressure abrasive waterjets. *Journal of Materials Processing Technology*, 4573-4577.

10 Appendix

10.1 Appendix A – CFD Model Results

Model Characteristics				P.S / P.Sh. / MFR / FTL / P / V.O.Air	At 1mm s.o.d.			At 5mm s.o.d.			At inlet		
				40 / 0.8 / 0.01 / 4 / 300 / 95%	Water Max. Velocity	Garnet Max Velocity	Air Velcoity	Water Max. Velocity	Garnet Max Velocity	Air Velcoity	Water Max. Velocity	Garnet Max. Velocity	Air Max. Velocity
	19	Particle Size (mesh)	25=0.0280''	0.25	375.123444	388.118958	375.774689	319.633026	368.291748	318.455383	1576.34644	0	1763.93762
B.C.			**40=0.0165''**	0.40	374.915497	398.561035	375.322601	319.623077	373.483704	318.498749	1576.43848	0	1764.0575
	18		60=0.0098''	0.60	374.96283	404.610321	375.537354	319.625641	376.363159	318.552979	1576.54175	0	1763.34619
	17		100=0.0059''	1.00	374.479156	402.62027	375.434967	318.974396	370.682953	317.895721	1574.46265	0	1762.11316
	12	Particle Shape (#)	0.4	0.40	374.913391	409.418365	375.453674	319.306213	370.635071	318.133423	1575.11841	0	1763.26538
	11		0.6	0.60	375.140076	400.181183	375.684509	319.632751	372.79776	318.462799	1576.599	0	1764.18005
B.C.			**0.8**	0.80	374.915497	398.561035	375.322601	319.623077	373.483704	318.498749	1576.43848	0	1764.0575
	10		1	1.00	375.121918	371.870972	375.694519	319.63208	355.24527	318.459412	1576.36377	0	1764.03076
	16	Mass flow rate (Kg/s)	0.005	0.20	374.914124	401.071228	374.865997	319.62204	375.082825	318.390381	1576.37476	0	1763.31616
B.C.			**0.01**	0.40	374.915497	398.561035	375.322601	319.623077	373.483704	318.498749	1576.43848	0	1764.0575
	15		0.015	0.60	374.974518	400.349823	374.972107	319.623657	374.129395	318.39682	1576.41125	0	1763.75574
	14		0.02	0.80	410.909882	423.953461	412.696777	353.902985	403.799225	352.003052	1651.9458	0	1855.22083
	13		0.025	1.00	374.940125	399.580322	375.361267	319.625	372.978668	318.444214	1576.69556	0	1764.0896
	20	Focus tube length	2		345.757843	351.359192	351.809753	261.833801	315.750854	262.75174	1392.73096	0	1551.05884
B.C.			**4**		374.915497	398.561035	375.322601	319.623077	373.483704	318.498749	1576.43848	0	1764.0575
	21		6		441.493195	439.901886	440.577698	377.973633	416.406525	376.308167	1553.47034	0	1774.03162
	9	Pressure (Mpa)	150		370.985474	364.65448	368.287354	266.885132	323.772552	262.209442	1240.6355	0	1420.81982
	8		200		384.465332	370.41095	381.759003	284.680847	333.567017	282.8797	1288.76721	0	1482.76563
	7		250		363.953705	393.868805	366.227722	297.234467	364.436584	294.72049	1490.57239	0	1640.86133
B.C.			**300**		374.915497	398.561035	375.322601	319.623077	373.483704	318.498749	1576.43848	0	1764.0575
	6		350		429.507507	431.315125	430.776581	394.497253	419.005951	394.397003	1693.71106	0	1903.86182
	1	V.O.Air (%)	0		181.606522	182.547485	N/A	152.281982	166.578217	N/A	775.997925	0	N/A
	2		25		275.234558	273.47757	274.165955	220.441849	252.868942	219.630539	1091.76477	0	1233.40649
	3		50		303.657806	296.703918	301.71875	221.283615	266.054382	216.203262	1130.79956	0	1243.16602
	4		75		327.349701	315.10611	325.500793	247.544678	287.028656	247.105179	1205.9502	0	1374.71082
	5		**95**		374.915497	398.561035	375.322601	319.623077	373.483704	318.498749	1576.43848	0	1764.0575

10.2 Appendix B – Experimental Results

Table 8: Experimental results – 3MFR, 5 Pressures, 3 Feeds

Metering Disk 0.154" - 2.86g/s				
		Depth (mm)		
	Feed (mm/s)	7.6	5.1	3.4
Pressure (Mpa)	172	1.626	3.454	5.791
		1.524	2.997	5.359
		1.778	3.327	5.740
	207	2.438	4.369	6.960
		2.337	4.343	6.401
		2.591	4.597	7.061
	241	3.099	5.537	8.636
		3.124	5.182	7.468
		3.200	5.436	7.544
	276	3.785	6.299	9.271
		3.759	5.690	9.449
		3.835	5.715	9.246
	310	4.521	6.477	10.236
		4.293	6.858	9.830
		4.572	7.137	9.906

Metering Disk 0.184" - 4.65g/s				
		Depth (mm)		
	Feed (mm/s)	7.6	5.1	3.4
Pressure (Mpa)	172	1.905	2.794	4.750
		2.108	3.200	4.648
		1.956	3.175	4.674
	207	3.150	4.775	6.985
		3.099	4.674	7.036

	3.023	4.826	7.163
	4.166	6.553	9.144
241	4.369	6.274	9.474
	4.267	6.629	9.119
	5.613	8.357	11.074
276	5.690	7.925	11.252
	5.436	8.458	12.040
	6.299	9.677	12.268
310	6.528	9.779	13.056
	6.325	9.601	12.624

Metering Disk 0.246" - 10.31g/s

		Depth (mm)		
	Feed (mm/s)	7.6	5.1	3.4
Pressure (Mpa)		4.216	6.833	10.185
	172	4.267	6.629	9.525
		4.216	6.858	9.246
		6.274	9.373	15.621
	207	5.969	9.144	13.386
		6.172	9.347	12.929
		7.925	10.922	16.358
	241	7.391	11.836	17.221
		7.772	11.786	15.265
		8.992	13.538	18.999
	276	9.296	14.656	19.050
		9.652	14.046	19.507
		11.176	15.799	21.539
	310	10.185	14.072	21.590
		10.846	14.605	22.504

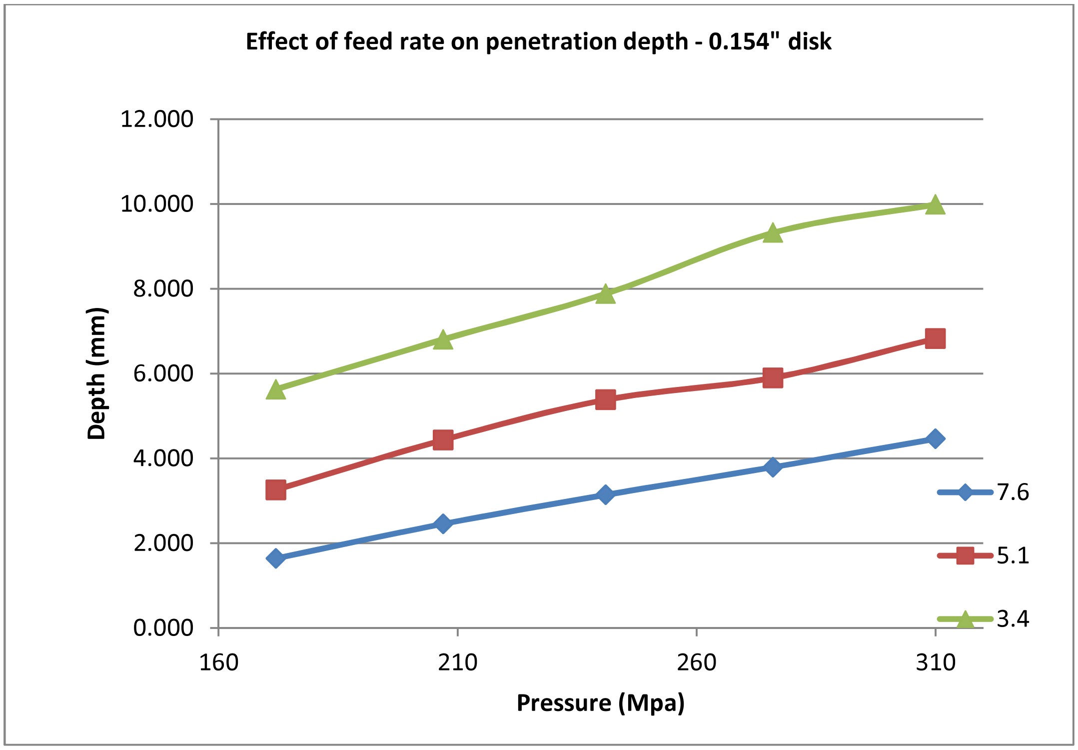

Figure 34: d.o.p. 0.154`` disk

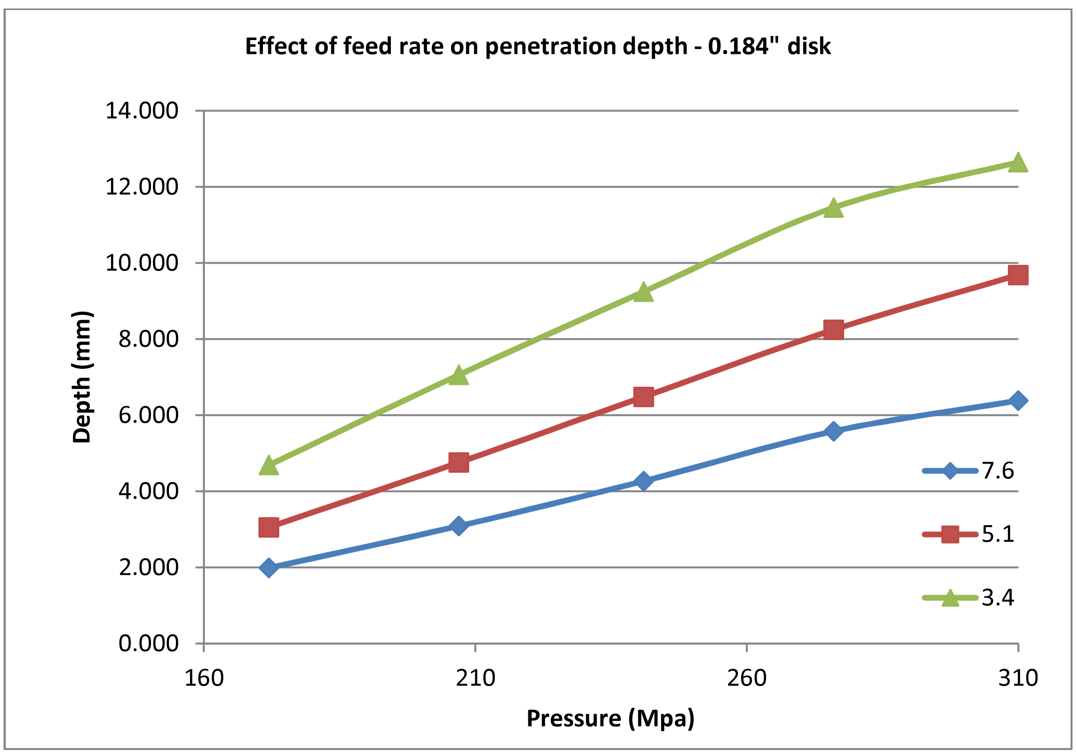

Figure 35: d.o.p. 0.184`` disk

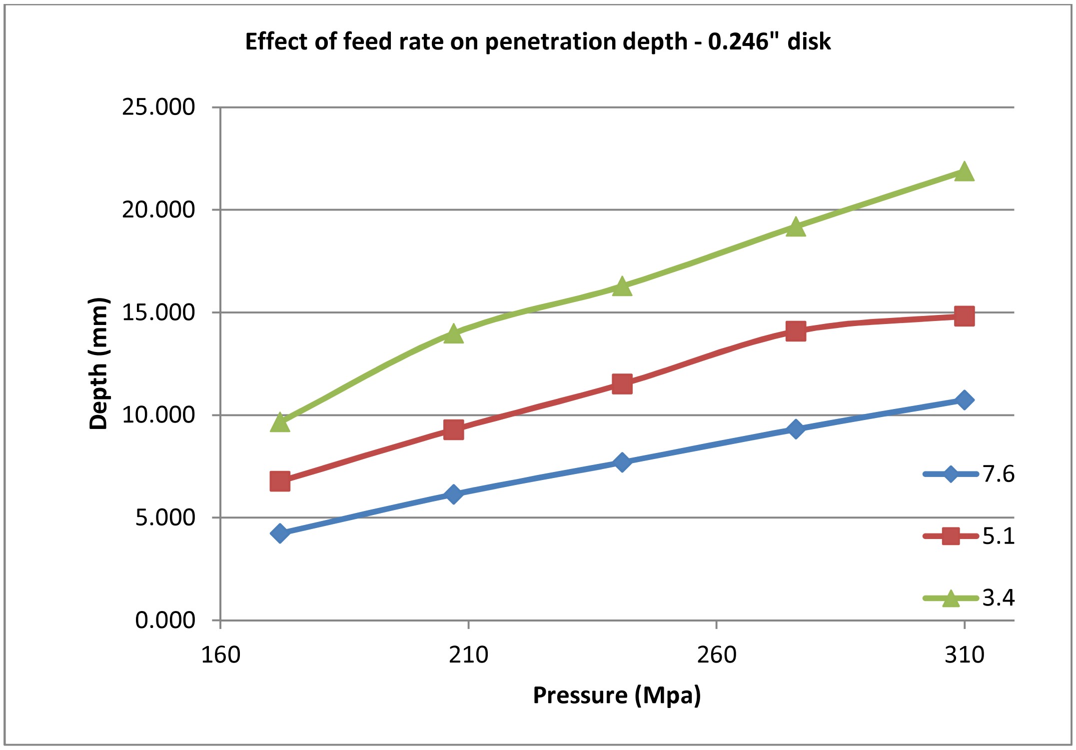

Figure 36: d.o.p. 0.246`` disk

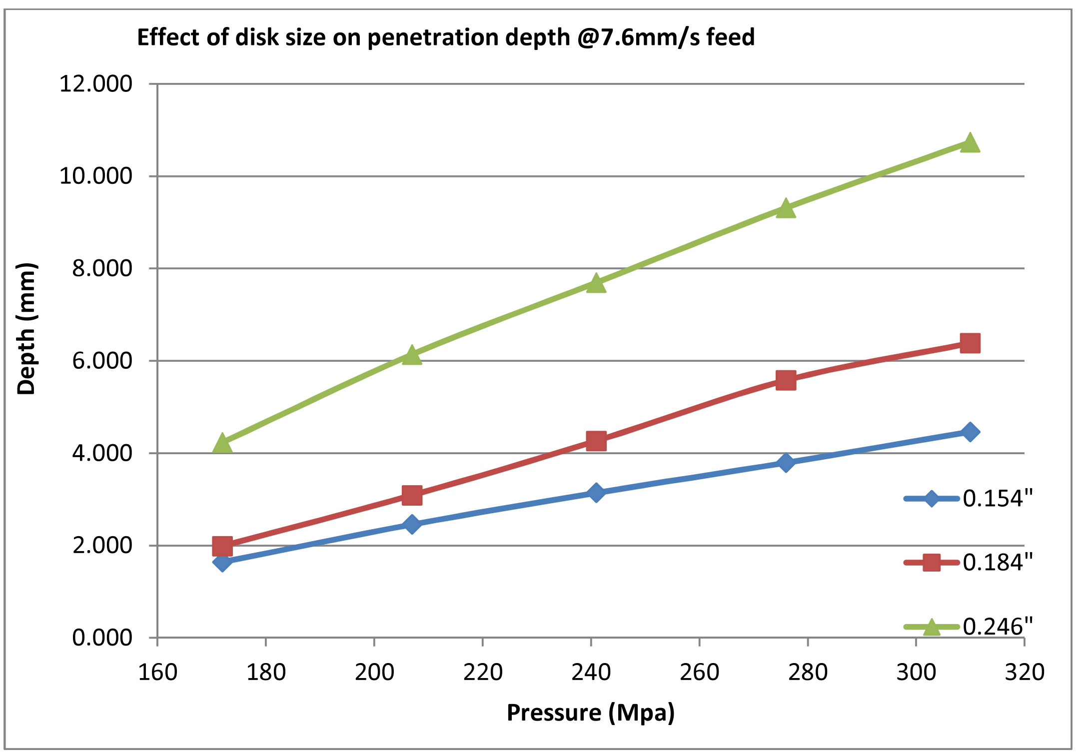

Figure 37: d.o.p. 7.6mm/s feed

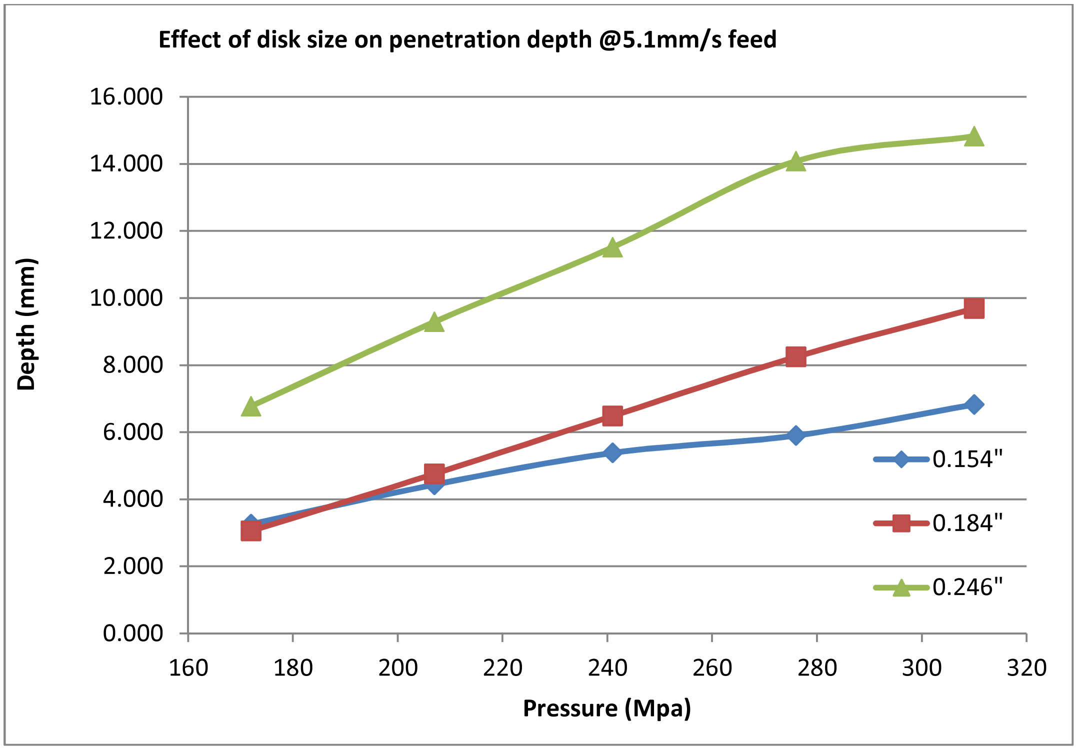

Figure 38: d.o.p. 5.1mm/s feed

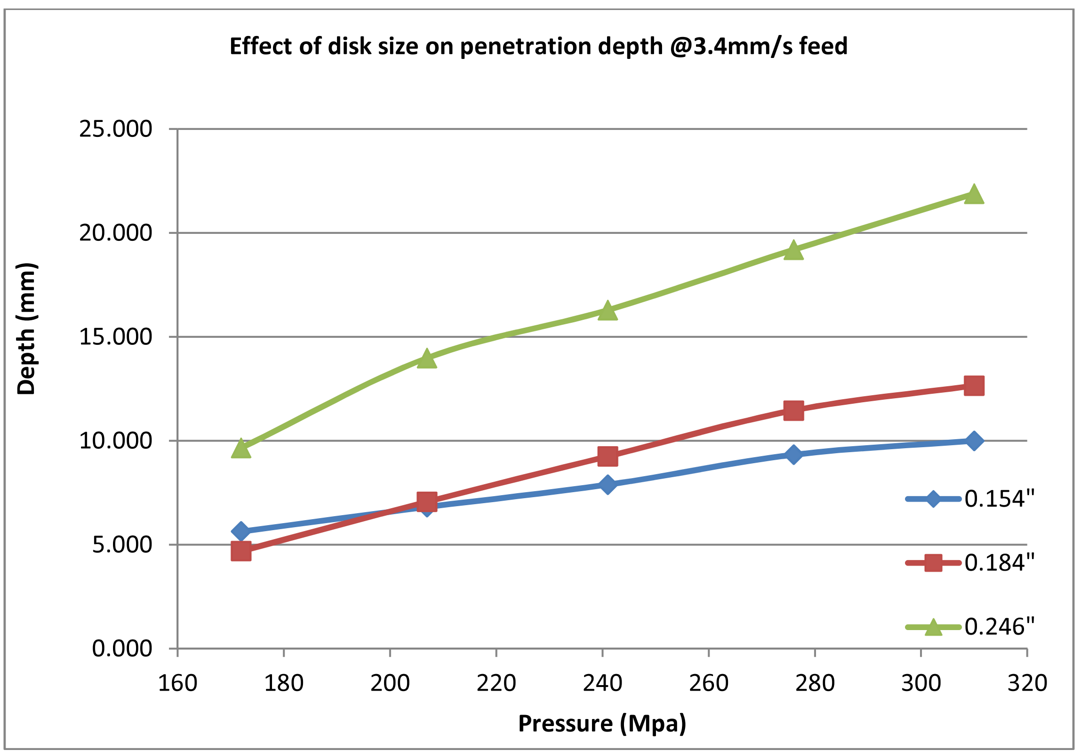

Figure 39: d.o.p. 3.4mm/s feed

10.3 Appendix C – Erosion Model Results

P	1.72000E+08	2.07000E+08	2.41000E+08	2.76000E+08	3.10000E+08	
7.6mm/s	0.00092	0.00112	0.00132	0.00154	0.00174	Hashish Model
5.1mm/s	0.00250	0.00305	0.00361	0.00419	0.00474	
3.4mm/s	0.00511	0.00625	0.00738	0.00857	0.00970	
7.6mm/s	0.00164	0.00246	0.00314	0.00379	0.00446	Experimental
5.1mm/s	0.00326	0.00444	0.00538	0.00590	0.00682	
3.4mm/s	0.00563	0.00681	0.00788	0.00932	0.00999	
7.6mm/s	0.00177	0.00228	0.00275	0.00316	0.00340	Simulation
5.1mm/s	0.00274	0.00373	0.00476	0.00566	0.00608	
3.4mm/s	0.00407	0.00594	0.00832	0.01072	0.01151	
7.6mm/s	0.00149	0.00182	0.00215	0.00250	0.00283	Hashish Model
5.1mm/s	0.00406	0.00497	0.00586	0.00681	0.00771	
3.4mm/s	0.00831	0.01016	0.01200	0.01394	0.01578	
7.6mm/s	0.00199	0.00309	0.00427	0.00558	0.00638	Experimental
5.1mm/s	0.00306	0.00476	0.00649	0.00825	0.00969	
3.4mm/s	0.00469	0.00706	0.00925	0.01146	0.01265	
7.6mm/s	0.00223	0.00286	0.00345	0.00395	0.00426	Simulation
5.1mm/s	0.00344	0.00465	0.00593	0.00703	0.00791	
3.4mm/s	0.00508	0.00739	0.01033	0.01328	0.01427	
7.6mm/s	0.00330	0.00404	0.00477	0.00554	0.00627	Hashish Model
5.1mm/s	0.00900	0.01101	0.01300	0.01510	0.01709	
3.4mm/s	0.01842	0.02253	0.02661	0.03090	0.03498	
7.6mm/s	0.00423	0.00614	0.00770	0.00931	0.01074	Experimental
5.1mm/s	0.00677	0.00929	0.01151	0.01408	0.01483	
3.4mm/s	0.00965	0.01398	0.01628	0.01919	0.02188	
7.6mm/s	0.00322	0.00410	0.00493	0.00564	0.00607	Simulation
5.1mm/s	0.00491	0.00663	0.00842	0.00998	0.01073	
3.4mm/s	0.00723	0.01048	0.01462	0.01878	0.02018	

			Pressure (Mpa)					
			1.720E+08	2.070E+08	2.410E+08	2.760E+08	3.100E+08	
2.86	Feed (m/s)	7.6mm/s	0.0009157	0.0011206	0.0013232	0.0015364	0.001739396	Hashish
			0.0016425	0.0024553	0.0031411	0.0037931	0.004461933	Experiment
			0.0015939	0.0020178	0.0025195	0.0031914	0.004084319	Simulation
		5.1mm/s	0.0024959	0.0030543	0.0036065	0.0041878	0.004740969	Hashish
			0.0032597	0.0044365	0.0053848	0.0059013	0.006824133	Experiment
			0.0025459	0.0031967	0.0039664	0.0050000	0.006366794	Simulation
		3.4mm/s	0.0051091	0.0062520	0.0073824	0.0085723	0.009704567	Hashish
			0.0056303	0.0068072	0.0078825	0.0093218	0.009990667	Experiment
			0.0040370	0.0050460	0.0062337	0.0078274	0.009935126	Simulation
4.65	Feed (m/s)	7.6mm/s	0.0014888	0.0018219	0.0021513	0.0024980	0.002828015	Hashish
			0.0019897	0.0030903	0.0042672	0.0055795	0.006383867	Experiment
			0.0020200	0.0025454	0.0031631	0.0039924	0.005093681	Simulation
		5.1mm/s	0.0040580	0.0049658	0.0058636	0.0068087	0.007708039	Hashish
			0.0030565	0.0047583	0.0064855	0.0082465	0.009685867	Experiment
			0.0031956	0.0040026	0.0049526	0.0062276	0.007912538	Simulation
		3.4mm/s	0.0083065	0.0101647	0.0120024	0.0139369	0.01577765	Hashish
			0.0046905	0.0070612	0.0092456	0.0114554	0.0126492	Experiment
			0.0050385	0.0062852	0.0077542	0.0097214	0.012326172	Simulation
10.31	Feed (m/s)	7.6mm/s	0.0033009	0.0040394	0.0047697	0.0055385	0.006270118	Hashish
			0.0042333	0.0061383	0.0076962	0.0093133	0.010735733	Experiment
			0.0029204	0.0036588	0.0045294	0.0056961	0.007241805	Simulation
		5.1mm/s	0.0089970	0.0110096	0.0130000	0.0150953	0.017089034	Hashish
			0.0067733	0.0092879	0.0115147	0.0140801	0.014825133	Experiment
			0.0045750	0.0057120	0.0070514	0.0088453	0.011219605	Simulation
		3.4mm/s	0.0184158	0.0225350	0.0266087	0.0308968	0.034976984	Hashish
			0.0096520	0.0139785	0.0162814	0.0191855	0.021877867	Experiment
			0.0071734	0.0089330	0.0110041	0.0137775	0.017448046	Simulation

feed - 7.6mm/s		mass flow rate		
	Pressure	2.86	4.65	10.31
	172000000	0.0015939	0.0020200	0.0029204
	207000000	0.0020178	0.0025454	0.0036588
	241000000	0.0025195	0.0031631	0.0045294
	276000000	0.0031914	0.0039924	0.0056961
	310000000	0.004084319	0.005093681	0.007241805

feed - 5.1mm/s		mass flow rate		
	Pressure	2.86	4.65	10.31
	172000000	0.0025459	0.0031956	0.0045750
	207000000	0.0031967	0.0040026	0.0057120
	241000000	0.0039664	0.0049526	0.0070514
	276000000	0.0050000	0.0062276	0.0088453
	310000000	0.006366794	0.007912538	0.011219605

feed - 3.4mm/s		mass flow rate		
	Pressure	2.86	4.65	10.31
	172000000	0.0040370	0.0050385	0.0071734
	207000000	0.0050460	0.0062852	0.0089330
	241000000	0.0062337	0.0077542	0.0110041
	276000000	0.0078274	0.0097214	0.0137775
	310000000	0.009935126	0.012326172	0.017448046

u	150	200	250	300	300 +/-15,30	Model	
50	0.3	0.49	0.83	1.22	4.39	Hashish Model Sim	4g/s
25.00000	0.89000	1.48000	2.26000	2.99000	3.81000		
12.50000	2.40000	3.79000	4.01000	4.30000	4.03000		
6.25000	4.24000	5.64000	6.56000	8.02000	3.39000		
50.00000	0.23000	0.41000	0.60000	1.04000	7.14000	Experimental	
25.00000	0.45000	1.08000	2.20000	2.88000	6.56000		
12.50000	1.78000	3.50000	5.65000	6.49000	6.48000		
6.25000	4.79000	7.91000	10.88000	12.96000	6.01000		
50.00000	0.29117	0.47136	0.57134	0.66011	0.16618	Simulation	
25.00000	0.70824	1.17576	1.43831	1.63802	0.15462		
12.50000	1.56271	2.80503	3.64380	4.12653			
6.25000	3.22779	6.99651	11.89335	13.41884			

		mm/S	1.500E+08	2.000E+08	2.500E+08	3.000E+08	300 +/-15,30	Model
4g/s	Feed (m/s)	50.00000	0.30000	0.49000	0.83000	1.22000	4.39000	Hashish
			0.23000	0.41000	0.60000	1.04000	7.14000	Experiment
			0.29117	0.47136	0.57134	0.66011	0.16618	Simulation
		25	0.89000	1.48000	2.26000	2.99000	3.81000	Hashish
			0.45000	1.08000	2.20000	2.88000	6.56000	Experiment
			0.70824	1.17576	1.43831	1.63802	0.15462	Simulation
		12.5	2.40000	3.79000	4.01000	4.30000	4.03000	Hashish
			1.78000	3.50000	5.65000	6.49000	6.48000	Experiment
			1.56271	2.80503	3.64380	4.12653		Simulation
		6.25	4.24000	5.64000	6.56000	8.02000	3.39000	Hashish
			4.79000	7.91000	10.88000	12.96000	6.01000	Experiment
			3.22779	6.99651	11.89335	13.41884		Simulation

4g/s		mass flow rate			
	Pressure	50.00	25.00	12.50	6.25
	1.500E+08	0.29117	0.70824	1.56271	3.22779
	2.000E+08	0.47136	1.17576	2.80503	6.99651
	2.500E+08	0.57134	1.43831	3.64380	11.89335
	3.000E+08	0.66011	1.63802	4.12653	13.41884

Simulation

V=386

Constants

Ks	1.70000E+10		**theta**	-89.9988719	deg	**I=0.5*mass_p*((**	4.43E-17		**Xxk**	0.1000000355	m
Vc	0.00000E+00	m/s	**#p**	10000		**b**	3.81000E-04	m	**XyL**	0.2000000000	m
V	-3.86000E+02	m/s	**dp**	1.77E-04	80 mesh	**t**	3.55E-08	m			
eps	5.98782E+06		**Volp**	2.90E-12	m^3	**r**	0.000381	m			
dj	7.62000E-01	mm	**massp**	1.13E-08	kg	**dtS**	9.34E-09	s			
ma	2.42000E-03	kg/s	**time**	4.67E-02	s	**Xxo**	9.99115E-02	m			
c	0.00000E+00		**x**	3.55E-04	m	**Xyo**	2.00089E-01	m			
u	7.60000E-03	m/s	**dx**	3.55E-08	m	**phio**	0	rad			
sig	8.14286E+09		**dt**	4.67E-06	s	**F=Ks*b*t**	2.29919E-01	N			
Cf	2.00000E-03		**dm**	1.13E-08	kg	**thetA**	-1.570776638	rad			

Note:
must locate when Vx goes r
from theta=theta+phi calcu

	Step														
Solution	1	2	3	4	5	6	7	8	9	10	11	12	13	14	15
F=Ks*b*t	2.29919E-01	2.29919E-01	2.29919E-01	2.29919E-01	2.29919E-01	2.29919E-01	2.29919E-01	2.29919E-01	2.29919E-01	2.29919E-01	2.29919E-01	2.29919E-01	2.29919E-01	2.29919E-01	2.29919E-01
theta_rad	1.57082E+00	1.57082E+00	1.57082E+00	1.57082E+00	1.57082E+00	1.57082E+00	1.57082E+00	1.57082E+00	1.57082E+00	1.57082E+00	1.57082E+00	1.57082E+00	1.57082E+00	1.57082E+00	1.57082E+00
theta_deg	90.00113	90.00113	90.00113	90.00113	90.00113	90.00113	90.00113	90.00113	90.00114	90.00114	90.00114	90.00114	90.00114	90.00115	90.00115
Ax=(F/m)*cos(theta)	-4.00496E+02	-4.00565E+02	-4.00704E+02	-4.00911E+02	-4.01188E+02	-4.01533E+02	-4.01948E+02	-4.02432E+02	-4.02986E+02	-4.03608E+02	-4.04300E+02	-4.05062E+02	-4.05893E+02	-4.06794E+02	-4.07764E+02
Ay=(F/m)*sin(theta)	2.03410E+07	2.03410E+07	2.03410E+07	2.03410E+07	2.03410E+07	2.03410E+07	2.03410E+07	2.03410E+07	2.03410E+07	2.03410E+07	2.03410E+07	2.03410E+07	2.03410E+07	2.03410E+07	2.03410E+07
phi''=(F*r/I)*cos(theta)	-3.89643E+07	-3.89710E+07	-3.89845E+07	-3.90046E+07	-3.90316E+07	-3.90652E+07	-3.91056E+07	-3.91526E+07	-3.92065E+07	-3.92671E+07	-3.93344E+07	-3.94085E+07	-3.94893E+07	-3.95770E+07	-3.96714E+07
Vx=Vox+(Ax*dtS)	7.59626E-03	7.59252E-03	7.58877E-03	7.58503E-03	7.58128E-03	7.57753E-03	7.57378E-03	7.57002E-03	7.56625E-03	7.56248E-03	7.55870E-03	7.55492E-03	7.55113E-03	7.54733E-03	7.54352E-03
Vy=Voy-(Ay*dtS)	-3.85810E+02	-3.85620E+02	-3.85430E+02	-3.85240E+02	-3.85050E+02	-3.84860E+02	-3.84670E+02	-3.84480E+02	-3.84290E+02	-3.84100E+02	-3.83910E+02	-3.83720E+02	-3.83530E+02	-3.83340E+02	-3.83150E+02
phi'=phio+(phi''*dtS)	-3.63986E-01	-7.28034E-01	-1.09221E+00	-1.45657E+00	-1.82118E+00	-2.18611E+00	-2.55142E+00	-2.91716E+00	-3.28341E+00	-3.65023E+00	-4.01767E+00	-4.38580E+00	-4.75469E+00	-5.12440E+00	-5.49499E+00
Xx=Xxo+(Vx*dtS)	9.99115E-02	9.99115E-02	9.99115E-02	9.99115E-02	9.99115E-02	9.99115E-02	9.99115E-02	9.99115E-02	9.99115E-02	9.99115E-02	9.99115E-02	9.99115E-02	9.99115E-02	9.99115E-02	9.99115E-02
Xy=Xyo+(Vy*dtS)	2.00085E-01	2.00081E-01	2.00078E-01	2.00074E-01	2.00070E-01	2.00067E-01	2.00063E-01	2.00060E-01	2.00056E-01	2.00053E-01	2.00049E-01	2.00045E-01	2.00042E-01	2.00038E-01	2.00035E-01
phi=phio+(phi'*dtS)	3.40018E-09	1.02011E-08	2.04040E-08	3.40106E-08	5.10232E-08	7.14448E-08	9.52789E-08	1.22530E-07	1.53202E-07	1.87300E-07	2.24831E-07	2.65802E-07	3.10218E-07	3.58087E-07	4.09419E-07
delK	0.00000E+00	0.00000E+00	2.16840E-19	4.33681E-19	9.75782E-19	1.95156E-18	3.46945E-18	5.74627E-18	8.99888E-18	1.33357E-17	1.92988E-17	2.68882E-17	3.66460E-17	4.87891E-17	6.38595E-17
delL	2.59094E-12	7.77325E-12	1.55478E-11	2.59161E-11	3.88797E-11	5.44410E-11	7.26025E-11	9.33676E-11	1.16740E-10	1.42723E-10	1.71322E-10	2.02541E-10	2.36386E-10	2.72863E-10	3.11977E-10
XxK=Xxo+delK	1.00000E-01	1.00293E-01	1.00293E-01	1.00293E-01	1.00293E-01	1.00293E-01	1.00293E-01	1.00293E-01	1.00293E-01	1.00293E-01	1.00293E-01	1.00293E-01	1.00293E-01	1.00293E-01	1.00293E-01
XyL=Xyo+delL	2.00000E-01	1.99700E-01	1.99697E-01	1.99693E-01	1.99689E-01	1.99686E-01	1.99682E-01	1.99679E-01	1.99675E-01	1.99672E-01	1.99668E-01	1.99664E-01	1.99661E-01	1.99657E-01	1.99654E-01
theta= theta+phi	1.57082E+00	1.57082E+00	1.57082E+00	1.57082E+00	1.57082E+00	1.57082E+00	1.57082E+00	1.57082E+00	1.57082E+00	1.57082E+00	1.57082E+00	1.57082E+00	1.57082E+00	1.57082E+00	1.57082E+00
delAy		1.35973E-06	2.72319E-06	2.52597E-04	2.53960E-04	6.28091E-04	1.12649E-03	1.74913E-03	2.62029E-03	3.73997E-03	4.98391E-03	6.84913E-03	8.71437E-03	1.12009E-02	1.39359E-02
deltheta (deg)		-1.94816E-07	-3.89569E-07	-5.84294E-07	-7.79023E-07	-9.73790E-07	-1.16863E-06	-1.36357E-06	-1.55865E-06	-1.75391E-06	-1.94937E-06	-2.14506E-06	-2.34103E-06	-2.53731E-06	-2.73392E-06
delVy		-1.90016E-01	-1.90016E-01	-1.90016E-01	-1.90016E-01	-1.90016E-01	-1.90016E-01	-1.90016E-01	-1.90016E-01	-1.90016E-01	-1.90016E-01	-1.90016E-01	-1.90016E-01	-1.90016E-01	-1.90016E-01
delVx		-3.74189E-06	-3.74318E-06	-3.74512E-06	-3.74770E-06	-3.75093E-06	-3.75481E-06	-3.75933E-06	-3.76450E-06	-3.77031E-06	-3.77678E-06	-3.78389E-06	-3.79166E-06	-3.80007E-06	-3.80914E-06
delXy		3.60228E-06	3.60050E-06	3.59873E-06	3.59695E-06	3.59518E-06	3.59340E-06	3.59163E-06	3.58985E-06	3.58808E-06	3.58630E-06	3.58453E-06	3.58275E-06	3.58098E-06	3.57920E-06
delXx		-7.09256E-11	-7.08907E-11	-7.08557E-11	-7.08207E-11	-7.07856E-11	-7.07506E-11	-7.07154E-11	-7.06803E-11	-7.06451E-11	-7.06098E-11	-7.05744E-11	-7.05390E-11	-7.05035E-11	-7.04679E-11
Vy (m/s)		-385.620	-385.430	-385.240	-385.050	-384.860	-384.670	-384.480	-384.290	-384.100	-383.910	-383.720	-383.530	-383.340	-383.150
Xy (m)		0.20008	0.20008	0.20007	0.20007	0.20007	0.20006	0.20006	0.20006	0.20005	0.20005	0.20005	0.20004	0.20004	0.20003
Xx (m)		0.09991	0.09991	0.09991	0.09991	0.09991	0.09991	0.09991	0.09991	0.09991	0.09991	0.09991	0.09991	0.09991	0.09991
h (m)		0.00001	0.00001	0.00001	0.00002	0.00002	0.00003	0.00003	0.00003	0.00004	0.00004	0.00004	0.00005	0.00005	0.00005
h @dtS=500 (mm)	1.62721	1.62721E+00													

10.4 Appendix D - Mesh Method Settings Dialog Box (ANSYS, 2009)

The **Mesh Method Settings** dialog box allows you to apply settings for the smoothing, layering, or remeshing methods.

Smoothing contains parameters to be specified for the smoothing mesh update method.

Spring Constant Factor controls the spring stiffness.

Boundary Node Relaxation specifies how the node positions on the deforming boundaries are updated. This applies only if your model contains deforming boundaries.

Convergence Tolerance controls the smoothing convergence.

Number of Iterations specifies the number of iterations.

Layering contains parameters to be specified for the layering mesh update method.

Options specifies the criteria for splitting or collapsing cell layers.

Height Based specifies that the cell layers are split or merged based on height.

Ratio Based specifies that the cell layers are split or merged based on ratios.

Split Factor specifies the value of α_s in this equation in the separate Theory Guide. It controls the height or ratio at which the cells are split.

Collapse Factor specifies the value of α_c in this equation in the separate Theory Guide. It controls the height or ratio at which the cells are collapsed and merged into the next layer.

Remeshing contains parameters to be specified for the remeshing mesh update method.

Remeshing Methods contain options that control remeshing.

Local Cell allows you to remesh deforming boundary cells.

Local Face allows you to remesh deforming boundary faces. This option is available for 3D cases.

Region Face allows you to remesh a region.

2.5D enables the 2.5D model. This option will appear only for 3D cases. See Section 11.3.2 for more information on **ANSYS FLUENT**'s 2.5D model

Parameters contains parameters that control remeshing.

Minimum Length Scale specifies the lower limit of cell size below which the cells are marked for remeshing.

Maximum Length Scale specifies the upper limit of cell size above which the cells are marked for remeshing.

Maximum Cell Skewness specifies the desired maximum skewness for the mesh.

Maximum Face Skewness specifies the desired maximum skewness for the surface mesh. This option is active, when **Local Face** is selected under **Remeshing Methods**.

Size Remesh Interval specifies the interval in time steps for remeshing based on the above size criteria only. Marking of cells based on skewness occurs automatically at every time step when **Remeshing** is enabled.

Mesh Scale Info... opens the **Mesh Scale Info** dialog box, in which you can view the statistics of the mesh such as minimum and maximum length scale values and maximum cell and face skewness vales.

Use Defaults resets the remeshing parameters to the default values.

Sizing Function contains parameters that control the sizing function.

On allows you to enable or disable the sizing function.

Resolution sets the resolution for the sizing function. See Section 11.3.1 for more information. This item will appear only if **Sizing Function** is enabled.

Variation specifies the value of α in this equation in the separate Theory Guide. This item will appear only if **Sizing Function** is enabled.

Rate specifies the value of β in this equation in the separate Theory Guide. This item will appear only if **Sizing Function** is enabled.

Use Defaults resets the sizing function parameters to the default values. This item will appear only if **Sizing Function** is enabled.

10.5 Appendix E – ANSYS Fluent Parameters

FLUENT
Version: 2d, dp, pbns, eulerian, rke (2d, double precision, pressure-based, Eulerian, realizable k-epsilon)
Release: 12.1.4
Title:

Models

Model	Settings
Space	2D
Time	Steady
Viscous	Realizable k-epsilon turbulence model
Wall Treatment	Enhanced Wall Treatment
Multiphase k-epsilon Models	Mixture k-epsilon
Heat Transfer	Disabled
Solidification and Melting	Disabled
Species Transport	Disabled
Coupled Dispersed Phase	Enabled
Pollutants	Disabled
Pollutants	Disabled
Soot	Disabled

Material Properties

Material: titanium (inert-particle)

Property	Units	Method	Value(s)
Density	kg/m3	constant	3893
Cp (Specific Heat)	j/kg-k	constant	544.25
Thermal Conductivity	w/m-k	constant	7.4400001

Material: water-liquid (fluid)

Property	Units	Method	Value(s)
Density	kg/m3	constant	998.2
Cp (Specific Heat)	j/kg-k	constant	4182
Thermal Conductivity	w/m-k	constant	0.6
Viscosity	kg/m-s	constant	0.001003
Molecular Weight	kg/kgmol	constant	18.0152
Reference Temperature	k	constant	298
Thermal Expansion Coefficient	1/k	constant	0
Speed of Sound	m/s	none	#f

Material: anthracite (inert-particle)

Property	Units	Method	Value(s)
Density	kg/m3	constant	1550
Cp (Specific Heat)	j/kg-k	constant	1680

Thermal Conductivity w/m-k constant 0.33

Material: air (fluid)

Property	Units	Method	Value(s)
Density	kg/m3	constant	1.225
Cp (Specific Heat)	j/kg-k	constant	1006.43
Thermal Conductivity	w/m-k	constant	0.0242
Viscosity	kg/m-s	constant	1.7894e-05
Molecular Weight	kg/kgmol	constant	28.966
Reference Temperature	k	constant	298.15
Thermal Expansion Coefficient	1/k	constant	0
Speed of Sound	m/s	none	#f

Material: aluminum (solid)

Property	Units	Method	Value(s)
Density	kg/m3	constant	2719
Cp (Specific Heat)	j/kg-k	constant	871
Thermal Conductivity	w/m-k	constant	202.4

Cell Zone Conditions

Zones

name	id	type
surface_body	2	fluid

Setup Conditions

surface_body

Condition	Value
Material Name	air
Specify source terms?	no
Source Terms	((k) (epsilon))
Specify fixed values?	no
Fixed Values	((k (inactive . #f) (constant . 0) (profile)) (epsilon (inactive . #f) (constant . 0) (profile)))
Motion Type	0
X-Velocity Of Zone (m/s)	0
Y-Velocity Of Zone (m/s)	0
Rotation speed (rad/s)	0
X-Origin of Rotation-Axis (in)	0
Y-Origin of Rotation-Axis (in)	0
Deactivated Thread	no
Laminar zone?	no
Set Turbulent Viscosity to zero within laminar zone?	yes
Porous zone?	no
Porosity	1

Boundary Conditions

Zones

name	id	type
atmph2	7	pressure-inlet
atmph1	6	pressure-inlet
inlet	9	pressure-inlet
air_mass_outlet	11	velocity-inlet
outlet	5	pressure-outlet
wall	8	wall
mass_inlet	10	velocity-inlet

Setup Conditions

atmph2

Condition	Value
Reference Frame	0
Gauge Total Pressure (pascal)	0
Supersonic/Initial Gauge Pressure (pascal)	0
Direction Specification Method	1
Coordinate System	0
Turbulent Specification Method	1
Turbulent Kinetic Energy (m2/s2)	1
Turbulent Dissipation Rate (m2/s3)	1
Turbulent Intensity (%)	0.099999998
Turbulent Length Scale (in)	1
Hydraulic Diameter (in)	1
Turbulent Viscosity Ratio	10
Discrete Phase BC Type	4
Discrete Phase BC Function	none
is zone used in mixing-plane model?	no

atmph1

Condition	Value
Reference Frame	0
Gauge Total Pressure (pascal)	0
Supersonic/Initial Gauge Pressure (pascal)	0
Direction Specification Method	1
Coordinate System	0
Turbulent Specification Method	3
Turbulent Kinetic Energy (m2/s2)	1
Turbulent Dissipation Rate (m2/s3)	1
Turbulent Intensity (%)	0.099999998
Turbulent Length Scale (in)	1
Hydraulic Diameter (in)	1
Turbulent Viscosity Ratio	10
Discrete Phase BC Type	4
Discrete Phase BC Function	none

is zone used in mixing-plane model? no

inlet

Condition	Value
Reference Frame	0
Gauge Total Pressure (pascal)	3e+08
Supersonic/Initial Gauge Pressure (pascal)	2.99899e+08
Direction Specification Method	1
Coordinate System	0
Turbulent Specification Method	0
Turbulent Kinetic Energy (m2/s2)	274
Turbulent Dissipation Rate (m2/s3)	32275560
Turbulent Intensity (%)	3.3799999
Turbulent Length Scale (in)	0.00091
Hydraulic Diameter (in)	0.013
Turbulent Viscosity Ratio	60.86
Discrete Phase BC Type	2
Discrete Phase BC Function	none
is zone used in mixing-plane model?	no

air_mass_outlet

Condition	Value
Turbulent Specification Method	0
Turbulent Kinetic Energy (m2/s2)	1
Turbulent Dissipation Rate (m2/s3)	1
Turbulent Intensity (%)	10
Turbulent Length Scale (in)	39.370079
Hydraulic Diameter (in)	39.370079
Turbulent Viscosity Ratio	10
Discrete Phase BC Type	4
Discrete Phase BC Function	none
is zone used in mixing-plane model?	no

outlet

Condition	Value
Gauge Pressure (pascal)	0
Backflow Direction Specification Method	1
Turbulent Specification Method	3
Backflow Turbulent Kinetic Energy (m2/s2)	1
Backflow Turbulent Dissipation Rate (m2/s3)	1
Backflow Turbulent Intensity (%)	0.099999998
Backflow Turbulent Length Scale (in)	1
Backflow Hydraulic Diameter (in)	1
Backflow Turbulent Viscosity Ratio	10
Discrete Phase BC Type	4
Discrete Phase BC Function	none
is zone used in mixing-plane model?	no

wall

```
   Condition                                   Value
   -------------------------------------------------------------------------
   Wall Motion                                   0
   Shear Boundary Condition                      0
   Define wall motion relative to adjacent cell zone?   yes
   Apply a rotational velocity to this wall?     no
   Velocity Magnitude (m/s)                      0
   X-Component of Wall Translation               1
   Y-Component of Wall Translation               0
   Define wall velocity components?              no
   X-Component of Wall Translation (m/s)         0
   Y-Component of Wall Translation (m/s)         0
   Discrete Phase BC Type                        2
   Normal                                        1
   Tangent                                       1
   Discrete Phase BC Function                    none
   Number of Splashed Drops                      4
   Impact Angle Function                         ((polynomial angle 1))
   Diameter Function                             ((polynomial 1.8e-09))
   Velocity Exponent Function                    ((polynomial 0))
   Rotation Speed (rad/s)                        0
   X-Position of Rotation-Axis Origin (in)       0
   Y-Position of Rotation-Axis Origin (in)       0
   X-component of shear stress (pascal)          0
   Y-component of shear stress (pascal)          0
   Specularity Coefficient                       0

  mass_inlet

   Condition                          Value
   -----------------------------------------------
   Turbulent Specification Method       0
   Turbulent Kinetic Energy (m2/s2)     1
   Turbulent Dissipation Rate (m2/s3)   1
   Turbulent Intensity (%)              10
   Turbulent Length Scale (in)          39.370079
   Hydraulic Diameter (in)              39.370079
   Turbulent Viscosity Ratio            10
   Discrete Phase BC Type               4
   Discrete Phase BC Function           none
   is zone used in mixing-plane model?   no

Solver Settings
---------------

 Equations

  Equation      Solved
  ------------------------
  Flow          yes
  Volume Fraction   yes
  Turbulence    yes

 Numerics

  Numeric                 Enabled
```

```
 ---------------------------------------
 Absolute Velocity Formulation   yes

Relaxation

 Variable                  Relaxation Factor
 ---------------------------------------------
 Pressure                  0.1
 Density                   1
 Body Forces               1
 Momentum                  0.40000001
 Volume Fraction           0.40000001
 Granular Temperature      0.2
 Turbulent Kinetic Energy     0.40000001
 Turbulent Dissipation Rate   0.40000001
 Turbulent Viscosity       1
 Discrete Phase Sources    0.5

Linear Solver

                        Solver    Termination   Residual Reduction
 Variable               Type      Criterion     Tolerance
 ----------------------------------------------------------------------
 Pressure               V-Cycle   0.1
 X-Momentum                 Flexible   0.1        0.7
 Y-Momentum                 Flexible   0.1        0.7
 Volume Fraction            Flexible   0.1        0.7
 Turbulent Kinetic Energy     Flexible   0.1        0.7
 Turbulent Dissipation Rate   Flexible   0.1        0.7

Pressure-Velocity Coupling

 Parameter   Value
 --------------------------------
 Type        Phase Coupled SIMPLE

Discretization Scheme

 Variable                  Scheme
 ------------------------------------------------
 Momentum                  Second Order Upwind
 Volume Fraction           QUICK
 Turbulent Kinetic Energy     Second Order Upwind
 Turbulent Dissipation Rate   Second Order Upwind

Solution Limits

 Quantity                    Limit
 ---------------------------------------
 Minimum Absolute Pressure      1
 Maximum Absolute Pressure      5e+10
 Minimum Temperature            1
 Maximum Temperature            5000
 Minimum Turb. Kinetic Energy     1e-14
 Minimum Turb. Dissipation Rate   1e-20
 Maximum Turb. Viscosity Ratio    100000
```